Electron transport in strong magnetic field gradients

Lambert, Nicholas John

Award date:
2007

Awarding institution:
University of Bath

ELECTRON TRANSPORT IN STRONG MAGNETIC FIELD GRADIENTS

NICHOLAS JOHN LAMBERT

A THESIS SUBMITTED FOR THE DEGREE OF
DOCTOR OF PHILOSOPHY
UNIVERSITY OF BATH
DEPARTMENT OF PHYSICS
JUNE 2007

ProQuest LLC
789 East Eisenhower Parkway
P.O. Box 1346
Ann Arbor, MI 48106-1346

ABSTRACT

The physics of magnetic edge states and snake orbits in two dimensional electron gases (2DEGs) formed in Dy/AlGaAs/GaAs heterostructures is investigated. Such orbits are formed when a ferromagnetic stripe deposited on a semiconductor heterostructure is magnetised. The stray field from the stripe results in a gradient in the perpendicular component of the field at the 2DEG of the order of 10^6T/m.

Magnetoresistance of a narrow, dry-etched, 2DEG channel subject to a high magnetic field gradient is investigated. The channel is shown to display positive, but asymmetric, magnetoresistance. A model is proposed in which positive and negative currents experience a different confining potential due to the field gradient. This alters the number of transverse current carrying modes in the channel, and so changes the channel conductivity.

Devices we have termed *snake state spectrometers* have been fabricated and tested. These consist of point contacts positioned to discretised the snake orbits formed in a channel subject to a magnetic field gradient. A third point contact acts to selectively transmit snake orbits with appropriate orbital parameters. Using these devices, we have detected the transmission of discrete snake orbits.

A theory is described in which electrons in snake orbits couple to the electromagnetic field. This results in conversion of electrical energy to microwaves. Preliminary experiments designed to test this theory led to the resistive detection of ferromagnetic resonance in the dysprosium stripe overlying the 2DEG.

ACKNOWLEDGMENTS

There are many people without whom this thesis would not exist.

First and foremost, I would like to thank Dr Alain Nogaret for his ever enthusiastic and knowledgable supervision.

The experimental results presented here were carried out at the Grenoble High Magnetic Field Laboratory, and I am grateful for the able assistance and advice of Sammi Sassine, Dr Yuri Krupko and Professor Jean-Claude Portal.

I am especially grateful for academic discussions with, and advice from, Dr Dejan Uzur, Dr Phillip Shields, Dr David Cole, Hywel Roberts, John Neal, Dr Jean-Marc Laventure and Dr Tom Kehoe. Excellent technical and administrative help in Bath was given by Dr Spartico Landi, Wendy Lambson, Barry Chapman, Timothy von Seld, Harry Bone, Eva Ashford, Alison Humphries, Jacqui Symon, Myla Dixon and Peter Sykes.

Moral support from other colleagues was invaluable. In particular, I'd like to thank Miles Engbarth, Malcolm Connolley, Pedro Saraiva, Stephen Taylor, Dr Matthew Myzelinski, Dr Greg Pearce, Matthew Burnett, Sue Hopton, Dr David Mawdsley, Dr Ruth Mason, Dr Lowenna Smith and Jonny Williams.

Thanks are also due to all those in the Bath University Mountaineering Club, especially the Andys, the Sarahs, Adam, Darrell, Ollie, Ellen, Ian, Helen, Jon, Alix, James, Tim, Jamie, Jo, Molly and Rob. Bath Symphony Orchestra provided many evenings of enjoyable distraction, and I'm grateful to Nathan, Jonny, Rosie, Katherine, Fran, Nicky, Mike, Lee, Peter and all the committee members.

I would also like to acknowledge the LaTeX 2ε template provided by André Miede.

Finally, I'd like to thank my family, especially my sisters.

CONTENTS

1 INTRODUCTION

1.1 MOTIVATION

Since the invention of the integrated circuit (i.c.) in 1959[37], semiconductor devices have been made ever smaller and more powerful. This rapid progress, which has also driven the expansion of the semiconductor industry, is often encapsulated by Moore's Law[51]. In 1965, Gordon Moore observed that the number of components on a single i.c. was doubling every two years, and predicted that this growth would continue into the future. Moore's law has held true since then, and has gone from being an observation on technical progress to a motivating philosophy for the semiconductor industry roadmap[31].

This demand for development has often driven technological development in diverse areas. In the past, this has included improvements in photolithography and wafer fabrication, and these pressures have pushed i.c. fabrication to 65nm feature sizes. However, it has been predicted that these technologies will hit fundamental problems when devices become so small that irregularities in fabrication dominate the characteristics of the device. To overcome this, a number of novel approaches are the subject of current research interest.

Rather than tackle the problems presented by the top-down approach head on, a bottom-up method appears to offer an attractive alternative. Fabrication of nano-electronic components made from carbon nanotubes[62], organic molecules[63] and semiconductor/molecular hybrids[20] all take this line of attack.

Another approach, which has already made the leap into commercial products, is to use the magnetic moment, or spin, of the current carrying electrons to process information. *Spintronic* devices are currently used in the read/write heads of hard discs and recently magnetic random access memory chips have been introduced to the market[65].

But the use of spin for information processing, rather than data storage and retrieval, has lagged behind. The primary requirements for spintronics are the presence of a non-equilibrium spin population and spin-dependent transport coefficients. Therefore, a thorough understanding of the interactions between charge carriers and magnetic fields in semiconductors is an important underpinning of the development of these technologies.

One system that has been investigated consists of a 2DEG channel subject to a spatially varying field. If the magnetic field perpendicular to the 2DEG changes sign anywhere in the channel, then a zero field line exists. The Lorentz force on either side of the zero line is in the opposite sense, and so electrons can be guided along the zero field line in orbits termed *snake states*.

These systems show a variety of interesting behaviours. This Thesis presents some research into them.

1.2 ORGANISATION OF THESIS

Introductory material is covered in Chapters 2 and 3. The relevant theory of magnetic materials and transport in mesoscopic semiconductor stuctures is discussed in Chapter 2. In Chapter 3 the experimental methods used are described, including nanofabrication techniques, cryogenic methods and microwave irradiation of the sample. Also discussed is the magnetisation and resultant stray field profile of a long thin ferromagnetic stripe, as this method was subsequently used throughout to impose a strong field gradient on 2DEGs.

Three experimental chapters follow. In Chapter 4, measurements of the resistance of a narrow 2DEG channel subject to a strong magnetic field gradient are presented. Asymmetric positive magnetoresistance was observed. This was explained using a theory based on calculations of the number of conducting modes in the channel.

Magnetoresistance measurements were also made on both sides of the thin channel simultaneously. A field dependent difference between the two was observed. This difference was thought to be due to conductance enhancement by magnetic edge states travelling in opposite directions at either edge of the channel.

Chapter 5 describes the fabrication and operation of a *snake state spectrometer*, designed to distinguish individual snake states in a channel modulated by a magnetic field gradient. This is done by the introduction of two point contacts to the channel, discretising the available states. States are then detected by a third point contact. The conductance of the device was observed to be enhanced when the classical electron trajectory passes through all point contacts.

The theory, and some preliminary measurements of, the interaction of snake states with the e.m. field is introduced in Chapter 6. A channel subject to the stray field from a dysprosium stripe was irradiated with microwaves whilst in a strong field. Ferromagnetic resonance in the stripe was detected *via* measurements of the conductance of the channel.

Finally, Chapter 7 draws together the conclusions, including possible areas of further experimental and theoretical work.

2 BACKGROUND THEORY

Research into semiconductors is wide-ranging, with much effort being directed towards semiconductor heterostructures, which consist of a junction between two different semiconductors. This is in contrast to a homojunction, in which two differently doped regions of the same material are brought into contact. Of particular interest are heterostructures incorporating quantum wells, which have lead to such technological developments as heterostructure based light emitting diodes, solid state lasers and high mobility transistors for high frequency applications.

The advent of nanostructuring techniques has allowed new physical regimes in heterostructures to be investigated. Devices with length scales comparable to the mean free path of electrons in the quantum well have revealed new physics. When combined with recent progress on magnetism and magnetic materials, this has made nanostructured magnetic devices a fruitful class of materials to investigate[48]. Examples include studies of magnetoresistance effects, magnetic multilayer materials and spin injection , leading to the use of electron spin for data storage and retrieval and information processing.

In this chapter the physics upon which the rest of the Thesis is based is summarised. Semiconductor heterostructures and ferromagnetic materials are described, and electron transport in mesoscopic semiconductor devices discussed.

2.1 SEMICONDUCTOR HETEROSTRUCTURES

The use of semiconductor heterostructures was first proposed in the early 1950s by W. Shockley[74] and others[40]. Extensive theoretical work was carried out around this time, including analysis of the current-voltage characteristics of junctions and the properties of injected carriers, and the proposal of a variety of possible device applications[3]. However, theoretical studies were for some time ahead of experimental work. This was due to the difficulty of finding two different semiconductors with suitable properties – a number of conditions of compatibility need to be met.

The foremost requirement is for the two compounds to have closely matching lattice constants (ideally within 1%), to avoid dislocation defects at the interface[5]. It is clearly also necessary

for the crystals to have the same crystalline structure. Thermal properties must also be similar, to avoid stresses when heating or cooling, and the compounds must be chemically stable.

Diffusion of dopants across the boundary between the two compounds can also cause problems known as cross doping effects. For example, this situation could potentially occur in the semiconductor pair GaAs/Ge, as Ga and As are dopants of Ge, and Ge is a dopant of GaAs[50]. This problem can be minimised by keeping the growth temperature as low as possible.

GaAs has a number of properties which make it a well-studied and useful material[2]. In particular, it has some advantages over silicon. It has a direct bandgap, making optically active devices easier to fabricate. It has a high electron mobility, which is important for high frequency devices. It also has a higher breakdown voltage, allowing higher power circuits.

These properties made GaAs a suitable starting point for attempts at developing a useful heterostructure. Appropriate materials with closely matching lattice constants included GaP and AlAs. However, these are not chemically stable. The realisation that AlGaAs is stable, and developments in heterostructure fabrication lead to the first lattice matched AlGaAs/GaAs heterostructures simultaneously at the Ioffe Physico-Technical Institute in Russia[4] and at IBM[70].

Since then, a range of other combinations have been fabricated and investigated. Careful selection of semiconductor pairs (within the requirements stated above) allows fine-tuning of device parameters such as carrier mobility and optical properties. For example, InAs/GaAs heterostructures are used for infrared wavelength photodiodes. Heterojunctions are also used in a variety of other technological applications, including diode lasers, bipolar junction transistors and phototransistors[50].

2.1.1 *Fabrication*

There are two steps in preparing a heterostructure from raw materials. First, a single crystal of substrate must be prepared, and then a suitable set of layers grown on top of it.

Boule growth

The first stage in fabricating a semiconductor heterostructure is the growth of a large, single crystal cylinder of the substrate material, termed the boule. *Czochralski crystal growth* is a widely used method for a variety of semiconductors.

In this technique, a crucible of high-purity molten semiconductor is prepared. A seed crystal is mounted on a rod, and dipped

into the melt. It is then slowly drawn out while rotating. By precise control of the speed, rotation and temperature gradient, a single crystal is formed. Dopants can be added to the crucible before the drawing process begins. The process is done in an inert atmosphere (typically argon) and in an inert crucible, usually quartz.

If the semiconductor is composed of multiple elements, such as a III-V material, then additional problems of decomposition are presented. The addition of a liquid lid or encapsulate, a technique known as Liquid Encapsulated Czochralski (LEC) growth, is growing in popularity. In the case of GaAs, arsenic is the more volatile of the two constituents, and so the semiconductor mix is typically covered by a boron oxide melt. An inert gas at a higher pressure than the arsenic partial pressure prevents the melt from boiling.

This technique introdues a relatively high level of oxygen impurities, scavenged from the quartz crucible. This, and the othe problems related to compound materials, means that this approach is not always ideal for GaAs growth, and so the *Bridgeman technique* is often used. In this process, the seed crystal is placed at one end of the crucible, and the melt is cooled from that end, by either moving the crucible in furnace or vice versa.

Once a cylindrical crystal has been prepared, circular wafers are cleaved from it.

Deposition of the heterostructure

Once a wafer of bulk semiconductor substrate has been obtained, the crystalline heterostructure is then grown on one side of it. This relies on careful control of the thickness, quality and purity of the deposited layers. The layers must also be aligned with the crystal axis of the substrate. The process is termed epitaxial growth, and there are three principle methods for doing this.

Vapour Phase Epitaxy (VPE) uses a stream of gaseous elements or compounds directed at the surface of the substrate, which condense to form the required layer. This is the predominant technology in use in industry. In Liquid Phase Epitaxy (LPE), the substrate is immersed in a saturated metallic solution containing the necessary layer components. However, these methods have a variety of disadvantages when compared to Molecular Beam Epitaxy (MBE)[10].

MBE takes place in a ultra-high vacuum chamber. Sources, called effusion cells, or Knudsen cells, are loaded with the required materials for the epitaxial layers, and aligned with the substrate. These are then heated until thermal evaporation permits the atoms to escape from the cell. In the high vacuum envi-

Chapter	X (nm)	Y (nm)	2DEG depth (nm)	Mobility ($cm^2V^2s^{-1}$)	m.f.p. (μm)
4	12.5	12.5	30	3.5×10^5	3.35
5	17.5	17.5	40	7.2×10^5	9.04
6	22.5	12.5	40	6.5×10^5	6.05

Table 1. Parameters for the heterostructures used in this work. Carrier densities are deduced in the relevant chapters.

ronment, scattering of the atoms is minimized and they form a beam incident upon the substrate. Shutters in front of the sources allow precise control of the growth profile. This method is relatively slow (approximately one layer per second), but results in sharp boundaries between layers, very low impurity levels and highly uniform layers. Doping levels can be precisely controlled. This method has produced samples with the highest recorded mobilities [75].

For a GaAs/AlGaAs heterostructure, a typical growth structure is shown in fig. 1. The parameters for the heterostructures used in our experiments are shown in table 1, with mean free path (m.f.p.) lengths being determined from the mobility and the carrier density.

2.1.2 *The GaAs/AlGaAs quantum well*

Semiconductor heterostructures can therefore be regarded as single crystals in which the lattice occupancy changes at an interface[38]. Such junctions are usually understood by considering first the band structure in the individual materials, and then the modifications to these by interactions at the inteface. (Although the physics is similar for all semiconductor heterostructures, the GaAs/AlGaAs system is discussed here.)

Semiconductors have a conduction band that lies close to the valence band. The energy distance between them is referred to as the band gap. Electrons in the semiconductor fill the energy levels available, starting from the lowest. The Fermi level at $T = 0K$ is defined as being the level above which all states are empty and below which all are filled. At finite temperatures, the electron distribution is thermally broadened, and the Fermi level is defined as being the level of which the occupancy is one half.

GaAs and AlGaAs are both direct band gap semiconductors,

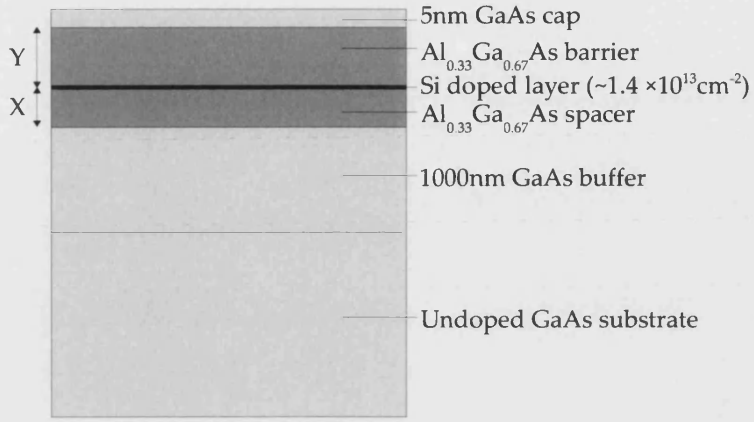

Figure 1. Typical composition of a near-surface modulation doped GaAs/AlGaAs heterostructure. X and Y denote the depth of the spacer and barrier layers respectively. Values of these and other parameters for the heterostructures used in our experiments are shown in table 1.

with the Fermi level lying between the valence band (at an energy E_v) and the conduction band (at E_c). However, the energy gap between these two ($E_c - E_v$) is larger in AlGaAs, and the Fermi level is higher.

We now bring the two materials into contact. The Fermi levels in the two materials must equalise (otherwise there would be a permanent potential between the two layers). This is achieved by the migration of carriers and the bending of the band structure in the region of the interface (fig. 2). The bending of the conduction band creates a potential well, which dips below the Fermi level and can therefore be populated with electrons.

The electrons come from Si donors implanted in a thin layer in the AlGaAs. This highly doped layer is generally spatially separated from the interface, a technique referred to as *modulation doping*. This reduces scattering of electrons from impurities, and so increases their mobilities.

Si donors are substitutional – they generally occupy the lattice site usually ocupied by the group-III species, but this is not always the case[53]. If, instead, the ion is displaced to an interstitial location then a defect trap is created (see fig. 3). These are termed DX centres, and usually trap electrons during the cooldown process. The electron population in the traps depends on the rate at which the system is cooled. This presents a problem if a

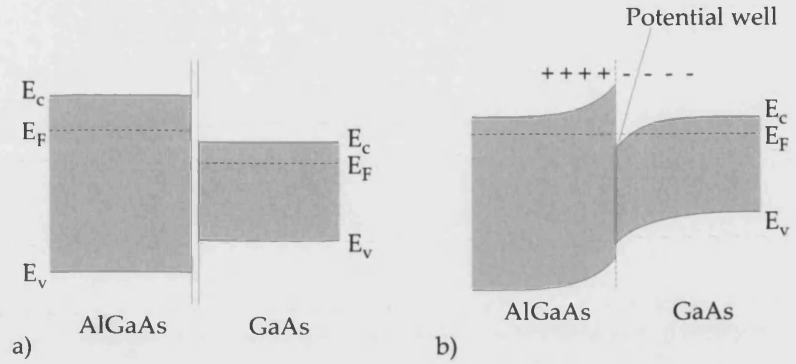

Figure 2. Band structure in a GaAs/AlGaAs heterotructure. a) The structure of the separate materials. b) The materials are brought into contact. The requirement for equalisation of the Fermi level results in charge redistribution and band bending at the boundary.

reproducible electron density is required.

Electrons can be excited from these traps by an incident photon of energy $h\nu \approx 1.3 - 1.4$eV[35]. They then tend to migrate to the potential well, as to re-enter the trap, they would have to overcome a potential barrier of around 0.16eV. This leads to a persistant photoconductivity effect[80]. Photoconductivity is also caused by electron-hole generation in the bulk GaAs, followed by charge separation at the interface[35]. The relative size of these two effects depends on the structural and material parameters of the heterostructure.

The illumination of the heterostructure therefore permits rudimentary control over the electron density in the potential well. It is of particular use if an electrostatic gate cannot be overlayed over the entire heterostructure – if, for example, a split gate design (see below) is used, or if optical access to the device surface is required.

Electron gas depletion by an electrostatic gate relies on the existence of a Schottky barrier (also depicted in fig. 3) caused by band bending at the metal-semiconductor interface. This insulates the metal from the semiconductor. A potential difference between the gate and the electrons in the potential well affects the electron density by the electrostatic interaction – a negative gate voltage depletes the electron gas, and a positive voltage increases the carrier density.

The application of a large negative gate voltage can deplete the potential well entirely. This technique is used to shape the electron

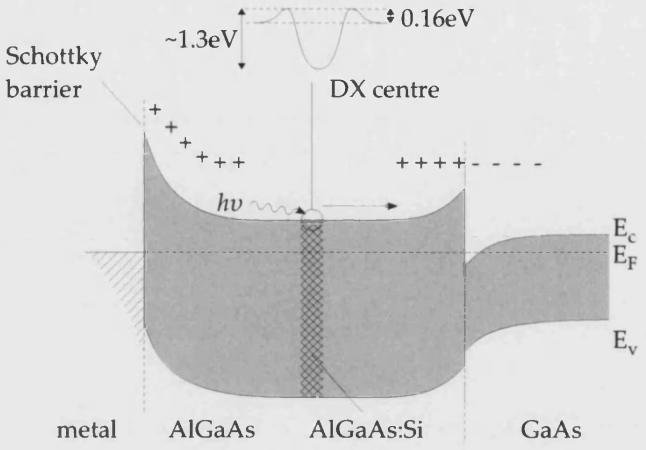

Figure 3. Heterostructure band structure modified by a Schottky barrier at a semiconductor-metal interface and the presence of misplaced Si donors forming traps.

gas in *split gates*(see section 3.1.4). Conversely, a large positive voltage can raise the Fermi level to the point where conduction channels are opened in the AlGaAs layer. Furthermore, too large a magnitude of gate voltage can overcome the Schottky barrier, and cause a gate leakage current into the semiconductor.

2.1.3 *A two-dimensional system*

As the potential well is so narrow, discrete transverse modes are formed, and the energy of electrons in the well is quantised. If only one of the subbands lies below the Fermi surface, then only that energy level will be populated and a *two-dimensional electron gas* will form. A further proviso for this to occur is that the temperature is sufficiently low that significant numbers of electrons are not thermally excited into the higher subbands.

In a typical GaAs/AlGaAs heterostructure, the difference between the first two energy levels is approximately 30meV[75]. This is sufficiently large that transport remains predominantly two-dimensional well above 4.2K.

A 2DEG in an GaAs/AlGaAs modulation doped heterostructure was first observed by Dingle *et al* in 1978[18].

2.2 MAGNETIC MATERIALS

Magnetic fields, and the resultant forces, are due to the movement of an electric charge. In many cases, this movement is in the form of a current loop. Some materials, particularly when placed in an external magnetic field, possess a magnetic moment. This is called the *magnetisation* of the material.

By convention, H is used to denote an applied field, M describes the magnetisation of a sample and B is the resultant magnetic field density, or the magnetic induction. The unit of B used here is Tesla, and the units of M and H is A/m. However, the quantities $\mu_0 H$ and $\mu_0 M$ are usually used, and these also have units of Tesla.

2.2.1 *Origins of magnetism: atomic magnetic moment*

Bulk magnetism originates in the magnetic moment of individual atoms. This in turn is a result of the magnetic moment from individual orbital electrons. There are two contributions to the magnetic moment of a particular electron; the first comes from the angular momentum of the electron orbit around the nucleus.

An orbiting electron, of charge $-e$ and angular frequency ω, is equivalent to a circulating current i, where $i = e\omega/2\pi$. As the magnetic moment due to a circulating current is $M = iS$, where S is the area of the current loop, the magnetic moment due the orbital angular momentum of the electron is

$$M = -\frac{e\omega r^2}{2}. \tag{2.1}$$

As P, the orbital angular momentum of the electron, is given by $P = m\omega r^2$, this can also be written as

$$M = -\frac{e}{2m}P, \tag{2.2}$$

showing that magnetic moment is proportional to angular momentum.

The angular momentum of the orbiting electron is quantised. Permitted values are given by $P = l\hbar$, with l, the orbital angular momentum quantum number, being integer. This means that the resultant magnetic moment is also quantised. The allowed values are

$$M = -\frac{e\hbar}{2m}l. \tag{2.3}$$

Magnetic moment therefore comes in integer multiples of

$$M_B = \frac{e\hbar}{2m}, \tag{2.4}$$

a quantity termed the Bohr magneton.

The electron also has an intrinsic *spin angular momentum*. The magnitude of the spin is $\hbar/2$. Angular momentum is therefore given by

$$P = s\hbar, \tag{2.5}$$

where $s = \frac{1}{2}$ and is called the spin quantum number. The resultant magnetic moment is

$$M = -\frac{e\hbar}{m}P. \tag{2.6}$$

There are therefore two individual contributions to the magnetic moment of an atom or ion. The net moment depends upon the electronic structure of the atom, and on the filling of electron shells. In particular, unpaired electrons can contribute strongly to the total moment.

The magnetic moment of an atom is often described as its spin, even though it contains an orbital component.

2.2.2 *Bulk magnetic materials*

The magnetic behaviour of bulk materials can be divided into two categories[14]. A lack of long range magnetic order of atomic magnetic moments, resulting in feeble bulk magnetism, is either *diamagnetism* or *paramagnetism*. Long range order, leading to stronger bulk magnetism, is termed *ferromagnetism* (in its broadest sense). This in turn can be subdivided into types of ordering, the main ones being *ferromagnetism* (the narrower sense in which it is used from now on), *ferrimagnetism* and *antiferromagnetism*.

In ferromagnetic materials, neigbouring spins align due to the *exchange interaction* between them. This interaction originates from the Pauli exclusion principle. If neighbouring atoms have unpaired electrons with opposite spin then they can approach each other, and the electrostatic energy of the system is increased. If, however, the spins are aligned in the same direction, they cannot approach each other due to the exclusion principle, and the Coulomb energy is decreased. Neighbouring spins are therefore aligned, despite the classical tendency of magnetic moments to antialign.

Domains

Over longer distances, the magnetostatic energy of a single large dipole increases, until it becomes energetically favourable for the spin population to split into two or more non-aligned regions. These are termed domains, and are arranged in such a way as to minimise the total energy of the spin system. They tend to be aligned with the crystal structure of the ferromagnet.

A single domain is at saturation magnetisation by its nature, but in zero applied magnetic field, a ferromagnet will tend to have a net magnetisation of zero – domains of different magnetisation direction will cancel each other out.

They are separated by intermediate regions called *domain walls.* In these regions, the spin angle changes gradually, over a few hundred[38] atoms. This is because the exchange energy of neighbouring spins increases with the square of the angle between them.

Magnetisation process

When a magnetic field, H, is applied to a ferromagnetic material, the magnetisation of the material increases. This is achieved through movement of the domain walls – in the case where field is applied along crystal direction domains aligned with applied field grow, while domains at 180° and 90° to H shrink. This continues until the entire sample is magnetised in one direction, and saturation magnetisation is therefore reached.

If the field is applied in a direction not parallel to crystal direction, then the two (if the field is applied along the [110] direction) or three (if the field is applied along the [111] direction) domain orientations closest in alignment to H grow until they occupy the entire sample. Further field increases then rotate these domains to align with the field. Again, the entire sample is magnetised. For a polycrstalline material, the magnetisation curve of the sample will be an average of the curves for the different crystal orientations present.

The magnetisation curve can be divided into three regions. When the field is first applied, reversible domain boundary movement occurs, primarily through bulging domain walls[14]. As the field is increased, domain walls move and irreversable boundary displacement occurs. The final region of increased magnetisation comes from magnetisation rotation of domains. All spins are now aligned with the applied field.

This maximum magnetisation is termed the *saturation magnetisation.* When the applied field is decreased, the magnetisation does not return along the same path – there is some hysteresis.

The magnetisation present when $H = 0$ is termed the *remanance magnetisation*. As the field is applied in the opposite sense, the magnetisation reduces to zero and then once more becomes aligned with the applied field. The applied field at which the magnetisation is zero is the *coercivity*.

In fact the magnetisation curve is not smooth. Domain wall movement progresses in small leaps, as walls are released from some fixed point and then repinned. Small volumes of spin switching direction can cause nearby regions to flip, setting up a cascade effect. This is termed the *Barkhausen effect*. Magnetisation reversal in a region often initiates at a defect, such as a grain boundary or impurity, and then propagated through the sample.

These reversal processes can result in localised vortices in the magnetisation – a point around which the magnetisation vector circulates. These form in small magnetic elements, in which geometric constriction is important, and are typically seen at intermediate fields in the switching process.

2.2.3 *Shape effects on sample magnetisation*

When a finite sample is magnetised, its shape has a significant effect on the shape of the magnetisation curve. This is because free magnetic poles are created at either end of the sample. These create a demagnetising field,

$$H_d = \frac{NM}{\mu_0}, \tag{2.7}$$

which acts in the opposite direction to the magnetisation. N is called the demagnetising factor, and depends heavily upon the shape and direction of magnetisation of the sample. An anisotropic sample will therefore have 'easy' and 'hard' axes of magnetisation. A given field applied along the easy axis will result in a greater magnetisation than the same field applied along the hard axis.

For example, if the sample is a thin elliptical plate, as shown in fig. 4, it will be easier to magnetise along a vector in the plain than normal (Axis C in fig. 4) to it, as this minimises the size of the free poles. Similarly, it will be easier to magnetise it parallel to the long axis (axis A) of the ellipse than parallel to the short axis (axis B).

2.2.4 *Ferromagnetic resonance*

A magnetic state vector will precess about an external applied field. If this precession involves the nuclear spin, the phenomenon

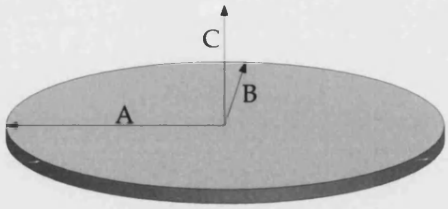

Figure 4. Magnetisation axes of a thin ellipsoidal plate. A (the longest axis) is the easy axis, and C is the hard axis.

is termed nuclear magnetic resonance. If the precession involves the total electron magnetic moment in a ferromagnet, it is termed ferromagnetic resonance (FMR). The angular frequency of rotation is given by

$$\omega = -g\frac{e\mu_0}{2m}H. \tag{2.8}$$

It therefore depends upon the magnitude of the applied field and g, the gyromagnetic ratio for the material.

If there is no external source of energy, this angular momentum will die away, due to damping in the crystal lattice. To maintain the precession, an electromagnetic field of angular frequency ω can be applied, so that the spin is subject to an alternating magnetic field. For typical material parameters and the application of a field of 1T, $\omega = 1.76 \times 10^{11}\text{rads}^{-1}$, which corresponds to a frequency of 2.8×10^{10}Hz. This is the microwave region of the electromagnetic spectrum.

FMR can be detected by inserting a sample in a microwave cavity with a static field orthogonal to the e.m. radiation. A microwave detector is used to measure the absorption of radiation by the sample, and the static field is swept through a range of values. When the frequency of the microwaves matches ω, and the resonant condition is met, absorption of the microwaves will increase. A decrease in the intensity at the detector will be recorded.

FMR can be used to measure the ferromagnetic properties of a material. For example, it has been used to probe spin waves[46], saturation magnetisation[11] and exchange couplings[30].

2.3 ELECTRON TRANSPORT IN 2DEGS

2.3.1 *Electron transport in mesoscopic 2DEG structures*

Electrons in a single subband of a 2DEG have energy (relative to the bottom of the subband)

$$E(k) = \frac{\hbar^2 k^2}{2m}. \tag{2.9}$$

The density of states (DOS) is given by

$$\rho(E) = \frac{g_s g_v m}{2\pi\hbar^2}, \tag{2.10}$$

where the spin degeneracy $g_s = 2$ and the valley degeneracy $g_v = 1$. The DOS is therefore independent of the energy. A sequence of subbands in the DOS are associated with different energy levels in the well at the heterostructure interface. Usually, only a single subband is occupied, and so this means that the electron density, n, is related to the Fermi energy by

$$n_s = \frac{E_F g_s g_v m}{2\pi\hbar^2}. \tag{2.11}$$

The Fermi wavevector, $k_F = \sqrt{2mE_F/\hbar^2}$, is related to density by

$$k_F = \sqrt{4\pi n_s / g_s g_v}. \tag{2.12}$$

The application of an electric field shifts the distribution of electrons in k-space away from the equilibrium. Assuming this shift is small in comparison to k_F, most electrons with wavevector $k > 0$ are still compensated by electrons with wavevector $k < 0$. The electron states previously occupied by electrons with wavevectors around $-k_F$ will be empty. Conversely, empty states around $+k_F$ are filled. As a consequence of this, electrical charge transport is due only to electrons around the Fermi surface.

2.3.2 *Diffusive and ballistic transport*

Often the mean free path of an electron in a nanostructure is comparable to the scale of the device. It is therefore useful to consider two regimes in which transport can take place. In the

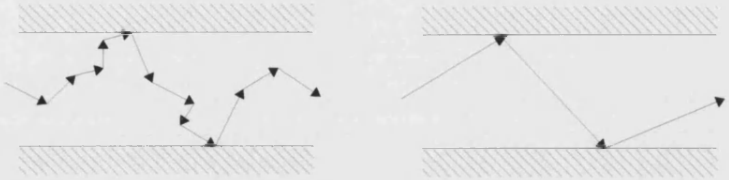

Figure 5. Transport in a 2DEG channel. a) The diffusive regime. Electrons scatter from the channel walls, defects, electrons and thermal phonons. b) The ballistic regime. Electrons scatter only from the channel walls.

diffusive regimes (fig. 5a), the mean free path (m.f.p) of the electrons is much shorter than the characteristic length of the system. Most scattering events consist of interactions with defects and phonons, and these are the main contribution to the resistivity of the channel. This behaviour is described by the Drude model discussed in section 2.3.3.

If, on the other hand, the m.f.p. is longer than the length scale of the system, then the electrons are described as moving ballistically (fig. 5b). Scattering occurs mainly from the boundary of the conducting channel, and can be either specular or diffuse, the latter resulting in an isotropic momentum distribution after the collision. If the scattering is specular, then momentum along the channel is preserved, and there is no contribution to the resistivity. Typically, however, there is a diffuse component to boundary scattering.

The intermediate regime, in which both effects are significant, is termed the quasi-ballistic regime.

2.3.3 *Diffusive transport*

Drude model of conductivity

In a zero or weak magnetic field, a simple model can be used to relate longitudinal and transverse conductivity to the transport properties of the 2DEG. (Magnetotransport is discussed in more depth in section 2.3.5.)

Current carrying electrons gain momentum from an external electric field, **E**, and lose momentum in collisions with defects and phonons. In the steady state, the rate of change of momentum from each mechanism is equal and opposite. This condition can

be written as

$$\left[\frac{d\mathbf{p}}{dt}\right]_{\text{scattering}} = -\left[\frac{d\mathbf{p}}{dt}\right]_{\text{field}}. \tag{2.13}$$

In terms of properties of the 2DEG, this becomes

$$\frac{m\mathbf{v}_d}{\tau} = e[\mathbf{E} + \mathbf{v}_d \times \mathbf{B}]. \tag{2.14}$$

Here, τ is the scattering time, or the momentum relaxation time, and $\mathbf{v}_d$ is the drift velocity.

We can relate the current density, $\mathbf{J}$, to the carrier density and the drift velocity by $\mathbf{J} = e\mathbf{v}_d n_s$, and rewrite equation 2.14 in vector form to obtain

$$\begin{bmatrix} \frac{m}{e\tau} & -B \\ +B & \frac{m}{e\tau} \end{bmatrix} \begin{pmatrix} \frac{J_x}{en_s} \\ \frac{J_y}{en_s} \end{pmatrix} = \begin{pmatrix} E_x \\ E_y \end{pmatrix}. \tag{2.15}$$

The *resistivity tensor* is defined by

$$\begin{pmatrix} E_x \\ E_y \end{pmatrix} = \begin{bmatrix} \rho_{xx} & \rho_{xy} \\ \rho_{yx} & \rho_{yy} \end{bmatrix} \begin{pmatrix} J_x \\ J_y \end{pmatrix}. \tag{2.16}$$

Equation 2.15 can be rewritten as

$$\begin{pmatrix} E_x \\ E_y \end{pmatrix} = \sigma^{-1} \begin{bmatrix} 1 & -\mu B \\ +\mu B & 1 \end{bmatrix} \begin{pmatrix} J_x \\ J_y \end{pmatrix}, \tag{2.17}$$

where $\sigma = |e|n_s\mu$ and $\mu = |e|\tau/m$. Combined with equation 2.16, this gives us

$$\rho_{xx} = \sigma^{-1} \tag{2.18}$$

$$\rho_{yx} = -\rho_{xy} = \frac{\mu B}{\sigma} = \frac{B}{|e|n_s}. \tag{2.19}$$

So, the longitudinal resistivity is predicted to be constant. The perpendicular resistivity (the Hall resistivity, see section 2.3.5) increases linearly with field. These predictions are generally true for weak applied fields.

2.3.4 *Ballistic transport*

Quantum point contacts – conduction quantisation

A quantum point contact is a lateral constriction in a 2DEG channel, with a width of the order of the Fermi wavelength of electrons in the 2DEG. Lateral electron modes in the channel are quantised because of this constriction. The available conductance modes are therefore also quantised, which leads to quantised resistance steps of size $2e^2/h$ as the width of the QPC is changed. This is discussed in detail in section 2.3.4.

This geometry is realised either by etching a narrow channel or, more usually, by a split electrostatic gate on top of the heterostructure. The application of a negative voltage to this depletes the 2DEG beneath the gate (see section 2.1.2) – by varying the voltage the width of the contact can be changed.

Ballistic conductance effects

In the ballistic and quasi-ballistic regimes, the geometry of the sample can have a strong influence on its conductance, as boundary scattering is the dominant contribution to the resistance of the device. For example, the case of an electron entering a channel can be considered (figs 6a and b). The configuration of the junction between the channel and the wider region controls the amount of backscattering of electrons.

Ballistic effects can also produce voltage differences between contacts to 2DEG channels where, classically, there should be none. Two such situations are shown in figs 6c and d. In fig 6c, the current is being injected and extracted through contacts A and B. Further down the channel, the *non-local voltage* between C and D is being measured. As ballistic electrons injected from A are not necessarily scattered into B, some continue down the channel and contribute to a potential difference between C and D.

In fig. 6d the *bend resistance* is being meaured. Again, current is being injected through contacts A and B, and the voltage probes are labelled C and D. In this geometry, we are measuring the voltage associated with the bend in the current towards B. This is affected by an applied magnetic field, as discussd in section 2.3.5.

The Landauer-Büttiker formalism

Conduction through a channel between two or more reservoirs can be formally studied using the Landauer-Büttiker formalism.

In the Landauer model, the conductivity of a sample is disregarded in favour of considering the conductance. This means the

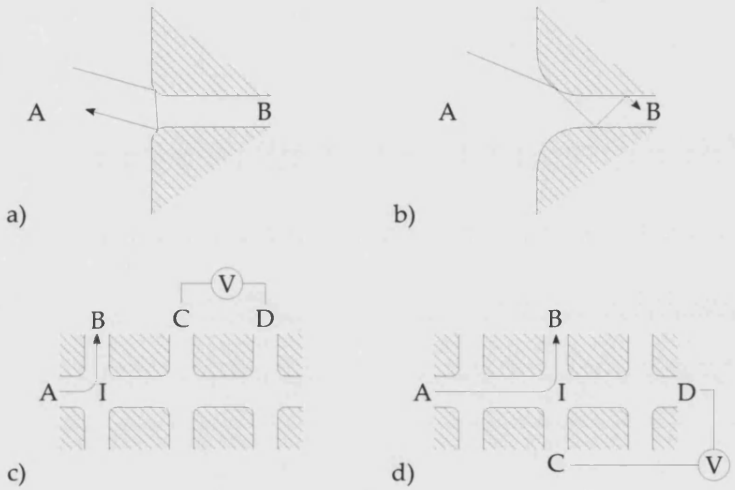

Figure 6. a) Electrons travel from a wide region of the 2DEG (A) to a narrow channel (B). The sharpness of the transition region causes backscattering. b) A more gradual transition reduces the backscattering. c) A current is injected from A to B, and the voltage measured across C and D further down the channel. Electrons which have not followed the classical path (I) contribute to a potential. d) Measurement of the voltage (C-D) associated with a bend in the current, which is again from A to B.

model can be applied when the concept of a local conductivity is not valid. One consequence of this is the independence of a channel's resistance on its length.

An electric current is carried by a number of conducting channels. To determine the transmission in each channel, we consider two reservoirs at energies E_F and $E_F + \delta\mu$. Electrons states with the group velocity in one direction are occupied up to E_F, while states travelling in the other direction are occupied up to $E_F + \delta\mu$. Therefore states between E_F and $E_F + \delta\mu$ contribute to the transmission.

To determine the total transmission, we integrate the product of the density of states and the group velocity in this interval. So

$$J_n = \int_{E_F}^{E_F+\delta\mu} g_s g_v \left(2\pi \frac{dE_n(k)}{dk}\right)^{-1} \frac{dE_n(k)}{\hbar dk} \tag{2.20}$$

$$= \frac{g_s g_v}{h}\delta\mu. \tag{2.21}$$

This is independent of the mode and the Fermi energy, as the group velocity and 1D density of states cancel each other out.

Using $\delta\mu = \delta n/\rho(E_F)$, $J = D\delta n$ and $G = e^2\rho(E_F)D$ we obtain

$$G = \frac{2e^2}{h}N \tag{2.22}$$

where N is the number of conducting channels available. In a square well point contact, the number of (one spin) conducting channels is given by

$$N = \frac{W}{2\lambda_F}, \tag{2.23}$$

and so the conductance of the point contact is

$$G = \frac{e^2}{h}\frac{W}{\lambda_F}. \tag{2.24}$$

More generally, this concept can be extended to conductance between a number of different reservoirs. For example, a four point resistance measurement may be considered. Voltage and current contacts are not considered separately. Rather, they are both described as reservoirs. Pairs of reservoirs are then considered, which are connected by leads.

For a given pair, reservoir A will be connected to m conductance channels in its lead, while reservoir B will be connected to

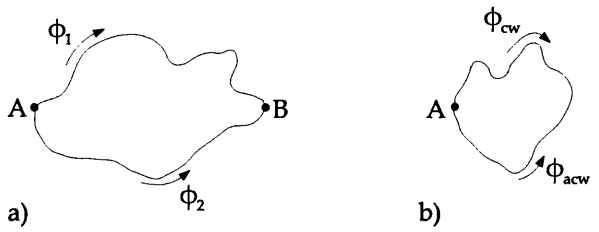

Figure 7. Weak localisation. a) Two arbitrary paths between two points. Phases are unrelated. b) An electron path forms a loop back to its starting point. Clockwise and anticlockwise phases are the same.

n channels in its lead. The transmission probability amplitude from channel m in lead A to channel n in lead B is given by $t_{BA,nm}$. The total transmission probability from reservoir A to reservoir B is then given by

$$T_{A\to B} = \sum_{m=1}^{N_A} \sum_{n=1}^{N_B} |t_{BA,nm}|^2 . \tag{2.25}$$

Probabilities can be determined for each pair of contacts, and so the behavior of the multireservoir conductor as a whole studied.

Weak localisation

Weak localisation[5, 7] is a phase coherent effect observed in 2D or thin film systems in which the probability for defect scattering is sufficiently high. The effect comes from the interference of counter-propogating closed electron paths, which is not taken into account by the Landauer-Büttiker formalism.

The situation in shown in fig. 7. Ballistic electrons from an arbitrary starting point (A) will then scatter off a number of defects before arriving at some finishing point (B). These paths are, in general, unrelated, and so there is no phase coherence between the two.

However, when A and B are in the same position, and so the electron is scattered back to its starting point, the situation is slightly different. In this case the path describes a closed loop, which can be traversed either clockwise or anticlockwise.

The paths are symmetric and phase coherent. This results in constructive interference of the electron's wavefunction at A, and an corresponding increase in the probability of the electron being scattered back to its starting point. The result of this is to increase

the resistivity of the 2DEG. Typically this effect is only significant below about 4K in AlGaAs/GaAs 2DEGs[15].

2.3.5 *Electron transport in magnetic fields*

A magnetic field component perpendicular to the plane of the 2DEG (B_z) has a variety of effects on the transport properties of the system. Note that the in-plane components have no effect the because perpendicular component of the electron momentum is quantised, and the energy levels are widely spaced. However, an in-plane field is often applied in experiments in order to magnetise a magnetic nanostructure deposited on the heterostructure. The stray field from this then has a non-zero and spatially varying B_z component.

Homogeneous magnetic fields

Homogenous magnetic fields have a number of effects on electron trajectories and energy levels. One of the most commonly observed is the Lorentz force. This is experienced by an electron travelling in a magnetic field, and is given by $\mathbf{F_L} = e(\mathbf{v} \times \mathbf{B})$. It therefore acts perpendicular to the direction of travel and the field direction. This force results in a number of effects, the most commonly observed of which is the Hall effect. This has already been mentioned in section 2.3.3, but is expanded upon here.

If a slab carrying a current I_H is subjected to a magnetic field normal to the plane of the slab, then the current-carriers are subject to the Lorentz force. This results in a build up of carriers at one side of the slab, and a consequent potential – the Hall voltage, V_H – across the slab. For a two-dimensional system, V_H is given by

$$V_H = \frac{BI_H}{ne}, \tag{2.26}$$

where n is the sheet carrier density.

More generally, in a bulk 2DEG, an applied field will force electrons to move in a circle. The electron will orbit with angular frequency

$$\omega_c = \frac{e\mathbf{B}}{m}. \tag{2.27}$$

A quantum picture of this can be developed. To obtain do this, we require the Schrödinger equation for the system. To obtain

this we write the momentum in operator form, as $\mathbf{p} - e\mathbf{A}$, where $\mathbf{A}$ is the vector potential and is defined by

$$\mathbf{B}(\mathbf{r},t) = \nabla \times \mathbf{A}(\mathbf{r},t). \tag{2.28}$$

Selection of the Landau gauge, $\mathbf{A} = -By\hat{\mathbf{x}}$ (for a field of form $\mathbf{B} = (0,0,B_z)$) leads us to the Schrödinger equation,

$$\left[-\frac{\hbar^2}{2m}\nabla^2 - \frac{ie\hbar}{mc}\mathbf{A}\cdot\nabla + \frac{e^2}{2mc^2}\mathbf{A}^2\right]\psi = E\psi. \tag{2.29}$$

It can then be demonstrated that the electron energies are given by

$$E = (n+1/2)\hbar\omega_c + \frac{\hbar^2 k^2}{2m}, \tag{2.30}$$

and so are quantised. These energy levels are termed *Landau levels*, and, in the absence of scattering, modify the density of states to a series of Kroniger delta functions,

$$\rho(E) = g_s g_v \frac{eB}{h}\sum_{n=1}^{\infty}\delta(E - E_n). \tag{2.31}$$

In fact, defect scattering and disorder broadens the levels, and so the inter-level density of states is non-zero.

In the central region of a confined 2DEG, and in the absence of an applied electric field, electrons in Landau states are stationary. However, at the perimeter of the sample, electrons will travel in one direction in *edge states*. A confined 2DEG with a perpendicular applied magnetic field will therefore have a current circulating around the edges, even in the absence of an electromotive force. However, any cross-section across the sample will have a *total* current density of zero.

Shubnikov-de Haas oscillations

As discussed in section 2.3.1, only electrons around the Fermi level contribute to conductance in the 2DEG. Therefore, a change in the DOS at the Fermi level affects the conductivity. If a Landau level coincides with the Fermi level then scattering will be augmented and the resistance increased. Conversely, if the Fermi level is in an inter-level region, the resistance will be decreased.

As the spacing of the Landau levels depends on the applied perpendicular field, so does the DOS at the Fermi level. The

magnetoresistance therefore shows oscillations periodic in 1/B, with minima at

$$B = \frac{hn_s}{2eN} \tag{2.32}$$

for integer values of N. These are termed Shubnikov-de Haas oscillations, and are often used to determine the electron density in a 2DEG. N is the *filling factor* and is the number of completely filled Landau levels.

The quantum Hall effect

The Hall resistance also shows features periodic in 1/B. Plateaux are observed at the same position as the mangetoresistance minima. This is the integer quantum Hall effect, and while the plateau have the same periodicity as the Shubnikov-de Haas oscillations, different physics is involved.

The number of edge states at the perimeter of a sample depends upon the magnetic field, but is always integer. (The fractional quantum Hall effect is a many body effect, and is, as yet, not fully understood.) Current flow around the sample is therefore also quantised. This effect requires transport to occur in spatially well separated edge states, so scattering between them is supressed and transport is adiabatic. High fields are therefore required, as transport at lower fields occurs in states that interact with both edges of the sample.

Other magnetoresistive effects

The application of a perpendicular magnetic field has a variety of other geometrical effects on ballistic transportation in a 2DEG channel. An applied field can suppress back-scattering from the edges of, and defects in, the channel (fig. 8a and b). This results in a negative magnetoresistance, particularly at quantum point contacts.

The bend resistance is also field dependent. It is typically negative at small fields, zero at large fields and positive at intermediate values. The exact situation depends upon the geometry of the contacts involved, and in particular the radius of the current bend.

A magnetic field also suppresses weak localisation (see section 2.3.1. An electron path returning to its origin increases resistance by constructive interference. The penetration of flux quanta through the loop breaks the symmetry of the loop, and so induces a phase difference between the clockwise and anticlockwise paths.

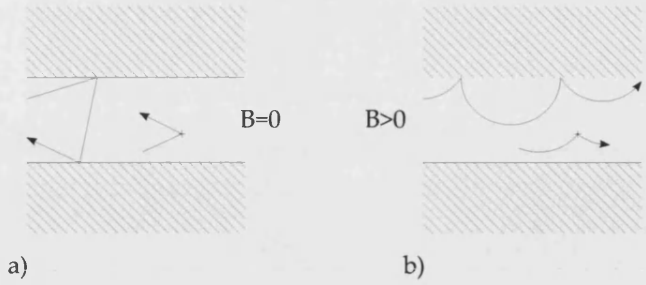

Figure 8. Scattering in a channel. a) The perpendicular field is zero. Back scattering occurs. b) A field is applied. Back scattering is suppressed.

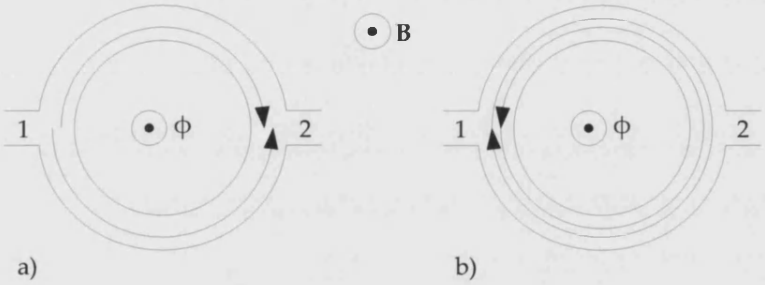

Figure 9. The Aharonov-Bohm geometry for electrons making a) a half circuit of the ring and b) a complete circuit.

The interference at the start point is therefore not, in general, constructive, and coherent backscattering does not occur.

Aharonov-Bohm oscillations

If a conducting ring is defined in a planar (metallic or 2DEG) substrate, as in fig. 9 then the paths from point 1 to point 2 are constrained to follow one of the two arms of the ring. In an ideally thin ring, there are only two paths available, and there is a matching of phases between the two paths. Interference is positive at point 2, and transmission from point 1 is increased.

A perpendicular applied field (B) introduces a phase shift between the arms of the ring of

$$\Delta\psi = \frac{e}{\hbar}\Phi, \tag{2.33}$$

where Φ is the enclosed flux, and is given by $\Phi = BS$. If this is $+\pi$ for one arm, and $-\pi$ for the other, then the total phase shift between the two arms is 2π, and the condition for constructive interference at 2 is still met. However, if the total phase shift between the arms is π, the interference will be destructive, and transmission will be reduced. This results in oscillations in the magnetoresistance of period

$$\Delta B = \frac{h}{e}\frac{1}{S}. \tag{2.34}$$

Interference between paths can also occur after a complete circuit of the ring (from point 1 back to 1). These oscillations will have period

$$\Delta B = \frac{h}{2e}\frac{1}{S}, \tag{2.35}$$

as the phase shift induced by the enclosed flux is

$$\Delta\psi = \frac{2e}{\hbar}\Phi. \tag{2.36}$$

In contrast to the oscillations due to half circuits of the ring, the phase of this effect is sample independent. In parallel or series arrays of rings, this means that the period $h/2eS$ oscillations remain, while the conductivity contribution from the period h/eS oscillations averages to 0.

This effect was first observed in a long aluminium cylinder[73]. As a cylinder is effectively a number of rings stacked on top of each other, only the period $h/2eS$ oscillations were observed. h/eS oscillations in a single ring were first observed by Webb *et al*[95], and explicit suppression of the $h/2eS$ oscillations in multiring geometries has also been observed[86]. In real samples, the width of the ring is finite, and so the frequency range of the observed oscillations is broadened.

Inhomogeneous magnetic fields

All the previous discussion concentrates on homogenous magnetic fields. This thesis is concerned with electron transport in inhomogeneous fields, primarily perpendicular to the field gradient, and so an introduction to the relevant physics is now presented.

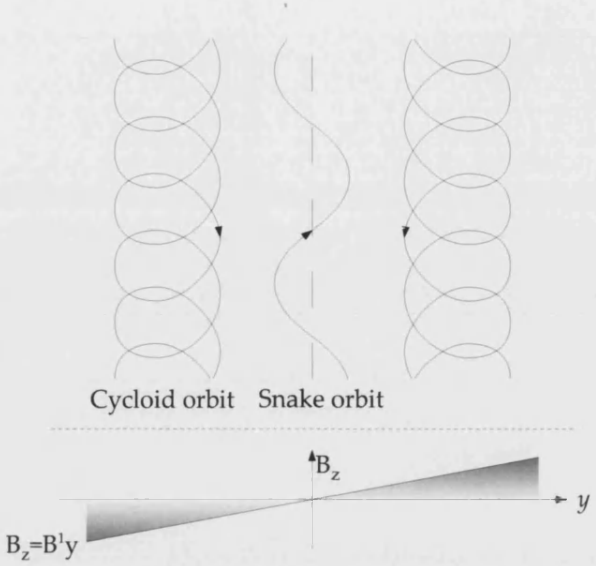

Figure 10. A magnetic field gradient guides the electrons in a channel in cycloid and snake orbits. Electrons in the two states travel in opposite directions.

A gradient of B_z across a current carrying channel can act to channel electrons, particularly around the zero field point if one is present. A semiclassical framework outlines the situation adequately, and is presented in fig. 10. In a channel with the zero field line down the middle and the field of different sign either side of the line, the Lorentz force on an electron moving down the channel will act in a different direction in each half of the channel. If the electron is moving one way along the channel then it will be forced towards the centre, regardless of which side of the stripe it is. These confined states can be parameterised by the angle at which they cross the $B_z = 0$ line and their "wavelength" – the distance between successive intersects of the electron trajectory and the zero field line. These two quantities are linked by the magnitude and profile of B_z.

This situation is not time symmetric. Positive and negative travelling electrons experience different confinements. If the electron moves in one direction, it will be confined to the centre line. If it moves in the other, it will be deflected towards the edges of the channel. This results in different magnetoresistance behaviour for the two directions of travel[44, 43, 29]. This is the subject of Chapter 4.

Other systems also show magnetoresistance effects. If the magnetic dot profile in a region of the channel is such that that $B_z = 0$ line forms a closed loop, then electrons can be trapped in edge states circulating this line. The trapping is strongest when an integer number of wavelengths fit around the loop. As above, the wavelength depends on the magnitude of the applied field, and so the trapping is periodic in B_z. This is observed as magnetoresistance oscillations[87].

Such systems can be realised by the deposition of micromagnets on the surface of the heterostructure. Dysprosium, cobalt and iron are all suitable ferromagnetic materials. These are then magnetised by the application of an external field (B_{app}). A thin wire of ferromagnet can produce a cross channel B_z profile with either one (if B_{app} is parallel to the plain of the 2DEG) or two (if B_{app} is perpendicular to the 2DEG) zero field lines. A circular closed zero field line can be created by a circular magnetic dot, which is magnetised by a perpendicular B_{app}. Fabrication methods are discussed in depth in Chapter 3.

2.3.6 *Spin transport in semiconductors*

The term *spintronics* was coined in 1996 and is used to describe devices in which the spin of the charge carriers is exploited. To achieve this, a nonequilibrium spin population is generally[71] required. Generating an equilibrium spin polarised current is easy – such a current flows naturally in a ferromagnet[54, 21]. Creating a spin polarised current in a non-magnetic material is more difficult. Also necessary is some way of detecting or manipulating the resultant spin polarised current.

Here, the techniques relevant to spin injection and transport in semiconductor-based 2DEGs are briefly described.

Spin injection

A number of techniques have been described to create a nonequilibrium spin poopulation in semiconductor devices, including optical polarisation[32] and spin filtering[28, 79]. Here, electrical spin injection is discussed, which is desirable for devices[93]. In this technique, a spin polarised *equilibrium* current is injected from a magnetic electrical contact into the semiconductor.

Ferromagnetic contacts can provide this source of spin current. Direct spin injection from ferromagnets into 2DEGs was originally proposed in 1990[16], but shows only small effects ($\sim$ 1%[24, 45]). This is due to the mismatch in conductivity between the two materials[72].

A tunnel barrier between the ferromagnet and the semiconductor can overcome this problem. This can be created using the Schottky barrier formed at the interface between the two materials, or alternatively by placing a thin layer of insulator – often MgO[94] – between them. This becomes the dominating resistance in the system, and removes the dependence of the spin injection efficiency on the relative resistances of the contact and semiconductor. Injection efficiencies of 55% have been achieved.

Alternatively semimagnetic semiconductors can be used as contacts, as they have resistances comparable with that of the semiconductor into which the spin is to be injected. Such materials consist of semiconductor lattices into which magnetic ions are incorporated[23]. Injection efficiencies as high as 80% at 4.8K[88] have been achieved.

Spin dependent transport

Although it is possible to probe the spin state of the current in a semiconductor using optical methods[cite], this is not often useful for devices. Some region with spin dependent transport properties is generally required. This is often done using another magnetic layer. In this, the resistance is much lower for the spin population aligned with the magnetisation than for those spins antialigned.

A simple device, therefore, can consist of a magnetic layer to inject the spin polarised current, a semiconducting layer in which the nonequilibrium spin population propagates, and another magnetic layer to detect the polarisation of the resultant current.

Spin relaxation

Once a non-equilibrium spin current has been injected into the semiconductor, the spin states relax towards the equilibrium. This relaxation is characterised by two different time scales. The *spin relaxation* time describes the change of the population of the two states towards equilibrium, and the *spin decoherence* time describes the loss of phase coherence in an initially coherent superposition of quantum states.

Typical spin relaxation times in GaAs/AlGaAs quantum wells are of the order of 100ps[59].

2.4 SUMMARY OF ELECTRON TRANSPORT

In this Chapter, we have described the formation of a 2DEG in a potential well created at the boundary between two different semiconductors. Such a 2DEG has a long mean free path (up

to $\approx 10\mu m$), a high mobility ($10^4 - 10^6 cm^2 V^{-1} s^{-1}$) and a low carrier density ($1 - 5 \times 10^{11} cm^{-2}$.

Electron transport in devices with length scales less than the mean free path is ballistic. Tranport is then affected by scattering from the boundaries of the 2DEG and weak localisation. Tansport through point contacts is quantised in units of e^2/h.

The application of a uniform magnetic field normal to the 2DEG results in the quantisation of the density of states into Landau levels, the separation of which is field dependent. As the transport coefficients are a function of the density of states at the Fermi surface, the resistivity of the 2DEG exhibits magnetoresistance oscillations as the field is swept and Landau levels pass through the Fermi surface.

The application of a field gradient to a 2DEG channel results in the formation of snake orbits along the zero-field line. This are time-asymmetric states which propogate in one direction only. Counterpropogating electrons are scattered away from the zero-field line. The formation of these states has implications fro magnetotransport in the 2DEG

A spin polarised current can be injected into a semiconductor from a ferromagnetic or semimagnetic semiconductor contact. The spin polarisation then relaxes as the current travels through the semiconductor. Application of a transverse magnetic field to the 2DEG results in Zeeman splitting of the energy levels.

3

SAMPLE FABRICATION AND EXPERIMENTAL TECHNIQUES

To observe quantum transport phenomena in a sample, it is generally necessary for it to be small and cold. Specifically, we need to ensure that the device has a similar characteristic size to the mean free path of the electrons in the 2DEG, which increases as temperature decreases. To do this, nanolithography techniques are used to fabricate the devices, and experiments typically take place at liquid helium temperatures (around 4.2K or lower).

In this chapter, the experimental methods used to fabricate the samples and obtain the results discussed in Chapters 4 to 6 are described.

3.1 SAMPLE FABRICATION

3.1.1 *Lithography*

Lithography is the process by which a pattern is transferred to the surface of a substrate. The sample is spin-coated with a *resist* which is typically a polymer in a solvent, which dries to form a highly crosslinked structure. Irradiation by the chosen method decreases the crosslinking and so increases the solubility of the polymer. The pattern is then developed in a suitable solvent, removing exposed areas. (Alternatively, a negative resist can be used, in which exposed areas are reduced in solubility.) The resist acts as a mask for subsequent steps, defining the area of the substrate to be processed.

Two types of lithography were used to fabricate the devices described in this work.

Optical lithography

Optical lithography uses electromagnetic radiation, usually from the UV part of the spectrum, to irradiate the resist. To select specific areas for irradiation, a physical mask with a pre-defined transparency pattern is used. This method allows the entire wafer to be exposed at once, allowing swift fabrication of large or repeated structures. The mask is usually fabricated by electron beam lithography (see below).

There are a number of different ways of transfering the pattern to the resist-coated substrate. The mask may be brought into

contact with, or close proximity to, the substrate. This method is simple but suffers from poor alignment and mask degradation. Alternatively, a number of projection systems are available. Lenses or mirrors are used to project a mask pattern onto the device. This gives the advantage of greater resolution, at the cost of increased complexity[52].

The resolution of an optical lithography system is limited by the wavelength of the light used. Successive generations of devices have moved to deeper and deeper UV light, with the latest experimental devices employing x-rays, and therefore being technically demanding. An alternative approach to extend the resolution of a system is to use liquid immersion lithography, in which the optical system is immersed in a liquid with a high refractive index. Liquid immersion systems are currently used to make 65nm pitch feature sizes, and 30nm pitch features fabricated using experimental systems have been reported[85].

For the devices described here, Shipley Microposit S1813 positive resist was used. Exposure was by contact lithography, using UV light from a unfiltered Hg vapour lamp. Smallest feature sizes achievable were around 1 μm.

Electron beam lithography

Electron beam lithography uses a directed beam of electrons, usually from the scanning beam of an electron microscope, to expose the resist. Polymethylmethacrylate (PMMA) is usually used as a resist. This process is much slower than optical lithography, but allows significantly smaller features to be defined. Resolution is limited by beam shape and back-scattering of secondary electrons from the substrate[52]. (Secondary electrons can be helpful for lift-off processes, by creating an undercut profile.)

With careful choice of resist and incident electron energy it is possible to write features as small as 3 to 5nm, but practical limits are defined by development of the resist and the process used to then transfer the pattern to the substrate. Isolated feature sizes of less than 10nm and periodic structures of pitch 30nm have been patterned[92].

3.1.2 *Deposition*

Deposition of metals on the surface of the substrate can be done by vapour deposition, in which a heated material is evaporated onto the substrate in a vacuum. The metal is placed in a boat or crucible. Evaporation is achieved either by the passing of a current through the boat, which is then subject to resistive heating, or by bombarding the material with an electron beam. Electron

beam evaporation has the advangtage of reducing contamination from the crucible, but is more complicated and can induce x-ray and ion damage in the substrate[47].

Alternatively, deposition can be carried out by sputtering, in which the target material is held at a negative potential and bombarded with positive inert ions. Ejected atoms are condensed onto the substrate, which is placed at the anode. This method results in slower deposition and better quality films. A wider range of materials can also be deposited.

After deposition, the resist and unwanted film are removed by an appropriate solvent. This step is aided by an undercut resist profile, which ensures a physical break in the deposited film.

3.1.3 *Ohmic contacts*

Semiconductors and metals both have bulk electrical properties which are good approximations to Ohm's Law – their resistance is independent of applied voltage. However, the contact between two such materials does not exhibit these properties. Instead, a Schottky contact is formed, in which charge carriers are depleted from the surface of the semiconductor, forming a barrier layer[38]. To make useful devices, it is necessary to engineer ohmic contacts between the two materials.

To achieve this, AuNiGe layered structures[9, 81] are deposited on the top surface of the AlGaAs/GaAs heterostructure. This is then annealed[81] in an oxygenless environment at around 400°C. During the annealing process, the heterostructure is penetrated by spikes from the deposited layers. If the spikes reach the heterojunction, then good electrical contact between the metal and the 2DEG results. Exact characteristics depend on the properties of the 2DEG, and the size and areal density of the spikes[8].

In the devices described here, a (bottom up – ie growth) recipe of $Ge_{60nm}Au_{90nm}Ni_{30nm}Au_{200nm}$ was used. Prior to deposition, the devices were immersed in a 1:1 mixture of $HCl : H_2O$ for 30s to remove any surface oxide layer. The structure was then annealed at 400°C in a hydrogen/nitrogen atmosphere.

3.1.4 *Etching*

To destroy the 2DEG in a region of the substrate, the heterostructure can be etched. Etching is the removal of the top layers of the heterostructure, in a region defined by lithography, to a certain depth. In AlGaAs/GaAs, removal of the structure down to the heterojunction (a *deep etch*, fig. 11b) has the desired effect, but this is not essential. Removal of the top layers, particularly the Si

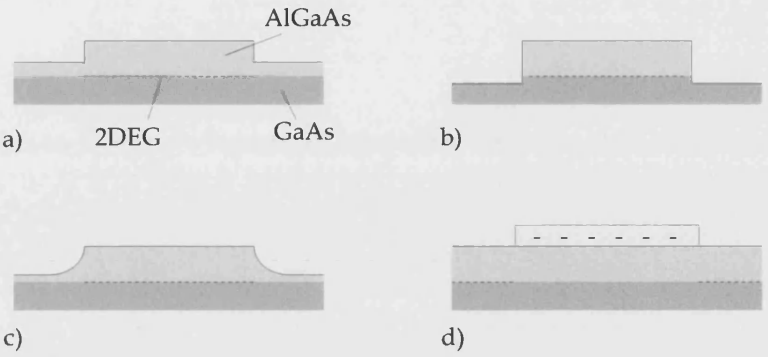

Figure 11. Processing of a semiconductor heterostructure to remove the 2DEG. a) Shallow dry etching (straight sidewalls). b) Deep dry etching (straight sidewalls). c) Shallow wet etching (curved sidewalls). d) 2DEG depletion by an electrostatic gate.

doped layer, will also deplete the 2DEG in the defined region (a *shallow etch*, fig. 11a)[5, 89].

Etching can either be performed by immersing the sample in a liquid etchant – *wet etching* – or by bombardment with vapour or plasma reactants – *dry etching*.

Wet etching

This is a chemical process, in which the sample to be etched is placed in an etch solution which reacts with the substrate. The rate of etching depends upon either the diffusion of reactants towards and away from the substrate (increased by agitation), or the reaction rate itself (increased by heating or an increase in reactant concentration)[47].

Wet etching is typically an isotropic process (although anisotropic wet etchants are available for some substrates). It therefore results in an rounded etch profile (fig. 11c) which undercuts the resist and increases the width of the feature to be etched. It produces no damage to the sidewall beyond the etched area. This makes it, in general, suitable for the etching of larger features.

For the devices described in this thesis, an etch solution of H_2O_2: NH_3: H_2O in the ratio 1:1:50 was used. This resulted in an etch rate of approximately $10nms^{-1}$.

Dry etching

When the etchant is in the gas or vapour phase, the process is termed dry etching. It has a number of advantages over wet etching. The etch is anisotropic, resulting in no undercut and better control of the dimension of the feature. (However, some damage to the sidewalls of the etch can result, decreasing the 2DEG mobility in that region. A damaged layer up to 60nm thick has been observed[13].) There are no surface tension problems, which, in wet etching, can prevent etchants from reaching the substrate.

The dry etching process has two components – chemical and physical. In our case, dry etching uses a plasma to dissociate the reactant gas and therefore form highly reactive radicals. This is termed Reactive Ion Etching (RIE). These reactive species are accelerated towards the substrate and either induce chemical reactions or physically remove layers from the substrate[47].

To etch the AlGaAs/GaAs substrate used for the devices described here, $SiCl_4$ was used. A plasma power of 50W resulted in an etch rate of around 100nm per minute.

Another use for plasma etching is the ashing of organic residue on the substrate. In this case, oxygen is used.

Depletion by an electrostatic gate

Regions of the 2DEG can also be depleted by the application of a negative voltage to an overlying electrostatic gate. In particular, this allows the width of a constriction to be varied by applying different voltages.

3.2 EXPERIMENTAL TECHNIQUES

3.2.1 *Low temperature techniques*

To keep devices at low temperatures during electrical measurements, temperature controlled cryostats are used (fig. 12). These essentially consist of a vacuum jacket surrounding a bath of cryogen, usually either liquid nitrogen or liquid helium. If liquid helium is used then this bath may be surrounded by a liquid nitrogen jacket. The cryogen is then either passed through a heat exchanger in close thermal contact with the sample, or directly over the sample. A heater on the sample mount allows steady temperatures above that of the cryogen.

Liquid He^4 has a boiling point of 4.2K at atmospheric pressure, making this the lowest achievable temperature with this cryogen unless the pressure in the sample chamber is reduced. This can be

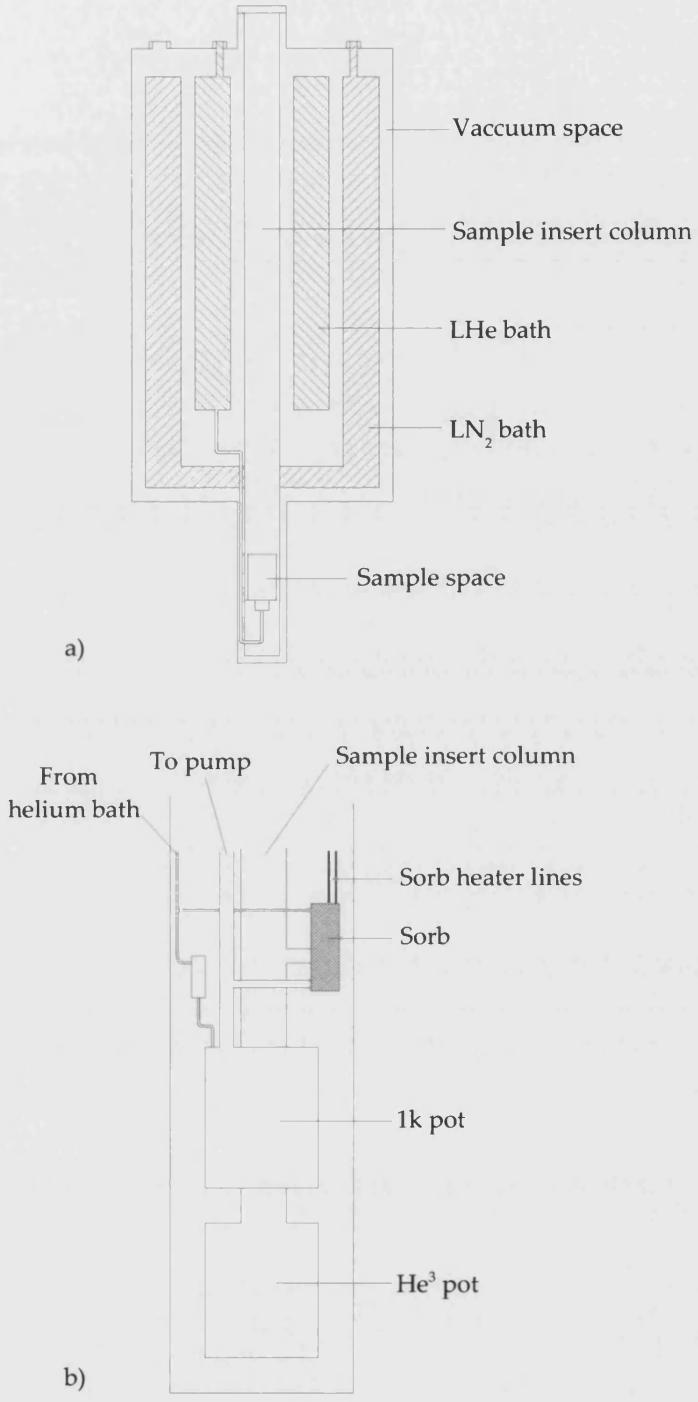

Figure 12. a) Schematic of a liquid helium temperature controlled cryostat. b) Schematic of a He_3 cryostat tailpiece.

done by pumping on the sample space, and allows temperatures as low as 1.3K to be reached.

If temperatures lower than this are required, then He^3 can be used (fig 12b). This has a boiling point of 3.2K at atmospheric pressure, but reducing the pressure can decrease this to 0.3K. A considerably more complicated cryostat (fig. 12b) is required – He^3 is expensive and is retained and recycled in the sample chamber. The gaseous He^3 is initially condensed by bringing it into thermal contact with a pumped He^4 reservoir (the "1K pot", which has a temperature of around 1.3K. The He^3 is then pumped on by a sorb. This is a material which adsorbs He^3 readily when below a certain temperature, but desorbs it above that point. By lowering the temperature of the sorb below the critical point, the pressure in the sample chamber is reduced and the temperature drops to 0.3K.

When the He^3 is all adsorbed onto the sorb, the temperature in the sample space begins to rise. At this point, the He^3 gas can be recycled by heating the sorb, to desorb it. It is once more in contact with the 1K pot, and so condenses. The cycle can then be started again.

To apply a magnetic field to the sample, a coil wrapped around the sample space is used. There are some advantages in using a superconducting coil for this – power consumption is lower as resistance in the coil is zero, and the magnetic field is steadier. Niobium-tin and niobium-titanium are often used for this application. However, a superconductor has to be cooled to below its transition temperature, usually using liquid helium. Furthermore, there is a limit to how strong a magnetic field a superconducting coil can support before the superconducting critical field density is exceeded – if fields above around 21T are required, either a resistive or hybrid magnet must be used.

3.2.2 *Electrical measurement techniques*

To measure the magnetoresistance of a semiconductor device, it is necessary to pass a known current through it while measuring the potential drop across it. This can be done by *two-terminal measurements*, in which the potential difference is measured between the same contacts that inject the current. However, in this case, a current is flowing through the voltage contacts. Therefore the measured potential drop has a component from the contacts.

This problem can be avoided by the use of *four-terminal measurements*. If the voltage is measured across two independent contacts to the sample, negligible current will flow through these. There will be no potential drop across them, and the measured voltage

will be across the sample only.

In the experiments described here, an approximately constant current was passed though the samples by putting a constant voltage across the sample in series with a resistance much larger than the sample resistance. Series resistance values of around $1 - 10M\Omega$ were used. Typical sample resistances were less than $10k\Omega$.

The application of a constant voltage results in a constant current – it is a *d.c. technique*. D.c measurements are necessary to measure rectification in a sample, but, in general, alternating current (a.c.) techniques are preferable, in order to increase the signal-noise ratio.

A. c. measurements involve the application of a voltage of a specific frequency, and the detection of a signal at that frequency. Selection of a frequency which is in a low-noise part of the spectrum ensures that the measured voltage is predominantly signal – a large signal-noise ratio is achieved. For example, the presence of mains loops in most laboratories suggests that a lot of electrical noise will be generated around 50Hz, and so this, and multiples/simple fractions of this, are frequencies to be avoided.

In the experiments described here, a current was passed through the sample using either the voltage output of a EG&G 5210 lock-in amplifier in series with a large ($\approx 1M\Omega$) resistance (for a.c. measurements), or a Keithley 220 current source (for d.c. measurements). The resulting signal voltage was passed through a pre-amplifier, which provided a gain of 10-100. This voltage was then read by the lock-in and passed to a Keithley 199 multimeter for GPIB readout (a.c), or read directly by the Keithley 199 (d.c.). GPIB instruments were controlled and read using a PC running LabVIEW.

LED illumination was provided by a burst current source. A Oxford Instruments ITC temperature controller was connected to the thermometer and heater inside the sample space.

A diagram of the experimental configuration is shown in fig. 13.

3.2.3 *Microwave irradiation*

Microwave irradiation of a sample was achieved using a cryostat insert with a circular cross-section millimetre-scale waveguide passing down the middle of it.

A backwards wave oscillator was used to generate the microwaves. In these, an electron beam from a cathode is passed through a slow-wave structure. The resultant microwaves are extracted near the cathode. The frequency depends on the accel-

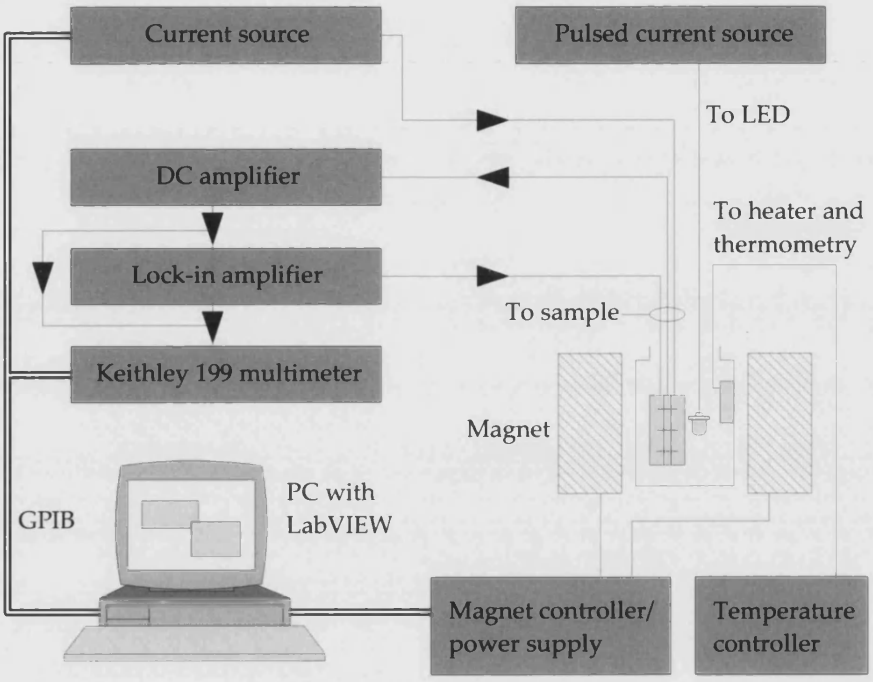

Figure 13. Experimental set-up used for the results presented in this Thesis. A.c measurements were performed using a EG&G 5210 lock-in amplifier coupled to a pre-amplifier. D.c measurements did not require the lock-in amplifier. The signal voltage was passed to a Keithley 199 multimeter for GPIB read-out. For current sweeps the Keithley 220 current source was controlled by the PC using GPIB, while the field sweeps were controlled via the Oxford Instruments magnet controller. Independent of the measurement electronics was the temperature controller and the LED current source.

erating voltage.

Microwave attenuation was performed using a rotary vane attenuator. These typically consist of three sections of waveguide, which have thin dielectric films mounted along their axis. These act to polarise the microwave radiation. The middle section is free to rotate, and, in conjuction with the other two sections, acts as a crossed polariser. The degree of attenuation depends upon the angle between the sections.

Radiative power can be measured as power relative to 1mW (dBm). Power is then given as $P_{dBm} = 10\log_{10}(P_{mW})$. This is therefore an absolute power measure.

3.3 MAGNETISED STRIPES

To impose a transverse field gradient on the 2DEGs in our devices, long thin dysprosium stripes were magnetised transverse to their axis. A discussion of the nature of the magnetisation process and the stray field resulting from such structures is now presented.

3.3.1 *Magnetisation process in ferromagnetic stripes*

Dysprosium is a ferromagnet, with a Curie temperature of 95K. It has a saturation magnetisation of 3.67T. Although bulk (i.e. with an aspect ratio of around 1) dysprosium will reach saturation in an applied field of around 2T[19], the high shape anisotropy that characterises the magetic stripes in these devices resulted in a much higher applied field at saturation magnetisation.

Typically, the stripes were about 200nm in width and depth, and around 10μm to 30μm long. They therefore had an aspect ratio of about 100, which leads to a high demagnetising field when magnetised in the transverse direction.

We can attempt to calculate an approximate value for the magnetic field needed to fully magnetise a typical dysprosium stripe. We need to apply a field *larger* than the demagnetising field, H_d. In S.I. units

$$H_d = NM_s, \tag{3.1}$$

where M_s is the saturation magnetisation. The demagnetising factor in the transverse direction for our structure is close to 1. We therefore calculate a value for $\mu_0 H_d$ of 4.63T.

This is an estimate for the minimum value for dysprosium wires of this shape. In fact, the actual value is likely to be greater than this.

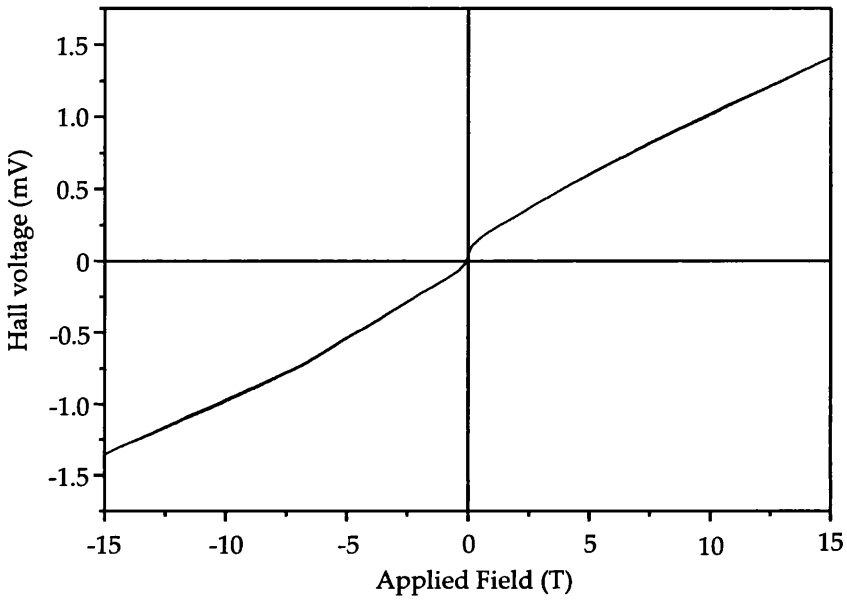

Figure 14. Hall measurements on a narrow (200nm) dysprosium stripe, showing the magnetisation curve with the field applied normal to the 2DEG (and therefore perpendicular to the stripe). The active area of the Hall probe was 2μm by 2μm. The field was applied in the plane of the 2DEG and perpendicular to the stripe.

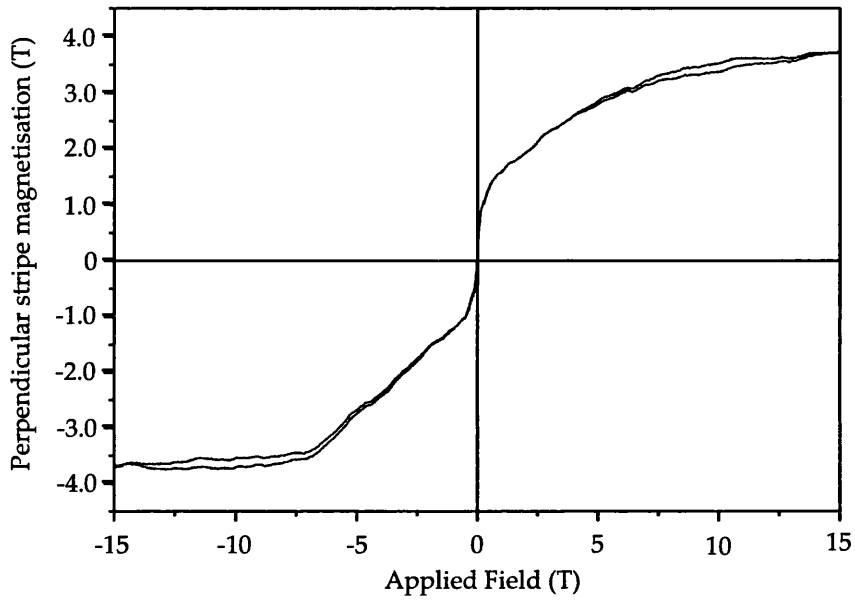

Figure 15. Transverse magnetisation curve for a narrow dysprosium stripe.

Similarly, the stripe would be expected to be made up of a single domain, as the exchange energy stored in the domain wall would tend to make such a configuration energetically unfavourable.

Experimental measurements of the magnetisation curve for a thin stripe deposited on a Hall probe made from an AlGaAS/-GaAs heterostructure are shown in figs 14 and 15. Fig. 14 shows the Hall curve for a 200nm wide stripe deposited on an AlGaAs/-GaAs Hall bar. The active area of the Hall probe was 2μm by 2μm.

In this configuration, the stray field from the stripe lies mostly within the channel of the Hall bar. The average field in the bar is therefore much smaller than the field directly below the stripe, but a sufficient proportion of the field profile lies outside the active area to ensure that a magnetisation curve is observed. Furthermore, this proportion is independent of the magnetisation of the stripe.

Fig. 15 has the slope due to the applied field removed. It is also normalised to 3.67T, the saturation magnetisation of dysprosium. It is this magnetisation curve that we use for analysis of results discussed in the subsequent chapters.

3.3.2 *Magnetic field profile beneath magnetised stripes*

The magnetisation of a ferromagnetic stripe deposited on a heterostructure results in a modulation of the applied field at the level of the 2DEG. The two-dimensional nature of the sheet of electrons means we only need to consider the component of the field perpendicular to the 2DEG, which we lable B_z. For an infinitely long stripe of height 2c, width 2a and magnetisation M, the field component a distance z below the middle of the stripe is given by

$$B_z = \frac{M}{2\pi}\left(\arctan\left(\frac{x+a}{z-c}\right) - \arctan\left(\frac{x-a}{z-c}\right) - \arctan\left(\frac{x+a}{z+c}\right) - \arctan\left(\frac{x-a}{z-c}\right)\right) \tag{3.2}$$

for magnetisation parallel to the 2DEG, and

$$B_z = \frac{M}{2\pi}\left(\sqrt{\frac{(z+c)^2+(x-a)^2}{(z-c)^2+(x-a)^2}} - \ln\sqrt{\frac{(z+c)^2+(x+a)^2}{(z-c)^2+(x+a)^2}}\right) \tag{3.3}$$

for magnetisation normal to the 2DEG. This geometry and the field profile for these two cases is shown in fig. 16. Note that, in the case of parallel magnetisation, the average field in the region immediately beneath the stripe is zero.

Two useful approximations to these field profiles can be made (fig. 17). In the first of these, we approximate regions of positive and negative field with constant functions of magnitude M_1 and M_2. This is the *step function approximation*, and has the useful feature that the cyclotron radius in each area is constant. This approximation therefore allows easy analysis of ballistic electron trajectories if a semi-classical model is used.

If the magnetic structure has been magnetised by an applied field perpendicular to the 2DEG, B_{app}, then the field values in these regions will be the sum of B_{app} and $M_{1,2}$. These values will then not necessarily be of opposite sign.

Alternatively, we can approximate the field profile to a line of constant gradient. This *linear approximation* is particularly useful for the field under a stripe magnetised parallel to the plane. It leads to a more accurate analysis of electron orbits confined to the zero field line.

For the sake of clarity, the nomenclature used when describing electrons in field gradients with a $B = 0$ line in the middle of the channel is now set out. An electron travelling along the channel in the direction such that the Lorentz force confines it to the middle of the channel is described as travelling in the *positive* direction. Conversely, an electron travelling so it would be forced to the edges of the channel is travelling in the *negative* direction.

Note that a reversal of the magnetisation of the stripe swaps the positive and negative directions of travel.

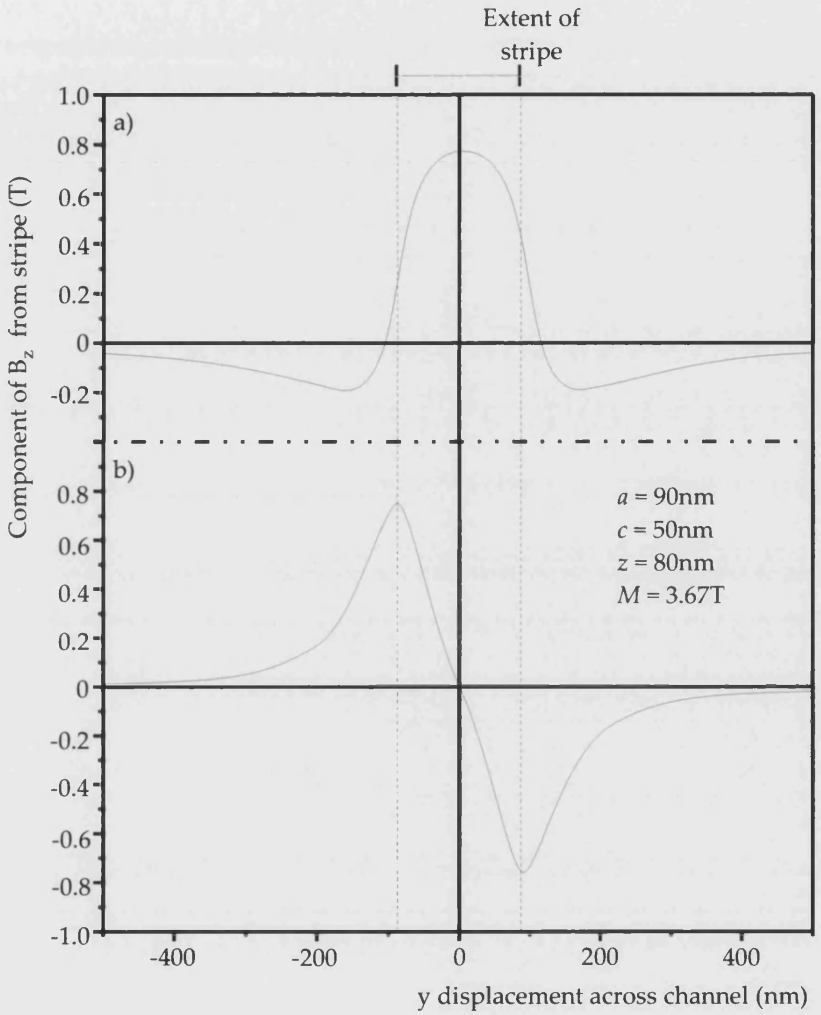

Figure 16. a) Exact form of the field beneath a stripe magnetised perpendicular to the 2DEG. b) Exact form of the field beneath a stripe magnetised parallel to the 2DEG. Both plots are for a 100nm deep and 180nm wide magnetic stripe, with the 2DEG 30nm below the surface of the heterostructure.

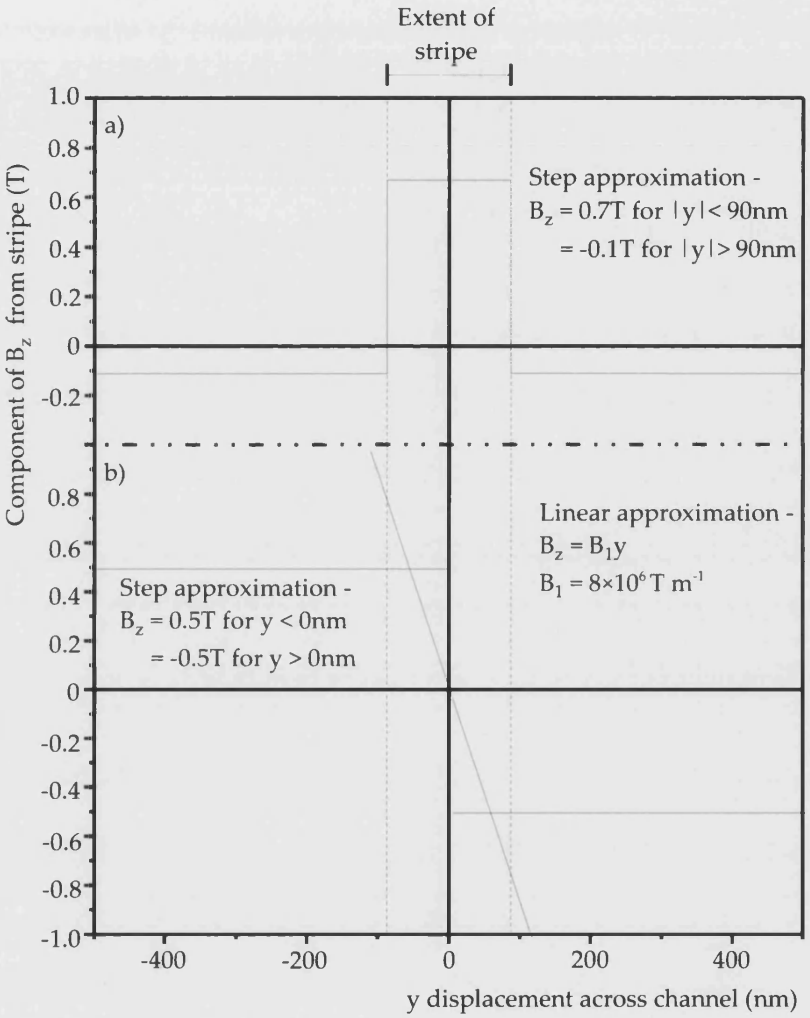

Figure 17. a) Step approximation for the field beneath a stripe magnetised perpendicular to the 2DEG. b) Step and linear approximations for the field beneath a stripe magnetised parallel to the 2DEG.

3.4 SUMMARY OF EXPERIMENTAL METHODS

Devices were fabricated using electron beam and optical lithography. Wet and dry etching was used to remove regions of 2DEG, and thermal evaporation to deposit regions of metals. This allowed fabrication of features down to 100nm in size.

The devices were then cooled to 0.3K using He^3, or 4.2K using He^4. This reduced electron scattering from thermal phonons, and increased the mean free path. Application of fields up to 13T was performed using a superconducting coil. This was uysed to magnetise nanomagnetic structures on the heterostructure, resulting in the imposition of a non-uniform B_z at the level of the 2DEG.

Electrical measurements were generally done using independent voltage and current contacts - a four point measurement. This has the advantage of removing contact resistance from the measurements. IV curves were necessarily taken using d.c. techniques, but a.c. techniques were used if possible due to the resultant reduced noise.

4

RECTIFICATION IN MAGNETIC CONFINING POTENTIAL

Previous experiments[43, 29] have shown evidence of asymmetric magnetoresistance in a transverse field in channels with a longitudinal ferromagnetic stripe overlaying them. The magnetisation of the stripe results in a steep gradient in B_z across the channel. The asymmetric behaviour can be intuitively understood in terms of the formation of snake orbits by electrons travelling in one direction only in the channel. It has been modelled in more detail in terms of the contribution by snake orbits to the conductance[29] and interactions with phonons in the asymmetric confining potential[43].

These studies used channels with typical widths of around 2μm. In the work presented here, a much narrower channel, with a width of around 200nm, was used. The intention of this was to concentrate on those orbits most tightly confined to the zero field line, and so remove any background contribution to the conductance from magnetoelectric states. The magnetoresistive and Hall behaviour of such quasi-1D wires has been observed to be different from the 2D behaviour[69].

In the following discussion, *stripe* is used to describe a long, very narrow ferromagnetic structure. A region of heterostructure designed and defined in order to carry a current along a particular axis is termed a *channel*, and the combination of the two is called a *wire*.

4.1 LITERATURE REVIEW

Nogaret *et al*[1] measured the magnetoresistance of 2μm wide channels with 500nm wide stripes superimposed, made of either Fe or Ni. The perpendicular applied field was swept between 1T and −1T and a number of different gate voltages applied. This resulted in a B_z field profile with two zero field lines.

A peak in the magnetoresistance was observed at 32mT for the Fe structures and 13mT for the Ni structures. The peak was independent of gate voltage, suggesting that it is entirely due to the magnetic modulation. The results are well described by a drift-diffusion model.

This system was further explored by Lawton *et al*, who used stripes of Ni, Fe and Dy. Material dependent peaks in the magne-

toresistance were observed, with the peaks being at highest fields for Dy and lowest fields for Ni. To confirm that the peaks orignate in the field modulation due to the stripe, the temperature of the Dy device was raised above its Curie temperature to destroy its ferromagnetism. This quenched the peaks.

Kubrak *et al*[41, 42] investigated transport perpendicular to a magnetic field gradient by depositing both stripes and films across a narrow constriction in a 2DEG channel. These were then magnetised both transversely and perpendicularly, resulting in different shaped magnetic barriers. The magnetoresistance of these devices was explained in terms of ballistic transport through the barrier.

Hara *et al*[29] used a transversely magnetised Co stripe. It was 500nm wide and 75nm deep, and positioned over the centre of a 1.5μm/1.8μm wide channel. The device was made in such a way that the magnetisation state of the Co wire could be probed by electrical transport measurements. The magnetic field was swept between 1T and −1T.

D.c magnetoresistance measurements were made under different bias conditions. Their results are shown in fig. 18a. Switching of the field or the current had a similar effect of the differential resitance. This results was ascribed to transport in snake states affecting the amount of e-e and boundary scattering events experienced by counter-propogating electrons.

Grabecki *et al*[27] used a slightly different micromagnet configuration to exert a field gradient on the channel in their devices. Two ferromagnetic layers were deposited either side of the channel and then transversely magnetised, resulting in a field gradient in the region between them. The channel width was around 1μm.

The bend resistance of the channel was measured between applied field values of 2.5T and −2.5T. Results are shown in fig. 18b, and were explained well by a semiclassical model in which the electrons are considered to propogate ballistically in a magnetically modulated billiard.

Theoretical studies of electron transport in field gradients have been done by Müller[55], and Reijniers and Peeters[64]. Müller described the effect on the energy bands and charge densities, and determined that the electron transport in these systems becomes quasi-1D. Reijniers and Peeters confirm this by analysis of the energy spectrum of the system.

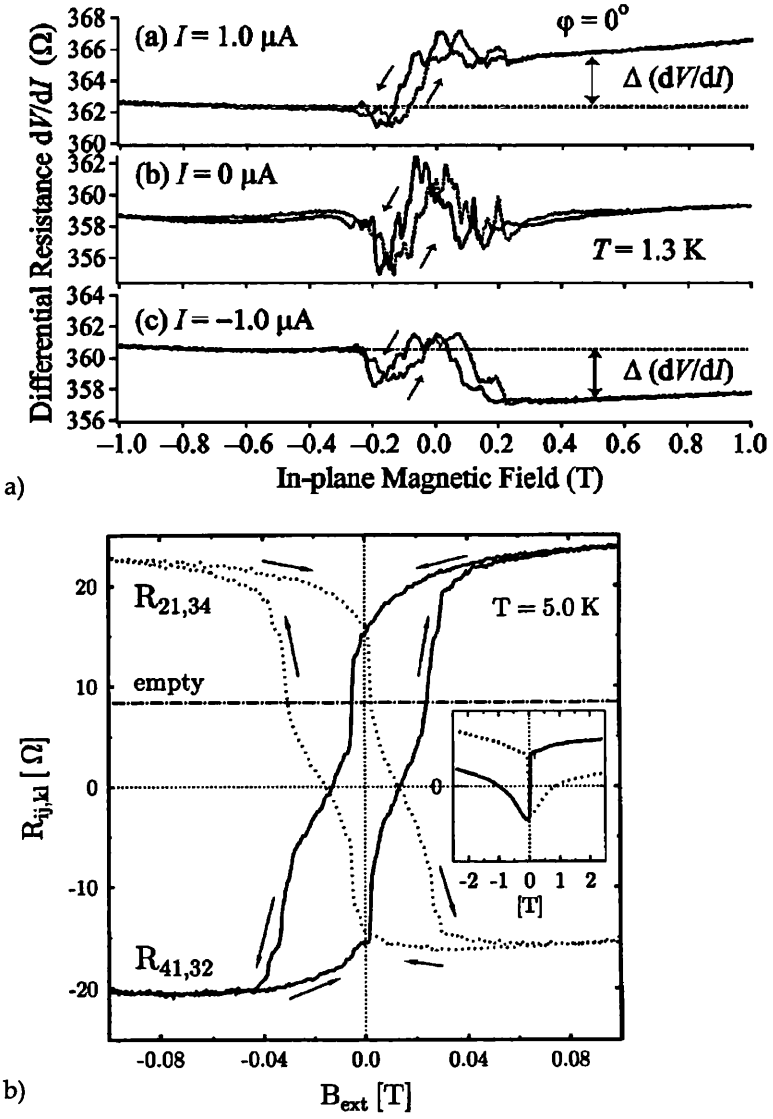

Figure 18. a) Differential in-plane magnetoresistance of a channel modulated by a cobalt stripe at different currents. From Hara *et al*[29]. b) Bend resistance as a function of in-plane magnetic field around 0T for a channel with lateral ferromagnets. Inset shows high field data. From Grabecki *et al*[27].

4.2 DEVICES

In order to concentrate on those electron orbits subject to the magnetic field gradient, devices with a very narrow conducting channel were fabricated (fig. 19). Such devices would explore a different regime than those described above, with a larger field gradient and quasi-1D transport. Using the techniques described in Chapter 3, a Hall channel 2μm wide was fabricated, and Ohmic contacts added to serve as current and voltage probes. A stripe of nominal width 180nm was then defined using EBL and 150nm of Dy was thermally evaporated.

This stripe was then used as an etch mask for a further stage of etching. This time, a dry etch was performed by RIE. Resist was used to mask the contacts to the channel, to preserve the 2DEG in these regions. This resulted in a narrow channel approximately the same width as the ferromagnetic stripe. (Sidewall damage during the etch probably produced a channel with a slightly smaller effective width than the stripe.)

The length of the ferromagnetic stripe was 36μm, and the depth of the heterojunction beneath the semiconductor surface was 30nm. Contacts were spaced along the length of the wire such that channel lengths of 2μm, 4μm, 8μm and 16μm could be probed. The sample layout and the labelling scheme for the contacts is shown in fig 20. Not all contacts were Ohmic upon cooling down of the device, which somewhat limited the measurements that could be performed.

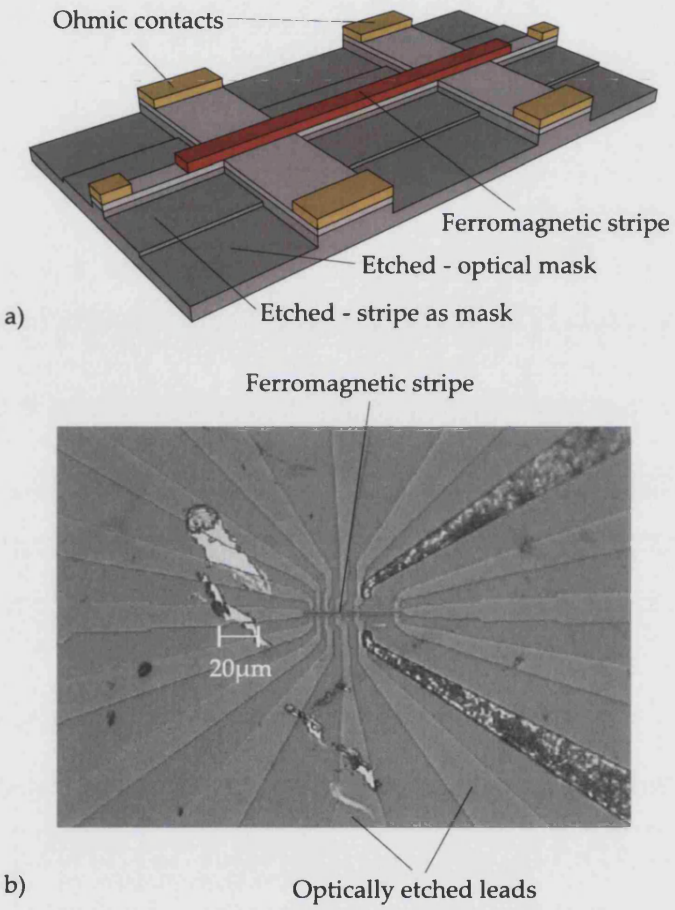

Figure 19. a) Schematic perspective view of the narrow channel device.
b) Optical micrograph of the device.

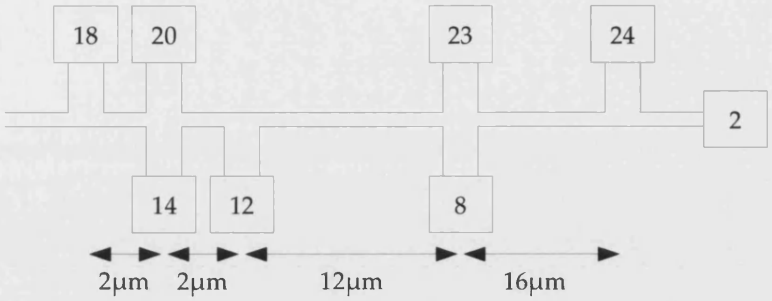

Figure 20. Schematic of the narrow channel sample used, including the labelling scheme for the contacts.

4.3 EXPERIMENTS

The sample was mounted on a rotation stage and cooled to 0.3K using a pumped ^{3}He cryostat. It was then briefly illuminated with a red LED, to excite some carriers from the DX centres, but not all. Illumination in very brief steps allows rudimentary control over the electron density in the 2DEG. Magnetic fields were applied using a superconducting magnet.

4.3.1 *Field applied parallel to sample*

The sample was accurately levelled by sweeping the field and measuring the Hall voltage under the stripe. When the applied field was parallel to the 2DEG, the Hall voltage should be approximately zero for all values of H. This is because neither of the components of the field perpendicular to the 2DEG contribute to V_H; the component of the normal field due to H is zero, and the component due to the stray field from the stripe is symmetric about the centre of the Hall channel, and averages to zero over the width of the channel (see section 3.3.2). It therefore also does not contribute to the Hall voltage[58], although the situation for an asymmetric flux distribution is more complicated[6].

The V_H curves do, in fact, show some structure, but levelling was achieved by ensuring the Hall curve was symmetric around $H = 0$.

Magnetoresistance measurements were made over 2μm and 16μm channel lengths, and IV characteristic measured over a 2μm channel length.

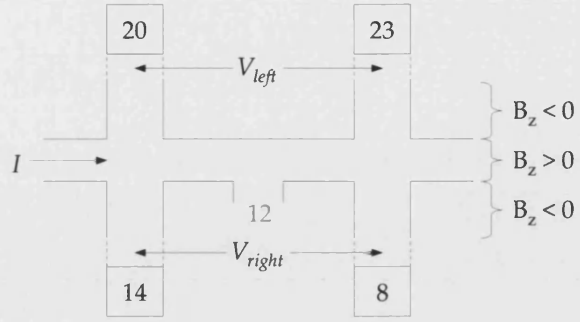

Figure 21. Contact configuration for probing both sides of the narrow channel device simultaneously.

4.3.2 *Field applied perpendicular to sample*

The sample was also orientated so that the applied field was normal to the plane of the 2DEG. This time, the correct orientation of the sample was ensured by maximising the Hall voltage for a fixed applied field. As the component of the field normal to the plane is given by $H\sin\theta$, maximising this ensures $\theta = 90°$.

Magnetoresistance measurements were first made to determine the Shubnikov-de Haas period. Using equation 2.32 the period of these oscillations can be linked to the electron density in the 2DEG, and so to the Fermi energy and wavevector.

Subsequent measurements in this sample orientation were made to both sides of the channel simultaneously, using opposing pairs of contacts. Specifically, contacts 14 and 8 were used to probe one side of the channel, and contacts 20 and 23 the other. Current was injected between contacts 18 and 2. This geometry is shown schematically in fig. 21.

This method was used to simultanously probe two regions with opposite magnetic field gradients. The main requirement for the approach to be appropriate was that contacts on one side of the channel were coupled significantly more strongly to orbits confined to that side of the channel. This assumption is discussed further in section 4.5.3.

Measurements were also made injecting a current from contact 18 to contact 12 and measuring the resultant voltage using the same contacts as above.

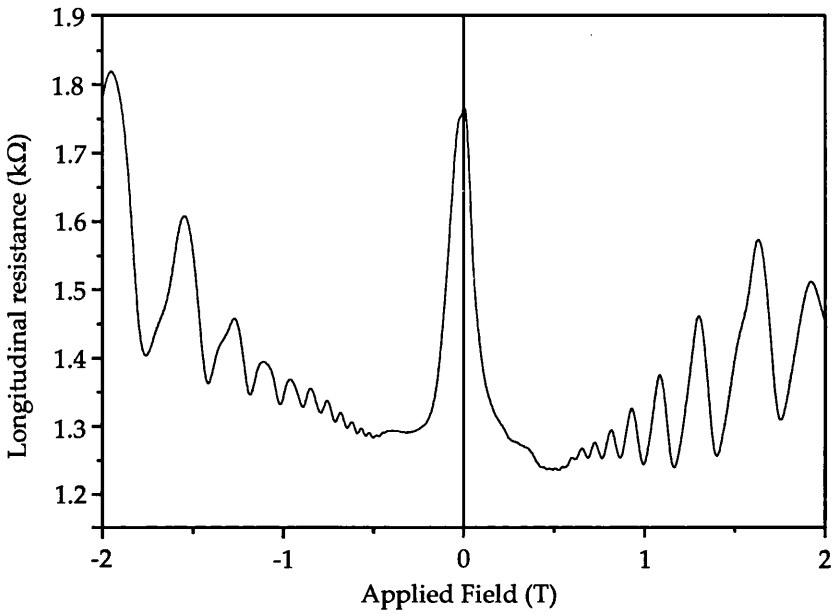

Figure 22. Longitudinal resistance measurements on narrow channel devices over a channel length of 2μm. The field was applied perpendicular to the 2DEG, and Shubnikov-de Haas oscillations are clear. T = 0.3K.

4.4 RESULTS

Magnetoresistance measurements between −2T and 2T, showing Shubnikov-de Haas oscillations, are shown in fig. 22. The frequency of these oscillations is used to determine the electron density and Fermi energy in section 4.5.1.

IV curves are plotted in fig. 23 for a channel length of 2μm. Curves are shown for applied fields of ±12T and 0T.

Comparisons can be made between the curves for the three field values in different field regimes. The data for $\mu_0 H = 0$T show the lowest voltage, and hence the lowest resistance, in all field regimes. The ordering of the resistance values for $\mu_0 H = \pm 12$T is swapped over for positive and negative fields. The data therefore show rectification-like behaviour dependent upon applied field direction.

These results also suggest a positive, but asymmetric, magnetoresistance. There is also some inherent rectification visible in the $\mu_0 H = 0$ curve.

Longitudinal magnetoresistance measurements are shown in

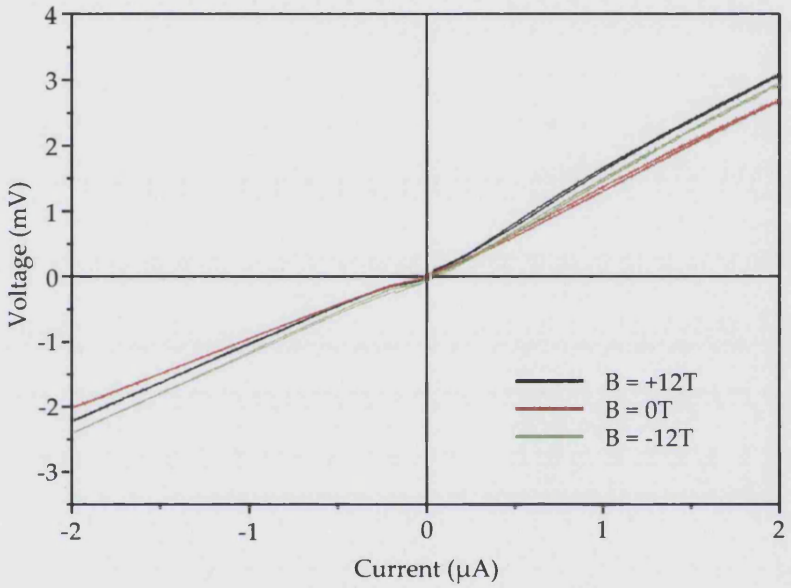

Figure 23. IV measurements of narrow channel device, over 2μm. Curves for $\mu_0 H = \pm 12T$ and 0T are shown. The current was injected betwen contacts 18 and 2 and voltage measured between contacts 14 and 12. The field was applied parallel to the 2DEG. T = 0.3K.

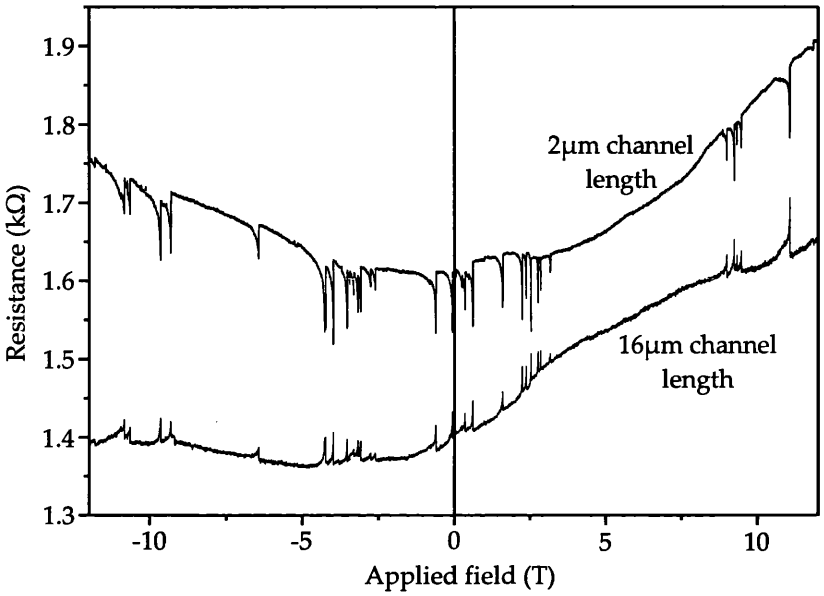

Figure 24. D.c magnetoresistance measurements of narrow channel device, over channel lengths of 2μm and 16μm. A current of 2.5μA was injected betwen contacts 18 and 2 and voltage measured between contacts 14 and 12 and contacts 23 and 24 respectively. T = 0.3K.

fig. 24 for 2μm and 16μm channel lengths. For both sets of data, resistance is close to or at its minimum value at an applied field of $\mu_0 H = 0$T. It increases more rapidly for fields applied in the positive direction than for those applied in the negative direction. Therefore, this confirms that the magnetoresistance is positive and asymmetric.

The degree of asymmetry is greater in the data for the 16μm channel length. Indeed, the resistance at negative applied field changes little.

The sample was then rotated so the applied field was perpendicular to the 2DEG. Magnetoresistance measurements were made on both sides of the channel. The current was passed from contact 18 to contact 2, and the potential measured between contacts 14 and 8, and contacts 20 and 23. Fig. 25 shows these data, with a full field sweep (both up and down) between −12T to +12T shown.

The polarity of the current was then reversed, and another field sweep performed. The results are plotted in fig. 26. In these

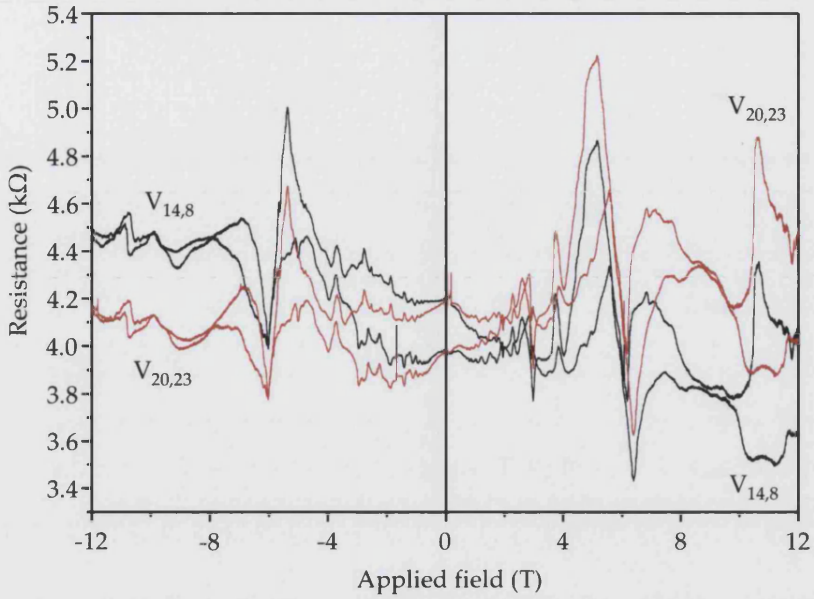

Figure 25. D.c. magnetoresistance measurements on both sides of the channel for a perpendicular applied field. A current of 2.5μA was passed from contact 18 to contact 2. T = 0.3K.

two plots there are a number of common features. In both cases, the resistance at $\mu_0 H = 0T$ is the same in both the left and right side of the channel. The two are different at non-zero applied fields, and of different signs for positive and negative fields. The difference between the sides of the channels is analysed at greater length in section 4.5.3.

As well as the difference between the sides of the channel, oscillatory features are present in the individual data sets. This is particularly so below about $\mu_0 H = 7T$ – above this field oscillations decrease markedly. Oscillations are larger in the data for positive currents.

With the sample still in the perpendicular orientation, IV measurements were made. The current was swept from $-2.5\mu A$ to $+2.5\mu A$ at applied field values of $\mu_0 H = -12T$, $\mu_0 H = 0T$ and $\mu_0 H = +12T$. The data are plotted in fig. 27.

We first note that the IV curves for the different sides of the channel for $\mu_0 H = 0T$ are the same. This confirms that resistance differences are a magnetic effect.

In the plots for $\mu_0 H = \pm 12T$, resistance ordering of the channels depends upon the polarity of the current and the direction of the

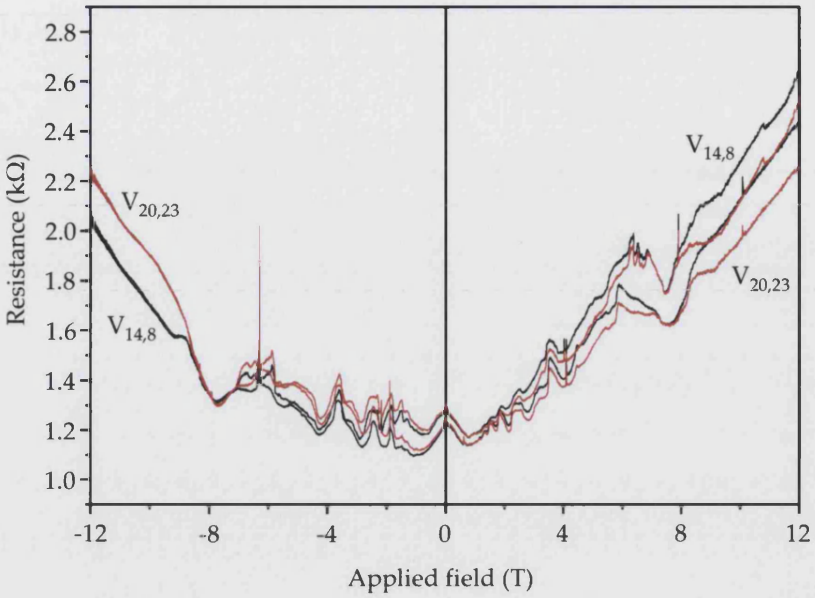

Figure 26. D.c magnetoresistance measurements on both sides of the channel for a perpendicular applied field. A current of 2.5μA was passed from contact 2 to contact 18 (the opposite polarity than for the reults shown in fig. 25. T = 0.3K.

applied field – reversing either will reverse the ordering. However, reversal of the current does not result in the same magnitude of resistance difference – there is some asymmetry in the IV behaviour. This is explored further in section 4.5.3.

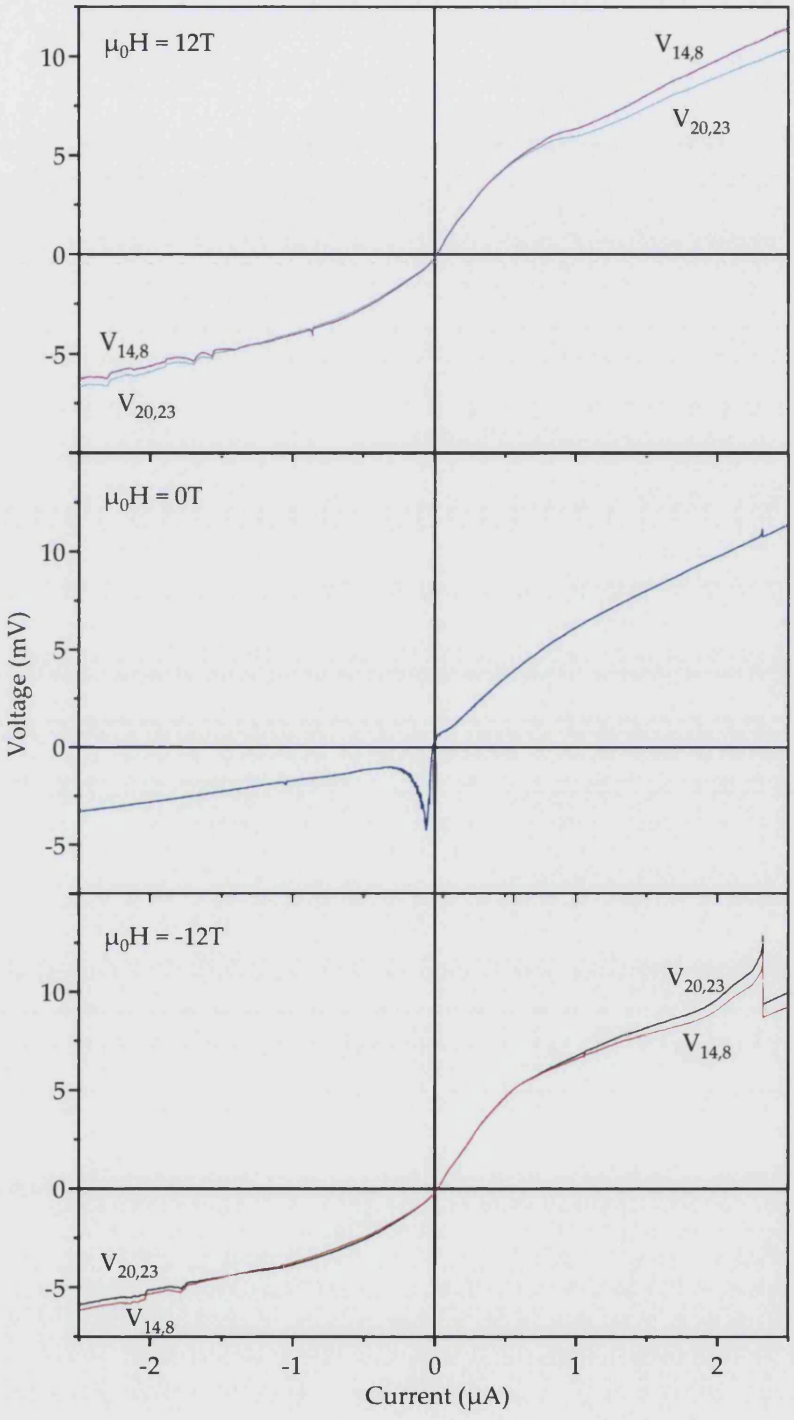

Figure 27. IV measurements on both sides of the channel for a perpendicular applied field. Plots are shown for applied field values $\mu_0 H = 12T$ (top) $\mu_0 H = 0T$ (middle) and $\mu_0 H = -12T$ (bottom).

4.5 ANALYSIS

4.5.1 *Device characterisation*

The frequency of the Shubnikov-de Haas oscillations, which are shown in fig. 22, can be used to determine the electron density in the 2DEG. From equation 2.32, the oscillations are periodic in 1/B. Plotting values of 1/B for successive resistance minima (fig. 28) gives a straight line of gradient

$$\frac{e}{h}\frac{g_s g_v}{n_s}. \tag{4.1}$$

In this case, $g_s = 2$ and $g_v = 1$. The gradient is found to be $0.157T^{-1}$, and so we determine a value of $n_s = 3.38 \times 10^{11}cm^{-2}$ for the electron density and $k_F = 1.46 \times 10^6 cm^{-1}$ for the Fermi wavevector.

From equation 2.11, the Fermi energy is therefore $E_F = 1.93 \times 10^{-21}J = 12.1meV$.

4.5.2 *Theoretical model of channel conductance – transverse stripe magnetisation*

We seek to explain the observed positive but asymmetric longitudinal magnetoresistance of the channel, as plotted in fig. 24. We have developed a model based on calculating the number of available conduction channels in the potential.

Modelling of magnetically modulated channel

Landauer theory (as discussed in detail in section 2.3.4) describes the conductance of a narrow channel in terms of the transverse modes present in the channel. For the calculation of the number of modes, the channel is generally assumed to take the form of a square potential well, but this need not necessarily be the case. In this model, we consider the number of modes in a 2DEG region in which the potential has a component from channel and a component from a magnetic field gradient.

For this analysis, the magnetic field is approximated to a linear form, as described in section 3.3.2. The perpendicular part of the field is given by

$$B_z = B_1 y. \tag{4.2}$$

The Hamiltonian of the system is given by

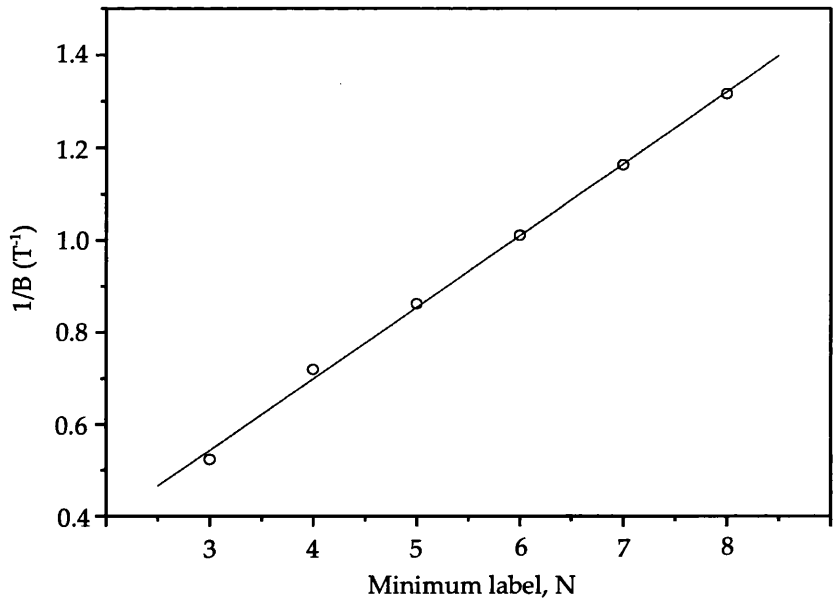

Figure 28. Shubnikov-de Haas minima for the narrow channel devices plotted against 1/B. The x-axis is the index N in equation 2.32.

$$H = \frac{1}{2m}\left(\hat{p} - \frac{qA}{c}\right)^2, \tag{4.3}$$

where $\hat{p}$ is the canonical momentum operator and A is the vector potential, defined by $B = \nabla \times A$[39]. By selecting

$$A = -B_1 y^2 \hat{x} \tag{4.4}$$

and setting $\hat{p} = \hbar k_x$, the magnetic potential[55] is shown to be of the form

$$V = \frac{1}{2m}\left(\hbar k_x - \frac{eB_1}{2c} y^2\right)^2. \tag{4.5}$$

This is shown in fig. 29 for positive and negative values of k_x and a field gradient of $5 \times 10^6 Tm^{-1}$. This potential modulates the channel, which is represented in this model by a square well[5]. This combined potential from the channel and the magnetic field gradient is shown in fig. 30. The potential is plotted for $B_1 = 5 \times 10^6 Tm^{-1}$ and $B_1 = -5 \times 10^6 Tm^{-1}$.

The two potentials plotted in fig. 30 are also for $k_x = \pm k_F$, as well as opposite field gradient. Therefore electrons travelling in the positive and negative directions experience a different environment, and swapping the direction of the current is similar to changing the polarity of the field gradient. This corresponds closely with the semiclassical orbits, with electrons travelling in the positive direction channeled in snake orbits along the $B = 0$ line, and negative-going electrons travelling in skipping orbits along the edge of the channel.

Each potential is relocated so the minimum potential at $V(x) = 0$, and the transverse modes in each potential can be calculated by solving the one-dimensional Schrödinger equation,

$$-\frac{\hbar^2}{2m}\frac{d^2\psi(x)}{dx^2} + V(x)\psi(x) = E\psi(x). \tag{4.6}$$

The eigenfunctions in the potential cannot be determined analytically, but can be calculated numerically. This was done using a Fortran program, listed in Appendix A. The approach used is now described.

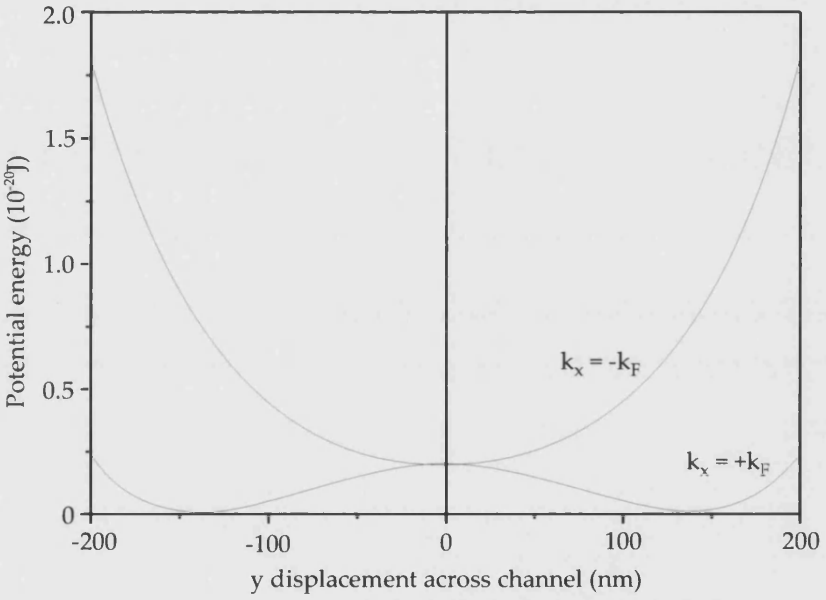

Figure 29. Magnetic potential due to a perpendicular field of constant gradient. Plots for $k_x = \pm k_F$ are shown, with, as for the sample described above, $k_F = 1.46 \times 10^6 cm^{-1}$.

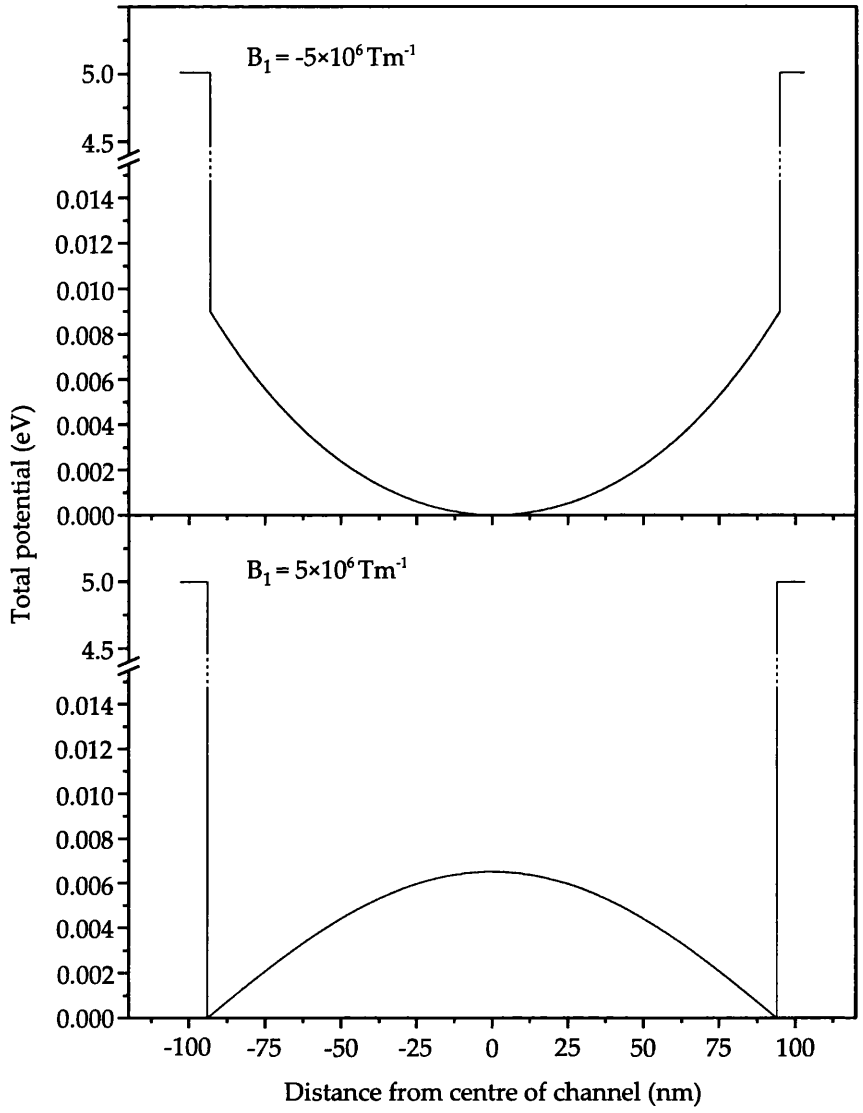

Figure 30. The form of the potential from both the confining channel and the magnetic field gradient. The potentials for $B_1 = 5 \times 10^6 Tm^{-1}$ (bottom) and $B_1 = -5 \times 10^6 Tm^{-1}$ (top) are plotted. Note the two different y axis scales. $k_F = 1.46 \times 10^6 cm^{-1}$. Classically, the attractive potential (upper panel) corresponds to snake states guided down the middle of the channel, whilst the repulsive potential (lower panel) corresponds to transport in edge states.

Numerical calculation of eigenvalues

To calculate the eigenvalues in the magnetically modulated potential, a 'shooting' algorithm is used[49, 83]. The eigenfunctions are described by the Schrödinger equation. In this approach an initial energy, which is expected to be too low, is selected. The wavefunction for that energy is calculated stepwise across the potential, starting at the centre of the well.

The potential is assumed to be symmetric about the centre point, and so the wavefunction is either antisymmetric or symmetric[25]. Therefore, either the wavefunction or the derivative of the wavefunction is zero at the centre of the channel. This condition acts as a starting point for the calculation of the wavefunction. The boundary condition $\psi(x \rightarrow \pm\infty) \rightarrow 0$ is imposed.

In general, the selected energy will not be an eigenenergy of the Schrödinger equation for the potential. The wavefunction therefore diverges outside the well, either to large positive or large negative values. The trial energy is increased by a small amount ΔE, and the wavefunction recalculated. This is repeated until the divergence of the wave function changes sign – in other words, if it diverged to high positive values on the previous iteration it now diverges to negative values, and vice-versa. This happens when the correct energy has been overshot.

The trial energy is now reduced by $\Delta E/2$, and the wavefunction (and its divergence) recalculated. In this way, a value for the trial energy as close to the eigenvalue as required can be determined.

Limitations and improvements

This is a relatively simple algorithm, and can be applied only to a very limited number of systems. The primary restriction is that the confining potential must be symmetric. This condition is imposed by the assumption that wavefunction is either symmetric or antisymmetric, which makes it considerably easier to calculate a reasonable starting point for the wavefunction and its derivative.

However, if the potential is asymmetric, it is possible to take a more sophisticated approach to finding a starting point, which allows the stepwise evolution of the wavefunction to start at high positive or negative values of position.

A more minor problem is that the algorithm does not always distinguish between energies that are close together – if they are closer than the change in energy between iterations, then an eigenenergy can be skipped. This can be avoided by selecting a smaller energy change (an approach which carries with it a speed penalty) and is usually noticed if the forms of, and number of nodes in, the resultant wavefunctions are plotted.

Finally, the resultant wavefunction is not normalised. This can, however, be easily done numerically. In this case it was not necessary to do so.

Modes in our device

For the parameters describing our device, the eigenenergies and forms of the conducting modes are shown in figs 31 and 32. Fig. 31 shows a positive field gradient, and fig 32 depicts the situation for a negative field gradient.

The wavefunction is very close to zero at the edge of the channel, as, for these relatively low energy states, the channel is a good approximation to an infinite well.

Having determined the number of available conduction modes in the two potentials, we can calculate the conductance of the channel in each direction using equation 2.24. The shape of the potential also depends on the magnetisation of the stripe, and so the shape of the magnetoresistance curve can, in principle, be calculated.

Here, a square well model for the channel is used. This is not the only option – parabolic confining potentials are often used to model channels, with the advantage that the resulting eigenfunctions are analytical. However, as this advantage is lost in this case due to the modulation caused by the magnetic field, such a model presents no particular advantage over any other confining potential, and the square well is retained for simplicity.

Splitting and smearing of Landau levels

Each of these transverse modes is in fact a two-fold degenerate state, with spin up and spin down channels. In our experimental configuration, B_{app} is applied in the plane of the 2DEG, and so would lift this degeneracy due to the Zeeman effect. The Zeeman splitting is the resulting energy difference between the two modes and, for electrons, is given by

$$E_z = g^* \mu_B B \tag{4.7}$$

where g^* is the effective g factor of the electrons in the channel.

The g factor for electrons in bulk GaAs is $g^* = -0.44$, but the presence of a confining quantum well can change this value. This is particularly the case for particularly narrow wells[76] in which a significant part of the electron's wavefunction lies within the $Al_{0.3}Ga_{0.7}As$, which as a bulk g^* value of $+0.4$. However, this effect is generally small for wells more than 5nm wide, and for our heterostructures $g^* = -0.44$ is a reasonable approximation.

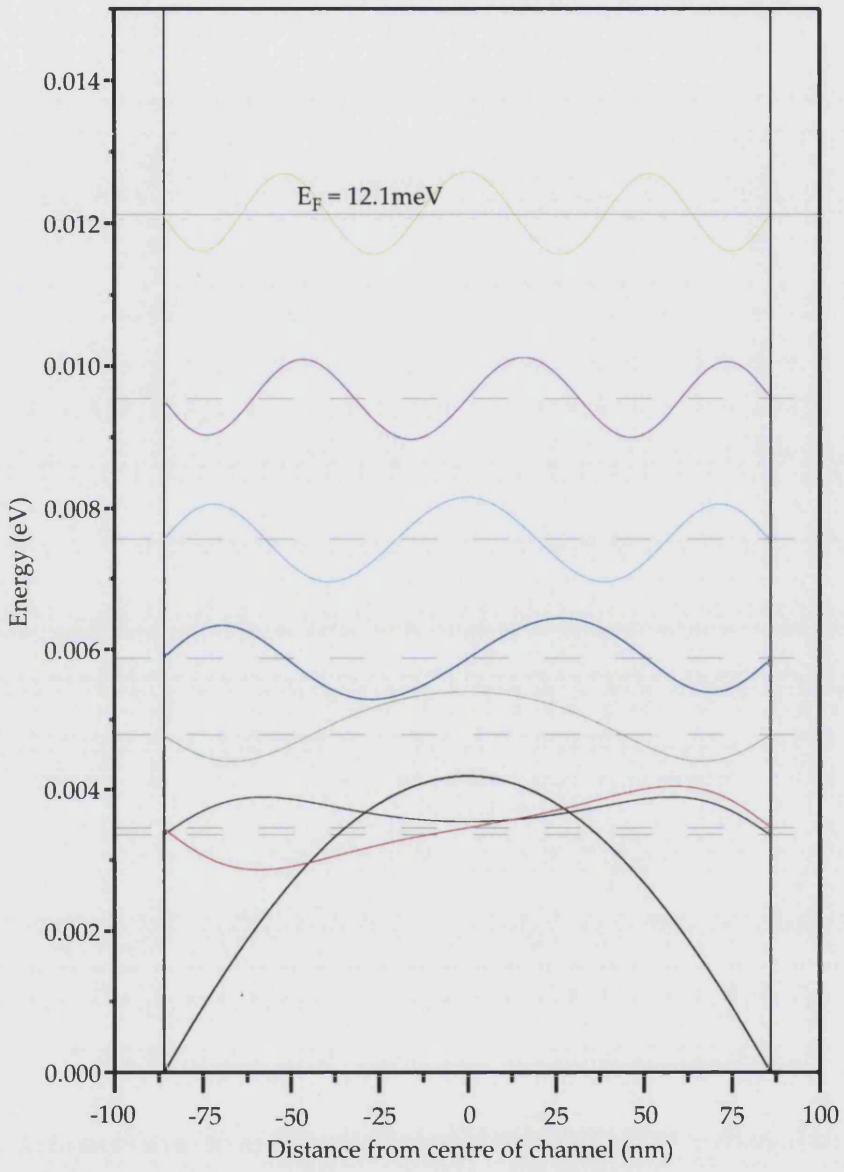

Figure 31. Eigenfunctions below E_F in the potential formed when $B_1 = 5 \times 10^6 Tm^{-1}$. The energies of the modes are marked with dashed lines, and the Fermi energy is shown as a solid line.

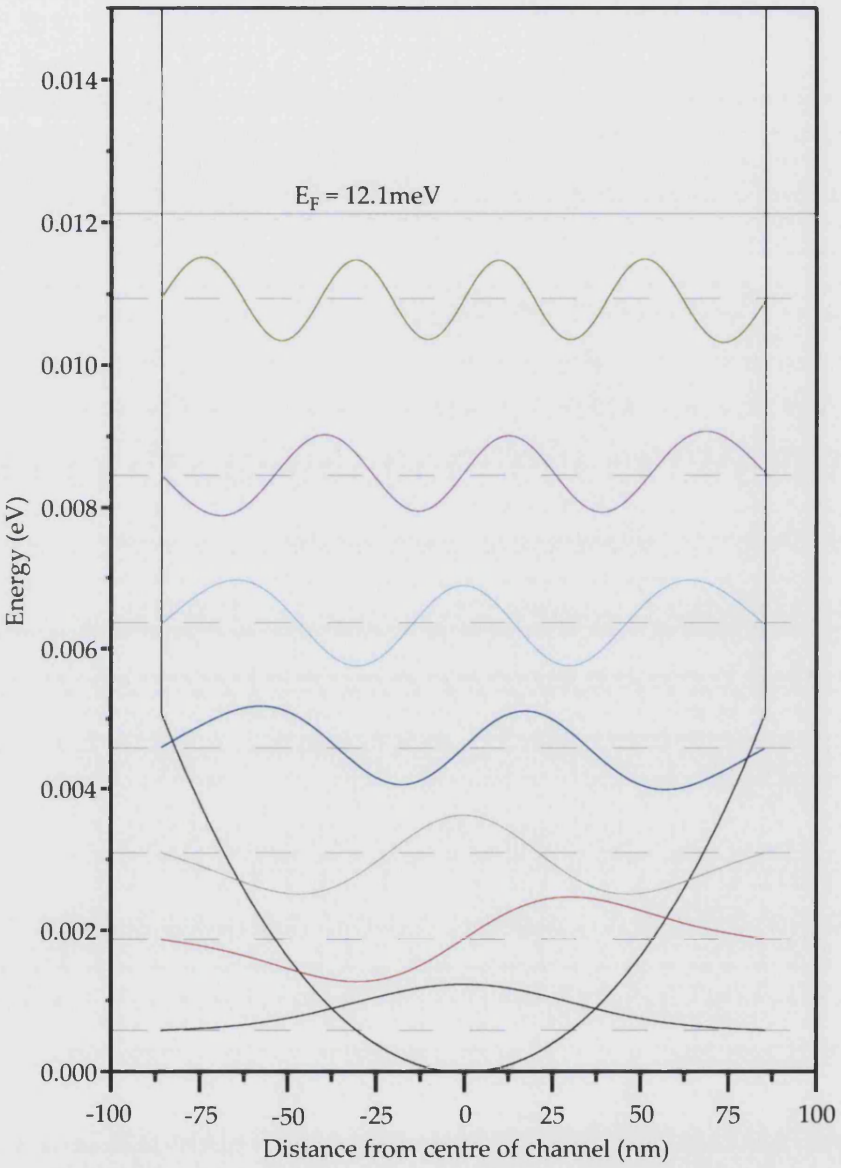

Figure 32. Eigenfunctions below E_F in the potential formed when $B_1 = -5 \times 10^6 \mathrm{Tm}^{-1}$. The energies of the modes are marked with dashed lines, and the Fermi energy is shown as a solid line.

Furthermore, the g value the 2DEG is modified by an field-dependent exchange interaction[33], leading to an *enhanced* g *factor*. It is also anisotropic - the value for magnetic fields applied perpendicular to the current direction has been found to be less than that for fields applied parallel to the current[60].

It is difficult to determine the enhanced g factor in our experiments. However, we can estimate an upper bound for the effect of the Zeeman splitting using a value of $g = 1.5$ which is in approximate agreement with references [60] and [56]. Using this value gives a Zeeman energy of $1.39 \times 10^{-23} \times B$. At the maximum applied field of 12T, the splitting is found to be or $\approx 1.6 \times 10^{-22}$J or $\approx$ 1.0meV.

The energies of the Landau levels are also expected to be affected in our experiments by the application of a significant source-drain bias voltage V_{sd}[61]. The Landau level is ether split[61] if transport in the channel is adiabatic, or smeared out[26] if it is not. This is due to the energy band around the Fermi energy in which transport occurs being broadened.

The size of this effect is given by $E_V = eV_{sd}$. In our experiments, the maximum source-drain voltage applied was 2.5mV. We also assume transport was non-adiabatic, and so the maximum smearing would be 2.5meV.

Typical intermode spacings predicted by the theory described in the previous section are 2meV. This compares to a combined energy of around 3.5meV for the effects described above. They would therefore have the effect of smoothing the plateaux in conductance that would otherwise be expected.

Application of model to results

In the absence of the splitting introduced in by the effects discussed in the previous section, this model suggests that the conduction in the channel should be quantised in units of e^2/h. The situation is analogous to a quantum point contact defined by a split electrostatic gate[90]. In that system, an increase in the negative charge on the gate constricts the channel and removes conducting modes by raising them above the Fermi level. Here, the energy of the modes is increased by the introduction of the magnetic field gradient, and a steeper field gradient raises the mode energies still further.

Therefore, a number of plateau in the magnetoresistance would be seen, with intermediate steps as individual modes cross the Fermi level. This behaviour is not seen here, because the splitting and smearing of the Landau levels is comparable to the intermode spaceing. However, the magnetoresistance measurements can still be usefully compared to the predicted plateaux positions, and

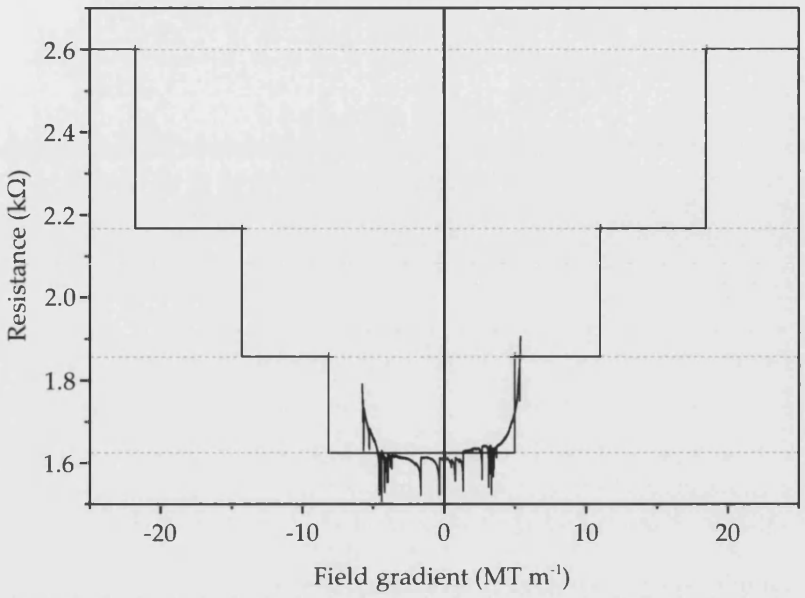

Figure 33. Theoretical and measured magnetoresistance for the 2μm channel length. Modelling assumed an effective wire width of 172nm, calculated from the zero field resistance of the channel.

this comparison is made in figs 33 and 34 for the 2μm and 16μm channel lengths respectively.

In each case, the effective width of the channel potential was determined from the zero field resistance. The model above was used in conjunction with the stripe magentisation curve to calculate the applied fields at which the degenerate conducting modes would be raised above the Fermi energy. The shape of the measured magnetoresistance curve broadly follows the predicted magnetoresistance for both the 2μm channel length and the 16μm channel length.

Another potential source of the blurring is thermal broadening of the Fermi surface. At finite temperatures, the Fermi surface broadens, until it occupies a range of energies about $k_B T$ around the Fermi energy (see section 2.1.2). This leads to the additional conductance due to a conducting mode being introduced gradually as it crosses a Fermi surface of finite depth.

The electrons at the Fermi surface are distributed in a range of approximate order $k_B T$ around the Fermi energy. At a temperature of 0.3K, the Fermi surface therefore has a width of around

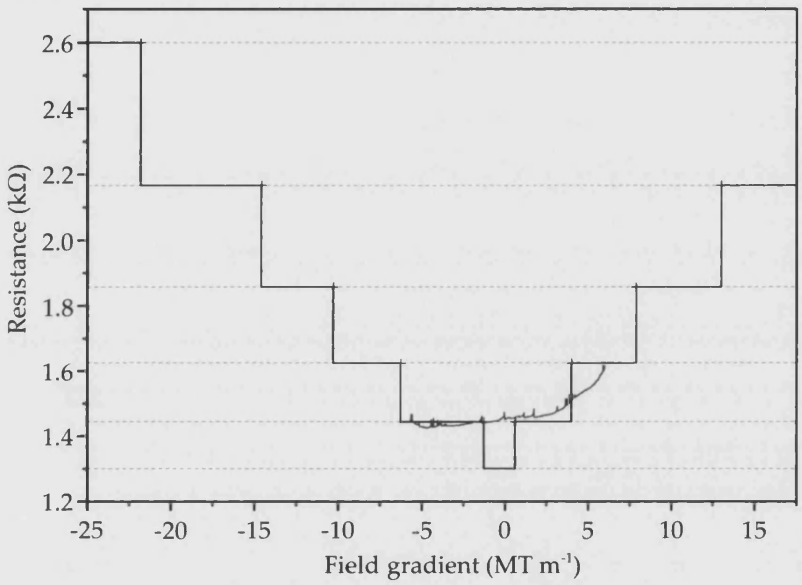

Figure 34. Theoretical and measured magnetoresistance for the 16μm channel length. Modelling assumed an effective wire width of 192nm, calculated from the zero field resistance of the channel.

$0.01 - 0.1$meV. The highest modes in the channel are typically separated by around 2meV. This is significantly larger than the broadening of the Fermi surface, suggesting that thermal effects are not significant at these temperatures. $k_B T$ becomes comparable to the mode separation at around 20K.

Fluctuations in the channel width and the depth and width of the ferromagnetic stripe result in changes in the mode energies along the measured wire length. This would also produce deviation from the expected behaviour.

An insight into the size of this effect can be gained by comparing the zero-field. resistance of the 2μm and 16μm channels. They are 1.6kΩ and 1.4kΩ respectively. This corresponds to 8 conduction modes for the 2μm length and 9.2 for the 16μm long channel.

This suggests that the channel width varies along the wire sufficiently to change the number of transverse modes by at least one. This corresponds to a change in width of around 20nm. This is around the resolution limit of e.b.l., and so we could expect the channel width to vary by around this amount. As a result, the broadening of the Fermi surface over the channel length would be of a similar order to the intermode separation.

The properties of the IV curves shown in figure 23 are also explained well by the above model. IV measurements for $\mu_0 H = \pm 12$T and 0T are plotted. At both positive and negative currents the zero field magnetoresistance has the lowest value. Reversing the current direction swaps the ordering of the positive and negative field resistances. This supports the prediction of the model that reversing the applied field direction is equivalent to reversing the direction of the current.

The sample also exhibits some inherent rectification. The resistances are around 25% larger for positive currents than negative currents. This is probably due to asymmetries in the channel, perhaps caused by an asymmetric etch during the RIE process.

4.5.3 *Analysis of perpendicular magnetisation results*

The results for the applied field perpendicular to the sample show a variety of rich structures, particularly so for the magnetoresistance curve. In fig. 35 part of fig. 26 is reproduced, for field values from 0T to 12T and voltage contacts 14 and 18.

In this plot, conventional Shubnikov-de Haas oscillations are visible at low ($B < 2$T) fields. At higher fields the situation is less clear. However, we tentatively ascribe the higher field behaviour to the anomolous Shubnikov-de Haas effect[91]. This effect is observed in magnetoresistance measurements involving one or

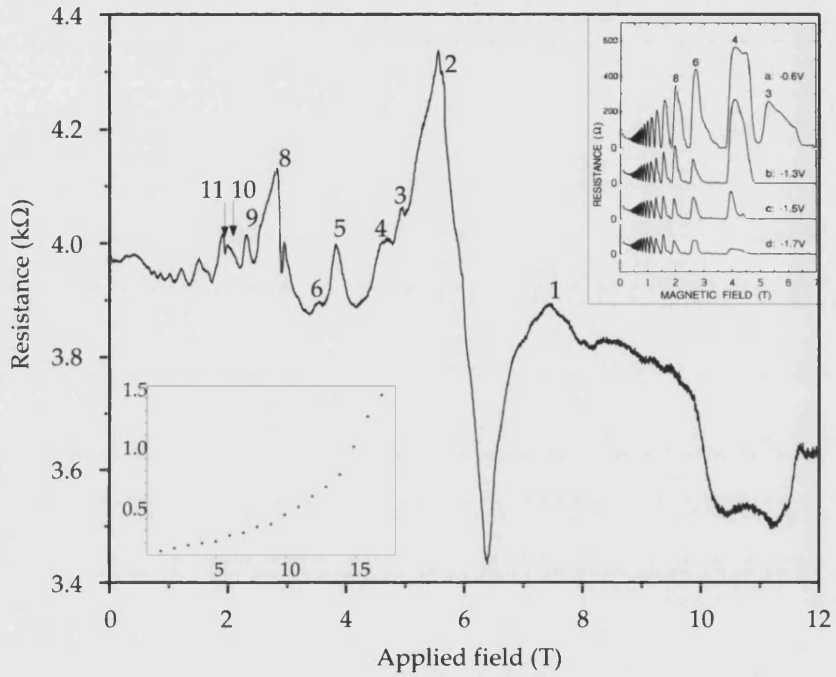

Figure 35. Reproduction of part of fig. 26, for field values from 0T to 12T and voltage contacts 14 and 18. Magnetoresistance oscillations are visible. The splitting of one Shubnikov-de Haas oscillation peak is arrowed. Inset top right is a plot of magnetoresistance of a wide 2DEG channel probed by a point contact, taken from reference [91]. Inset bottom left is a plot of $1/B$ against peak number. Peaks up to 10 are labelled in the main plot. Deviation from linear behaviour due to peak splitting is clear.

more point contacts. In this case, the channel being probed was sufficiently narrow to provide this condition.

For comparative purposes, a plot from van Wees *et al*[91] is included as an inset in fig. 35. There are some qualitative similarities between the two, particularly at low (B < 2T) and high (B > 5T) fields. Our device differs from the situation presented in reference [91] due to the modulation of the uniform applied field by the stripe. There will therefore be a range of field values in the channel, and so there will not be a single predicted 1/B frequency for the Shubnikov-de Haas oscillations. We see some evidence of splitting of magnetoresistance peaks, suggesting different values of B for different edge channels (arrowed in fig. 35).

This structure is present but less clear in fig. 25, because of a background superimposed upon the oscillations.

We can take the difference between the voltage measured for the two channels. These are plotted in figs 36 and 37. Fig. 36 shows the difference during the magnetoresistance measurements, and fig. 37 shows the same for the the IV curves.

Magnetoresistance

The differential magnetoresistance (fig. 36) shows a linear background, on which is superimposed oscilations periodic in 1/H (which are particularly clear in the plot for $I = -2.5\mu A$). As the maximum stray field from the dysprosium stripe was around 0.8T, the applied field, the maximum value of which was $\mu_0 H = 12T$, dominates. The contribution from the stray field is therefore mostly disregarded in this analysis, although it may well have a bearing on the full complexity of fig. 25 and 26.

The conductance is asymmetric at the edges of the channel due to the presence of circulating magnetic edge states. Conductance is enhanced if the current-carrying electrons flow in the same direction as these states, and is decreased if the two directions of travel are opposed.

This difference will be quenched if states at opposite edges of the channel are allowed to mix. This occurs more at low fields, as edge states are not so tightly confined to the boundaries of the 2DEG. Mixing therefore occurs in the middle of the channel. This accounts for the linear response to the applied field.

States can also mix through the Landau levels formed in the bulk region of the 2DEG. When a Landau level crosses the Fermi level coupling between the edge states is increased. The periodicity of the oscillations in the magnetoresistance difference is controlled by the electron sheet density, in analogy with Shubnikov-de Haas oscillations. The matching of the Fermi level and Landau levels is marked by minima in the absolute voltage difference.

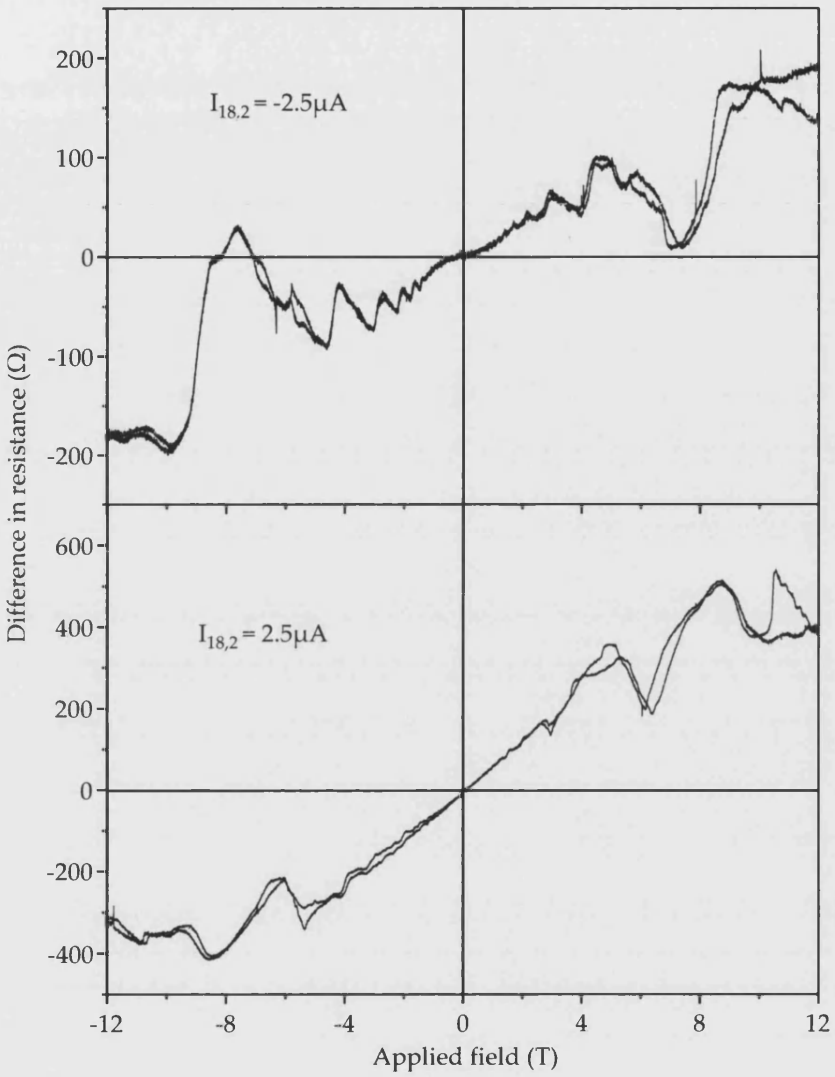

Figure 36. Difference between the magnetoresistance of the two conducting channels. The current was passed from contact 2 to contact 18 in the top plot, and from contact 18 to contact 2 in the bottom plot. Resistance values for a sweep up and a sweep down are plotted, showin very little difference.

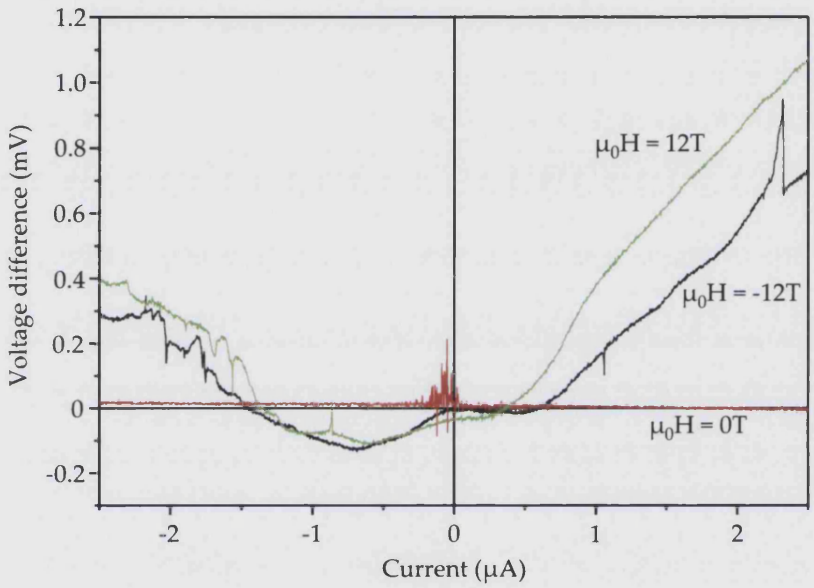

Figure 37. Difference between the IV curves of the two conducting channels. Data for three different values of applied field are plotted. Current was passed from contact 18 to contact 2, and the values for $\mu_0 H = 12T$ inverted for ease of comparison.

By using equation 4.1, these minima give an electron density of $n_s = 4.0 \pm 0.6 \times 10^{11} cm^{-2}$, which agrees with the electron density calculated in section 4.5.1. The greater uncertainty (and slightly higher value) is probably due to the modulation of the magnetic field in the bulk by the ferromagnetic stripe.

This supports the view that the oscillatory component of the magnetoresistance difference is due to mixing of the edge channels *via* bulk Landau states. The oscillation cannot be coming from variations in the conductance of the edge channels, as such variations would be equal in each channel, and so be cancelled out by the subtraction of the two resistances.

IV curves

The difference between the IV curves (fig. 37) is broadly as expected. Particularly at positive currents, the voltage difference is approximately proportional to the applied current, suggesting quasi-Ohmic behaviour in both current channels. The difference is of the same sign at both negative and positive currents, despite the *absolute* current changing sign.

At negative currents, behaviour is reasonably as expected, except for the region between $I = 0\mu A$ and $I = -1.5\mu A$. Here the voltage difference is negative. This may be because, for negative currents, electrons were inserted on one side of the channel, through contact 18, favouring injection into the set of edge states on that side.

The $B = 0$ curve shows no difference between the voltage probes on opposite edges, and so confirms that the difference is due to magnetic effects in the channel.

4.6 CONCLUSION

In conclusion, asymmetric magnetoresistance in a channel subject to a high magnetic field gradient has been observed, which has been ascribed to the different magnetic potentials seen by the electrons travelling each way in the stripe. However, the device used here is not really capable of fully testing this theory, as it is incapable of producing high enough field gradients. This is explored further in Chapter 7.

The conductance enhancement at the edges of the channel due to magnetic edge states has been probed. In this configuration, the contribution to the field due to the stripe was much smaller (an order of magnitude) than the applied field. It can therefore be ignored.

Coupling between the edge states is decreased as the applied field increases, and the edge states are confined more tightly to

the edges of the channels. Edge states can also couple through bulk Landau states, and this is enhanced when Landau states cross the Fermi level.

Sample shape may be of considerable importance in this effect. Contact 18 in our sample was on one side of the channel, and so would have preferentially injected electrons into edge states on that side.

5

DETECTION OF INDIVIDUAL SNAKE STATES

To better probe the magnetic edge states beneath a perpendicularly polarised ferromagnetic stripe, *snake state spectrometers* were designed, fabricated and tested. By discretising the snake orbits in the channel and directing these through a point contact, individual snake states were observed.

This type of device can be described as a ballistic electron optic device. Manipulation of electrons in the solid state can be performed by using electrostatic and magnetostatic fields. These methods have been realised in a number of ways, including electrostatic lenses[77] and prisms[78].

5.1 DEVICE DESIGN

The device (see fig. 38) is comprised of a 2DEG channel, on top of which is deposited a ferromagnetic stripe. In-plane magnetisation of this results in the field profile described above. Point contacts (PC1, PC2) are then defined at each end of the stripe, placing boundary conditions on the edge states permitted beneath the stripe. A further point contact (PC3) is then defined beyond the end of the stripe.

Electrons traversing the stripe region therefore have a limited number of snake states available to occupy – the orbits must cross the zero field line at the point contacts. The electron must therefore undergo a half-integer (n) number of transverse oscillations in this region. As there is a link between the wavelength of oscillation, the cyclotron radius beneath the stripe and the angle, θ_n at which electrons cross the zero field line in the channel, this geometrical constraint discretises the angles available to the edge states. Only when θ_n for a given edge state corresponds to the angle between the stripe axis and the path from PC2 to PC3 will the state contribute to the conductance between regions 1 and 4.

By changing the magnetisation of the stripe, the cyclotron radius in region 2 can be changed. Therefore, all θ_n are changed as well. Sweeping the applied in-plane field results in the crossing angle varying from $\theta_n = 0$ to $\theta_n = \pi$. Maxima in device conductance will be observed at applied fields such that the above condition is met. At these fields, the non-local resistance between regions 3 and 4 will be at a minimum.

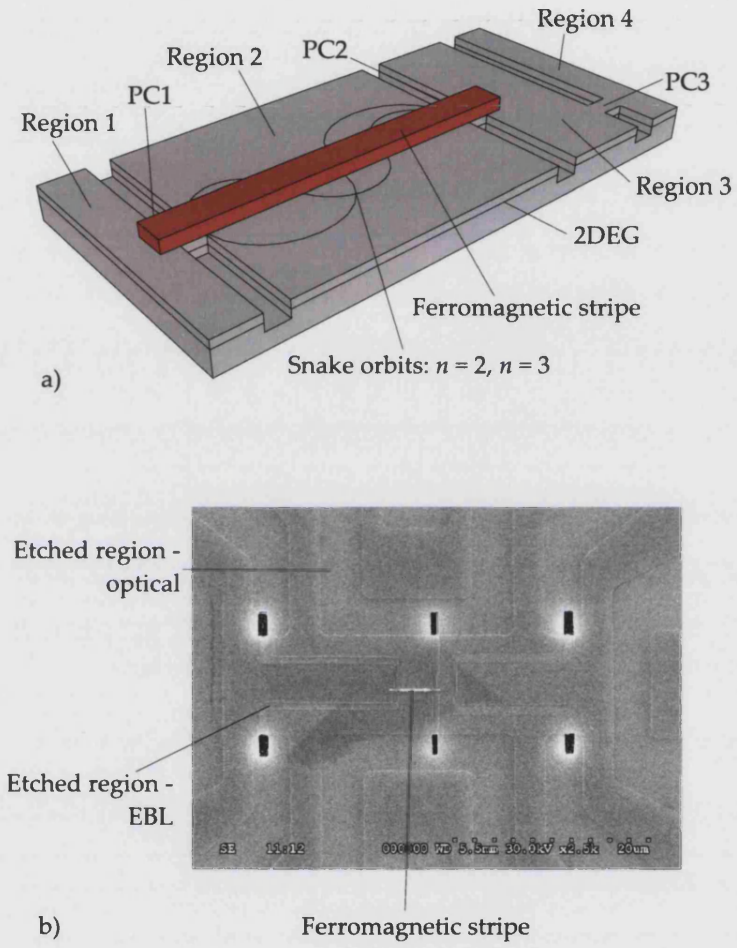

Figure 38. a) Schematic perspective view of the spectrometer, showing PCs 1-3 and regions 1-4. b) Scanning electron micrograph of the device.

5.2 DEVICES

Devices were fabricated using the techniques described in chapter 3. The substrate was a near surface heterostructure, with the 2DEG 30nm below the surface. A 10μm wide channel was defined using optical lithography and wet-etched. The dysprosium wire, which was 150nm wide, 150nm deep and 5μm long, was defined on top of the channel by electron-beam lithography (e.b.l.) and thermally evaporated. 0.5μm wide channels at each end of the wire were then defined by e.b.l. and reactive ion shallow-etched, with the dysprosium acting as a component of the mask to preserve the 2DEG in self-aligned point contacts beneath the wire. In the same step, the final point contact (PC 3) was defined and etched. The width of the PCs at each end of the stripe was therefore defined by the stripe itself as being 150nm wide. PC 3 was of similar width.

5.3 EXPERIMENTS

The device was mounted on a rotation stage and then cooled to around 0.3K using a pumped He^3 cryostat. This low temperature ensured that the mean free path of the electrons was at least as long as the device. Therefore electrons would remain in one snake orbit underneath the stripe, rather than being scattered from one state to another.

It was then illuminated with a red LED in order to photoexcite electrons from the DX centres and saturate the 2DEG (see Chapter 2). A magnetic field was applied to the device using a superconducting magnet. The stripe was therefore magnetised as described in section 3.3.2 above.

A variety of magnetoresistance measurements, both local and nonlocal, were made.

To determine the wavevector of the Fermi surface, the magentic field was first applied normal to the plane of the 2DEG. A current of 2μA was passed between contacts 1 and 4 (see fig. 39 for contact labelling). Magnetoresistance measurements in this configuration display Shubnikov-de Haas oscillations. Using equation 2.32 the period of these oscillations can be linked to the electron density in the 2DEG, and so to the Fermi energy and wavevector. These parameters of the 2DEG were necessary for the theoretical analysis of the results, as set out in section 5.5.2.

For subsequent measurements the device was rotated so that the applied field was in the plane of the 2DEG. A current of 1μA was passed from contact 1 to contact 4, and the applied field swept between +3T and -3T. Measurements were made of the

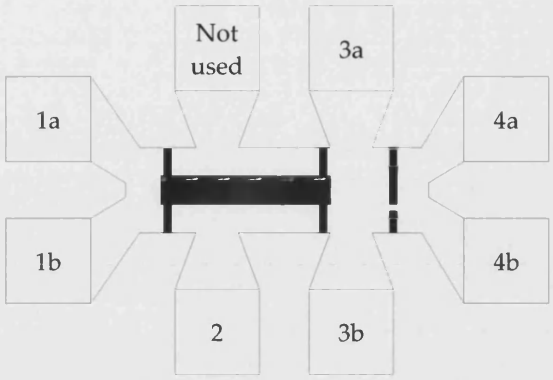

Figure 39. Contact labelling for the spectrometer.

magnetoresistance across each point contact and across PC1 and PC2 together.

Non-local measurements were also made. The applied field was swept between +3T and -3T. A 1μA current was passed between contacts 1 and 2, and the potential across contacts 3 and 4 (across PC 3) measured using standard lock-in techniques. This was therefore a non-local measurement and better suited to show the effects of ballistic phenomena on the magnetoresistance. Furthermore, the measurements were free from heating in PC 3.

5.4 RESULTS

Results are plotted in figs 40 to 45. Fig. 40 shows a.c. magnetoresistance measurements for the entire device, with a perpendicular applied field. Shubnikov-de Haas oscillations are clear, and are used to calculate the electron density and Fermi energy in the next section (which contains a more detailed analysis of all of these results).

Figs 41 to 44 show magnetoresistance data for the point contacts in the device. In figs 41 to 43, a pair of peaks centred on $B = 0$ can be seen. Applied field magnitudes at which the maxima occur are in the range 50mT - 65mT. They are due to classical size effects, and are used to characterise the width of the contacts in the next section. Shubnikov-de Haas oscillations are visible at fields above around 1T.

These peaks are not see in fig. 44.

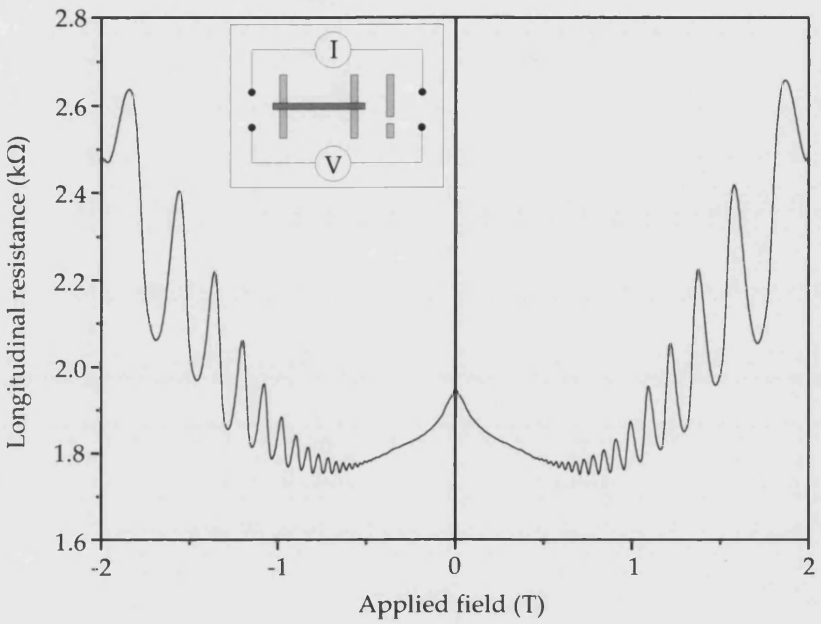

Figure 40. Magnetoresistance measurement of the entire spectrometer, with the field applied perpendicular to the 2DEG. The current was between contacts 1a and 4a, and the voltage was measured between contacts 1b and 4b. Shubnikov-de Haas oscillations can be seen.

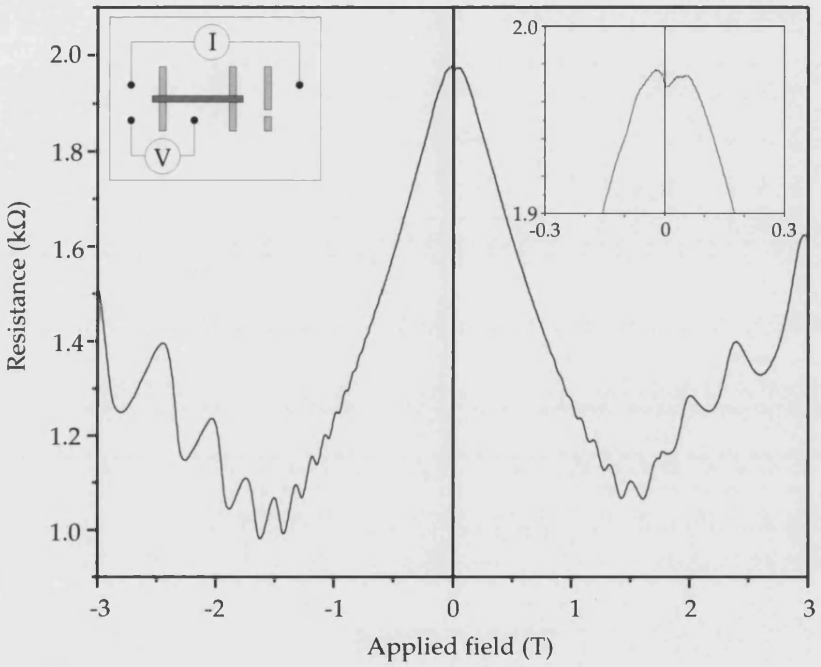

Figure 41. Four point magnetoresistance measurement across PC 1. Magnification of the region around zero field is inset top right. A schematic diagram of the contact configuration is shown top left. Current was applied between contacts 1a and 4a, and the voltage measured between contacts 1b and 2. I = 1μA, T = 0.3K, field normal to the 2DEG.

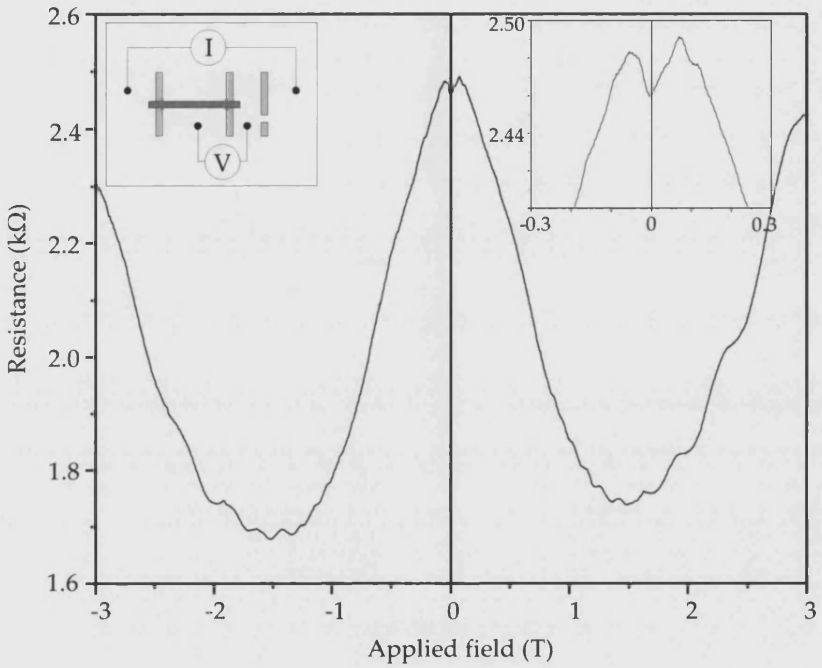

Figure 42. Four point magnetoresistance measurement across PC 2. Magnification of the region around zero field is inset top right. A schematic diagram of the contact configuration is shown top left. Current was applied between contacts 1a and 4a, and the voltage measured between contacts 2 and 3b. I = 1μA, T = 0.3K, field normal to the 2DEG.

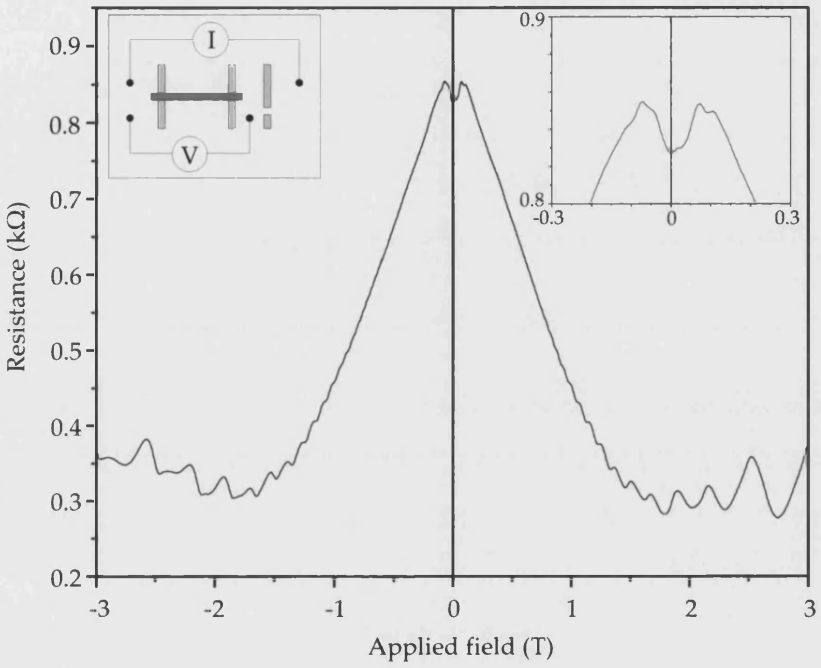

Figure 43. Four point magnetoresistance measurement across PCs 1 and 2. Magnification of the region around zero field is inset top right. A schematic diagram of the contact configuration is shown top left. Current was applied between contacts 1a and 4a, and the voltage measured between contacts 1b and 3b. I = 1μA, T = 0.3K, field normal to the 2DEG.

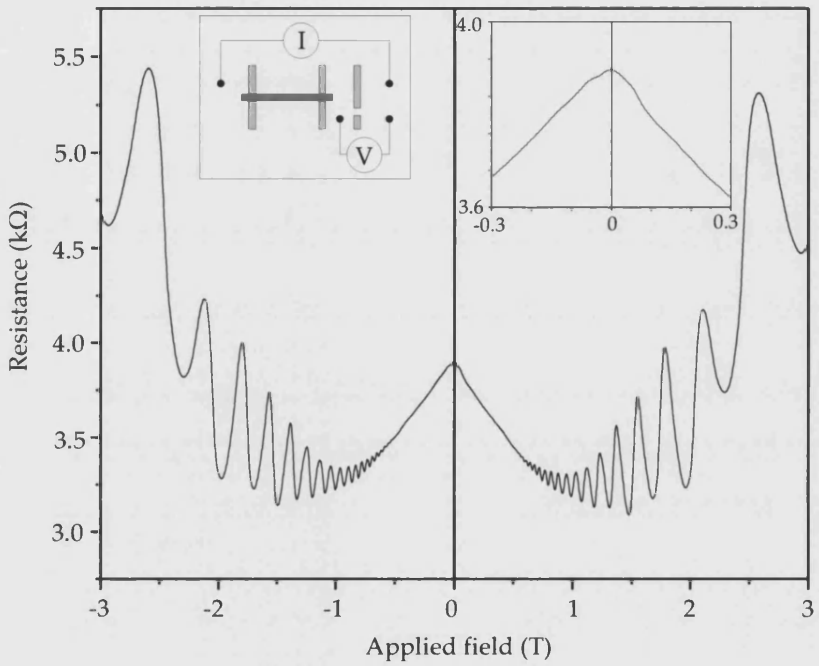

Figure 44. Four point magnetoresistance measurement across PC 3. Magnification of the region around zero field is inset top right. A schematic diagram of the contact configuration is shown top left. Current was applied between contacts 1a and 4a, and the voltage measured between contacts 3b and 4b. I = 1μA, T = 0.3K, field normal to the 2DEG.

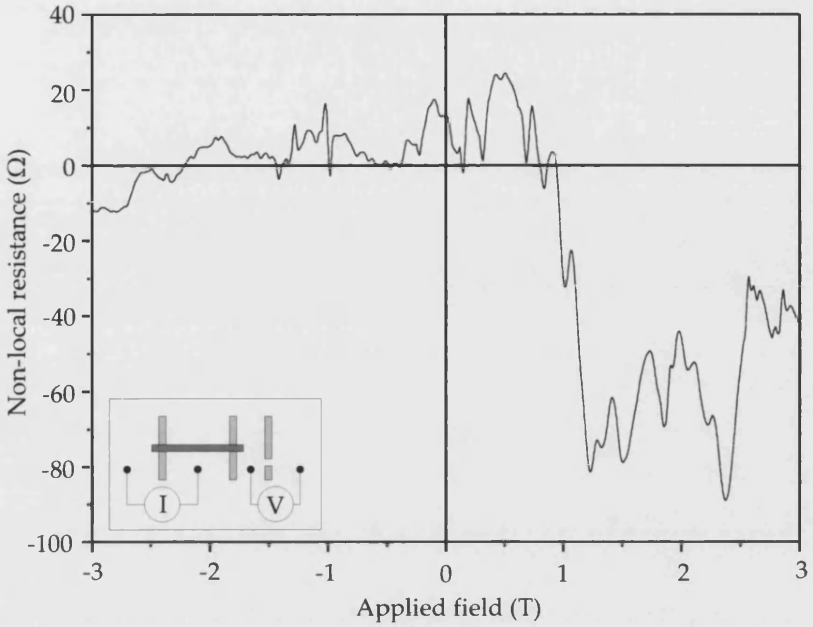

Figure 45. Non-local magnetoresistance measurements across PC 3. A schematic diagram of the contact configuration is shown bottom left. Current was passed from contact 1b to contact 2, and voltage probed between contacts 3b and 4b. Data is smoothed by moving average. I = 1μA, T = 0.3K, field parallel to the 2DEG.

Fig. 45 show non-local magnetoresistance measurements for the device operating in the configuration, described above, to detect discrete snake orbits. A non-local resistance of around R = 0 is measured for negative applied fields, and a negative and oscillating resistance for positive applied fields.

5.5 ANALYSIS

5.5.1 *Device characterisation*

The frequency of the Shubnikov-de Haas oscillations are shown in fig. 40. They are used here to calculate the electron density for the 2DEG as in section 4.5.1 in the preceeding chapter. Fig. 46 shows a plot of 1/B for successive resistance minima. The gradient is $0.091T^{-1}$, corresponding to a sheet electron density of $n_s = 5.84 \times 10^{11}cm^{-2}$ and a Fermi energy of $E_F = 3.32 \times 10^{-21}J = 20.8meV$.

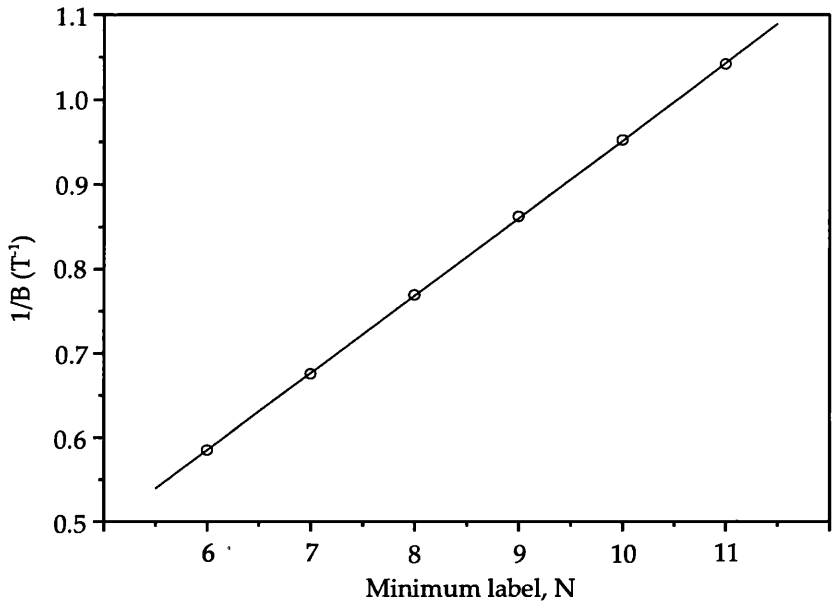

Figure 46. Shubnikov-de Haas minima for the spectrometer plotted against 1/B. The x-axis is the index N in equation 2.32.

Some magnetoresistance measurements on PCs 1-3 (figs 41 to 44) show symmetric peaks around $B = 0$ characteristic of point contacts[84]. Resistance maxima are at ± 50mT for PC 1 and ± 65mT for PC 2. Peaks are not present in the data for PC3.

The width of the point contacts can be determined from the field at which the maxima occur[84]. At this value of applied field, the cyclotron radius of the electron is the width of the point contact. This is the condition at which maximum backscattering occurs, and so conductance is at a minimum. The width is given by

$$w = \frac{l_c}{2} = \frac{\hbar k_F}{2eB}. \tag{5.1}$$

We cannot ignore the additional contribution to the field at the 2DEG from the magnetisation of the stripe. This can be calculated from the magnetisation curve in fig. 15 and the step approximation to the field profile at the 2DEG shown in fig. 17. We find the contributions to be of roughly the same size as the applied field, and so the width of PC 1 is 662 ± 130nm and the width of PC 2 is 546 ± 120nm. The large error is due to uncertainty in the magnetisation of the stripe at these fields.

Magnetoresistance measurements for PCs 1 and 2 together (fig. 43) show more complicated structure, consisting of two superimposed pairs of peaks. Each point contact contributes a separate pair of maxima. PC 3, on the other hand, does not demonstrate these maxima. This is perhaps because of the different method of fabrication. While PC 1 and 2, which were protected from the etch by the ferromagnetic stripe, should be reasonably square-cut, PC 3 is much more rounded, and this may serve to damp the magnetoresistance peaks. Furthermore, because the contact was etched, it is likely that there would be a strong non-specular component to the boundary scattering.

5.5.2 *Snake state detection*

Theoretical modelling

We can model this device using a semiclassical approach. The geometry is shown in figure 47. The electron travels in the positive x direction. The y co-ordinate describes the displacement across the channel, with $y = 0$ being the centre line, at which the actual field component B_z is zero. The electron crosses the line $y = 0$ at an angle θ. The point contact acting as a detector, PC3, is displaced from PC2 by a distance d in the x direction and $-a$ in the y direction.

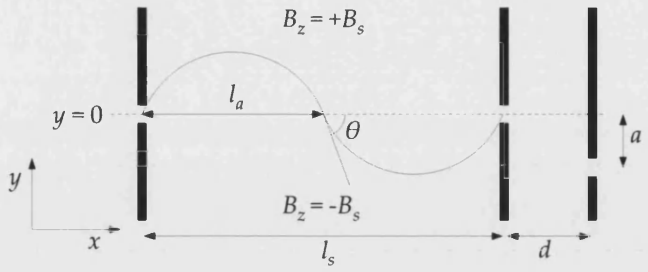

Figure 47. The geometry used to model the devices. The electron orbit shown is the $n = 2$ trajectory.

We use the step approximation for the field profile. The field is therefore given by $B_z = -B_s$ for $y < 0$ and $B_z = +B_s$ for $y > 0$. This region is of length l_s. Under the stripe an electron travels in a circular arc, with radius equal to the cyclotron radius, $R_c = \hbar k_F / eB_z$, due to the Lorentz force. It will describe a number of arcs, based on the $y = 0$ line.

The length of the base, l_a, is determined by θ and R_c, and is given by

$$l_a = 2R_c \sin\theta. \tag{5.2}$$

For a positive field direction snake orbits centred on the zero-field line are formed. Electron orbits can only contribute to the conductivity of the device if they have an integer number of half-wavelengths under the stripe and θ is such that they coincide with PC3. The half-wavelength and θ of a given state are linked by the cyclotron radius, which is governed by the magnitude of B_s.

Using this link between the applied field and the cyclotron radius, and the geometrical constraints imposed by the device, we can determine the values of B_s at which resistance minima should be present. A full derivation is presented in Appendix B. The change in field between successive minima is given by

$$\Delta B_s = \frac{2\hbar k_F}{le\sqrt{1 + \frac{a^2}{d^2}}}, \tag{5.3}$$

where $a/d = \tan(\theta)$. The Hall curve from the stripe is then used to link B_s to the applied field, H.

This model only applies if the applied field is in the positive direction (i.e. the direction that results in a field gradient such that electrons travelling from PC1 to PC3 occupy snake orbits). If the applied field direction is reversed, the device will not work, as electrons are not channelled along the zero field line. Therefore oscillations are not visible and the non-local voltage is predicted to be around zero.

Fit of model to results

For the device described above, the distance from the end of the stripe to PC3, d, is 2μm, and the offset of PC 3, a, is 200nm. The length of the stripe between PC1 and PC2, l is 4μm. The Fermi wavevector is given by $k_F = \sqrt{2\pi n}$, with $n = 6 \times 10^{11} cm^{-2}$.

Equation 5.3 gives a value for ΔB_s of 0.06T. In fig 48 replotted magnetoresistance data are shown, with these predicted applied field values for resistance minima highlighted by the dotted vertical lines.

The predicted resistance minima *broadly* coincide with the actual field values at which minima are found. Significant oscillations in the magnetoresistance are apparent at positive values of the applied field. At negative fields, no such periodic oscillations are seen. With the stripe magnetised in this direction, the device would have been working "in reverse". In other words, the Lorentz force beneath the stripe pushes electrons towards the edges of the channel, and does not guide them in snake orbits. The non-local voltage is zero.

The resistance at negative fields does give us an idea of the magnitude of any oscillations *not* due to the channeling of snake states. Typically, the magnetoresistance in this regime fluctuates aperiodically with a maximum change of 10Ω. Periodic oscillations in the positive field regime have a magnitude of between 20Ω and 40Ω. This helps to confirm that these features are not noise.

There are a number of simplifications in our model that could lead to prediction of the incorrect period for the magnetoresistance oscillations. We have assumed that the ferromagnetic stripe lies entirely between PC 1 and PC 2. In fact, this is not the case – a protrusion of around 400nm either side of the PCs is just visible in fig. 38b. (This is due to the difficulty of aligning the stripe with the dry etch during the e.b.l. process.)

Another source of inaccuracy associated with the end of the stripe is the assumption that the magnetic field profile described above gives way abruptly to the zero field region. In fact, there would be a intermediate transition region.

Finally, the finite length of the point contacts is not taken into

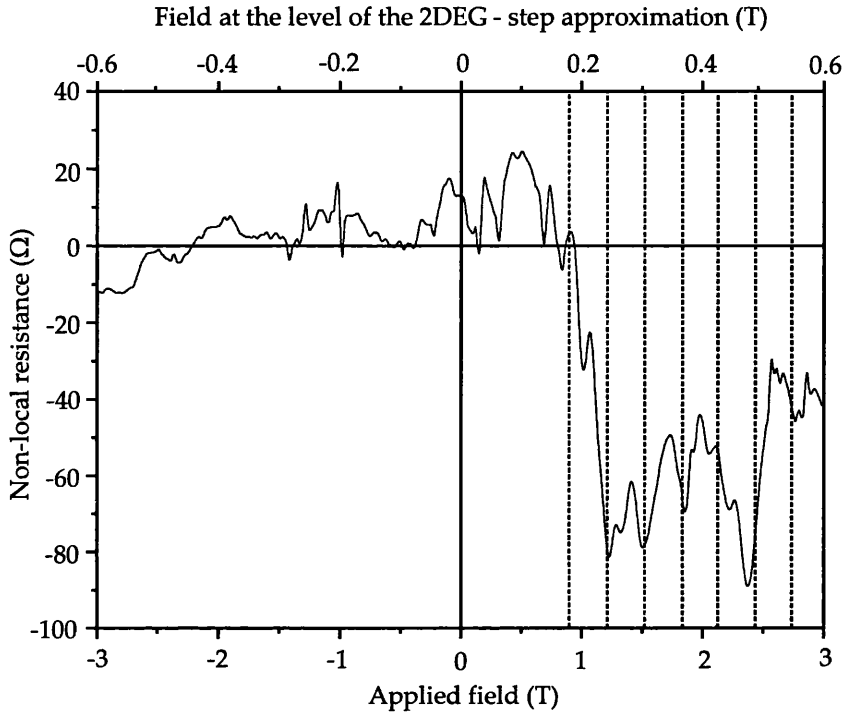

Figure 48. Non-local magnetoresistance measurements across PC 3 – fig. 45 replotted. The applied field is plotted along the bottom x-axis, and the top x-axis is labelled with the resultant value for B_z at the level of the 2DEG in the stepped field approximation (see section 3.3.2). Note the non-linearity of the relationship between these two. Dotted vertical lines are predictions of magnetoresistance minima from equation 5.3.

account. This may have an effect on oscillations if the quarter-wavelength of the snake orbit is comparable to the length ($\approx$ 300nm) of the PCs. In these devices this would be the case if the number of half-wavelengths between PC 1 and PC 2 were 8 or more. According to the predictions of equation 5.3, the fields at which this would occur are outside the regime studied here.

5.6 CONCLUSION

In conclusion, a device has been demonstrated in which snake orbits in a channel are discretised by the boundary conditions imposed by two point contacts. They are then selectively detected by a third point contact offset from the axis of the device. The non-local magnetoresistance of the third point contact was best at showing the spectral content of the snake orbits, as transmission in this mode of operation was entirely ballistic.

6

RESISTIVELY DETECTED FERROMAGNETIC RESONANCE

In this chapter, the interaction of snake orbits with the electromagnetic field is discussed. Experiments were performed in which a semiconductor/ferromagnet wire was irradiated with microwaves, and ferromagnetic resonance in the wire was detected *via* resistance changes in the 2DEG channel.

6.1 INTRODUCTION

There has been considerable interest in the fundamental physics of microwave emission from a variety of spin oscillator systems. A nanoscale microwave sourse that can be integrated with semiconductor electronics would also have applications in the fabrication of small scale wireless interconnects between microelectronic components[12]. This is a possible approach for circumventing the problems caused by the scaling of conventional interconnects in ultra-large scale integrated (USLI) circuits.

A number of nanoscale systems capable of microwave emission have been described.

The magnetisation of a thin ferromagnetic film can be reversed by a spin polarised current[36] with only moderate applied magnetic fields. Such behaviour is found in spin valves, which consist of a fixed magnetic layer, which acts to polarise the applied current, and a free layer. This magnetisation switch is followed by a period of damped spin precession, which is accompanied by the emission of a pulse of microwave frequency radiation[67].

Powers of a few nanoWatts have been observed from such structures[66]. The peak emission frequency is tunable in the interval $1 - 50$GHz by varying the magnitude of the spin polarised current through the device.

Microwave emission from molecular magnets has also been detected[34]. In these systems, reversal of the magnetisation is usually dominated by tunneling between Zeeman energies. When the applied magnetic field is reversed, the energies of these states are swapped. If the field switch is slow, then coupling between the levels restores the equilibrium electron distribution.

If, on the other hand, the field is switched rapidly, equilibrium is not maintained during the process and a population inversion results. A single burst of photons, with wavelength corresponding

to the Zeeman energy, is released as the electrons relax to the lower energy level. Microwave powers of a few tens of femtoWatts have been observed during coherent emission from crystals of magnetic molecules[82].

Here, a theory[57] we have developed describing the interaction of snake orbits with the electromagnetic field is described. Emission of microwaves is predicted, which would be tunable with maximum peak frequency of around 500GHz. Emission is expected to be continuous, with power levels of around 1nW.

This theory motivated experiments involving irradiation of a GaAs/AlGaAs heterostructure modulated by a Dy wire with microwaves in the range $50 - 110$GHz.

6.2 THEORY OF RESONANT EMISSION

The results described in this chapter concern spin resonance effects in the ferromagnetic structure. However, the theory of fluorescence from magnetic edge states we have recently developed is first presented, to enlarge upon the motivation for these experiments. A more in depth discussion of the forces on an electron in the channel is required. This leads on to a description of the resultant spin dynamics.

6.2.1 *Theoretical development*

The system

A 2DEG channel is considered in which an electron is propogating in the $\pm x$ direction. The y direction is taken as being across the channel, with the $y = 0$ point in the centre, and the z axis is normal to the plain of the 2DEG. The component of the magnetic field parallel to the z axis is then B_z.

We recall that the perpendicular component of the magnetic field beneath a transversely magnetised stripe can be reasonably approximated by a linear magnetic field gradient (section 3.3.2). This is written as

$$B_z = B_1 y. \tag{6.1}$$

In this development, the y component of the magnetic field must be taken into account. This is denoted B_y.

Classical electron dynamics

The motion of the electrons in the channel is now discussed.

The electron is subject to the Lorentz force due to B_z. It therefore undergoes transverse oscillations in a magnetic potential. It can be shown that the maximum amplitude of these oscillations is comparable to the width of the magnetic wire, and is given by $l_b = s\sqrt{\hbar k_F/eB'}$. The electron therefore remains in the region where equation 6.1 remains a good approximation.

It is worth considering the effect of the force due to the Zeeman effect on the magnetic dipole moment. This is due to the gradient of B_z acting on the spin of the electron. The spin precesses around B_y with the Larmor frequency, and so the Zeeman force also oscillates at the Larmor frequency.

As the magnitude of the Zeeman force depends on B_1 and the Lorentz force depends on B_z, the Zeeman force will dominate when y is sufficiently small, as B_1 is constant across the channel and B_z is at a minimum in the centre. Zeeman effects therefore control motion at the centre of the channel. The region in which the Zeeman force is of greater magnitude than the Lorentz force has a half-width of

$$l_{Zeeman} = \frac{g^* m^*}{g_0 m_0} \frac{1}{k_F}. \tag{6.2}$$

g^* and m^* are the Landé factor and effective mass for an electron in the 2DEG, and g_0 and m_0 are the corresponding values in free space. l_{Zeeman} is typically of the order of 1nm. Since the maximum amplitude of the electron oscillations is typically ~ 200nm, only the action of the Lorentz force is considered.

Therefore, using a semi-classical description of the electron's dynamic, the equations of motion

$$\tau_b \dot{X} = \frac{\cos(\theta)}{2} - Y^2 \tag{6.3}$$

$$(\tau_b \dot{Y})^2 = \left[\cos^2\left(\frac{\theta}{2}\right) - Y^2\right]\left[Y^2 + \sin^2\left(\frac{\theta}{2}\right)\right] \tag{6.4}$$

are obtained. These equations describe an anharmonic oscillator parameterised by θ.

In these equations, the length scales $X = x/l_b$ and $Y = y/l_b$ are introduced. Similarly, $\tau_b = m^*/\sqrt{\hbar k_F e B_1}$. θ parameterises the snake orbits and is the angle at which the trajectory crosses the $B_Z = 0$ line.

Resultant electron motion

Equations 6.3 and 6.4 can be integrated to describe the position of the electron as a function of time, which is then given by

$$t = \tau_b F(\chi, \theta). \tag{6.5}$$

F is the elliptical integral

$$F(\chi, \theta) = \int_0^{\chi} \frac{d\alpha}{\sqrt{1 - \cos^2(\theta/2)\sin^2(\alpha)}}, \tag{6.6}$$

where $\chi = \arcsin\sqrt{Y^2/[\cos^2(\theta/2)(Y^2 + \sin^2(\alpha))]}$.

Here, it is assumed that at $t = 0$ the electron is at $(X, Y) = (0, 0)$.

The Y co-ordinate can then be expanded as a Fourier series and written as

$$Y(t) = \sum_{k=0}^{\infty} b_{2k+1} \sin((2k+1)\omega t), \tag{6.7}$$

where

$$b_{2k+1} = \frac{4}{(2k+1)\pi} \int_0^{Y_{max}} dY \cos\left[(2k+1)\frac{\pi}{2}\frac{F(\chi, \theta)}{F(\pi/2, \theta)}\right] \tag{6.8}$$

and $Y_{max} = \cos(\theta/2)$.

This completes a full description of the motion of an electron subject to the Lorentz force in a magnetic field gradient.

Two observations can be made about the electron dynamics.

The possible oscillation frequency range is finite. It varies between $\omega = 0$ at $\theta = 0$ and the cut-off frequency $\omega_c = \tau_b^{-1}$ at $\theta = \pi$.

The oscillations are not sinusoidal, and have a harmonic content that depends upon θ. It becomes particularly rich as $\theta \to 0$ and the length of the electron's approach to the $y = 0$ line diverges. Therefore, when $\theta = 0$ the frequency tends to zero, and when $\theta = \pi$ the amplitude tends to zero.

Supply function

The behaviour of an electron population is now considered. In particular, the fraction, $n(\theta)d\theta$, of the total current carrying electrons injected into orbits between θ and $d\theta$ is calculated.

It is assumed that the entire current is carried in snake orbits – states at the edge of the channel are ignored. Electrons can enter a given orbit θ at any distance across the waveguide – it is not assumed that electrons start from $Y = 0$. Y_0 can vary between

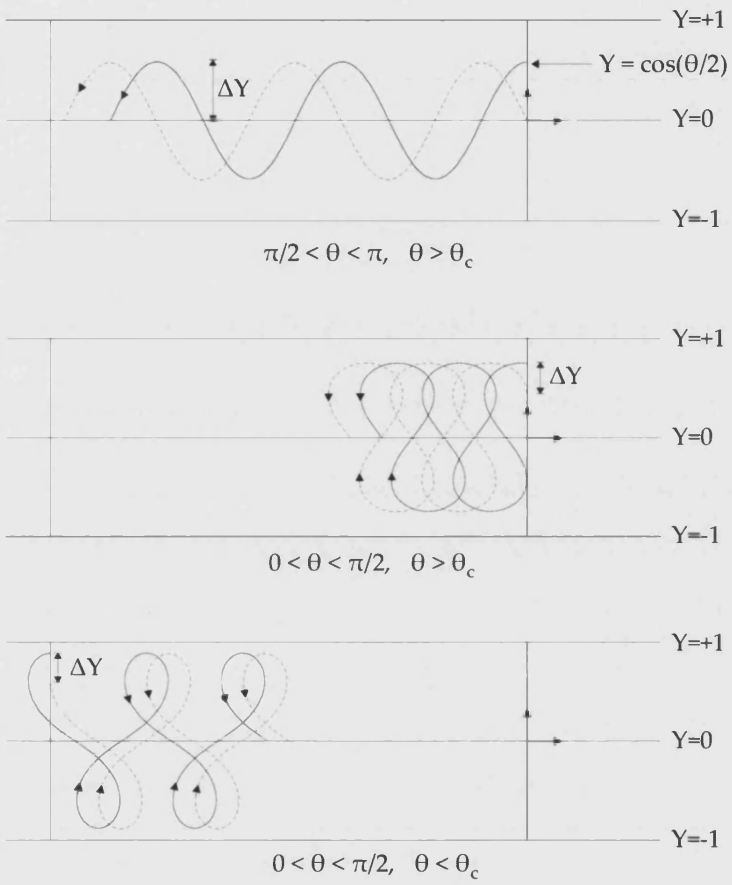

Figure 49. Three different regimes for electron snake orbits in the waveguide, parameterised by θ. Electrons in these orbits are inserted between $Y = 1$ and $Y = -1$ at the beginning of the waveguide.

Y_{min} and Y_{max}, which depend upon the magnitude of θ and the sign of the drift velocity. The possibilities are depicted in fig. 49.

$n(\theta)$ is calculated by summing the velocities of electrons in the region Y_{min} to Y_{max}. This sum is then normalised over the total number of electrons injected into the channel, to obtain

$$n(\theta) = \frac{I\pi}{e} \frac{\int_{Y_{min}}^{Y_{max}} dY_0 \langle v_x(\theta, Y_0, t)\rangle}{\int_0^{\pi} d\theta \int_{Y_{min}}^{Y_{max}} dY_0 \langle v_x(\theta, Y_0, t)\rangle}. \tag{6.9}$$

v_x is calculated for states for which the probability of remaining unscattered after time t is $e^{-t/\tau}$. It is given by

$$\langle v_x\rangle = \int_0^{\infty} dt e^{-t/\tau} v_x(\theta, y_0, t). \tag{6.10}$$

Inserting equations 6.7 and 6.8 into equation 6.3 and assuming $\omega\tau \gg 1$ gives the expression

$$\frac{\langle v_x\rangle}{v_F} = \cos(\theta) - \sum_{k=0}^{\infty} b_{2k+1}^2. \tag{6.11}$$

Plots of three different variables against θ are shown in fig. 50. In panel a, the possible range of Y for different values of θ lie within the clear area. The drift velocity for different orbits is plotted in panel b. The supply function is plotted in panel c.

Finally, the wavelength (that is, the distance between subsequent intersections with the $Y = 0$ line) of an orbit parameterised by θ is determined, from equations 6.5 and 6.11, to be

$$\begin{aligned}\lambda(\theta) &= |X(t = T) - X(t = 0)| \\ &= 2l_b F(\pi/2, \theta)\left|\cos(\theta) - \sum_{k=0}^{\infty} b_{2k+1}^2\right|.\end{aligned} \tag{6.12}$$

Here, T is the time period of the oscillation parameterised by θ.

Radiative emission

The dynamics of the electron's spin is now discussed.

The spin interacts with three magnetic field components. Firstly, B_y splits the spin states into the ground state, $|g\rangle$, and the excited state, $|e\rangle$. Secondly, the transverse oscillations of the spin results in it experiencing an a.c B_z. Finally, the spin interacts with the magnetic component of the e.m. field.

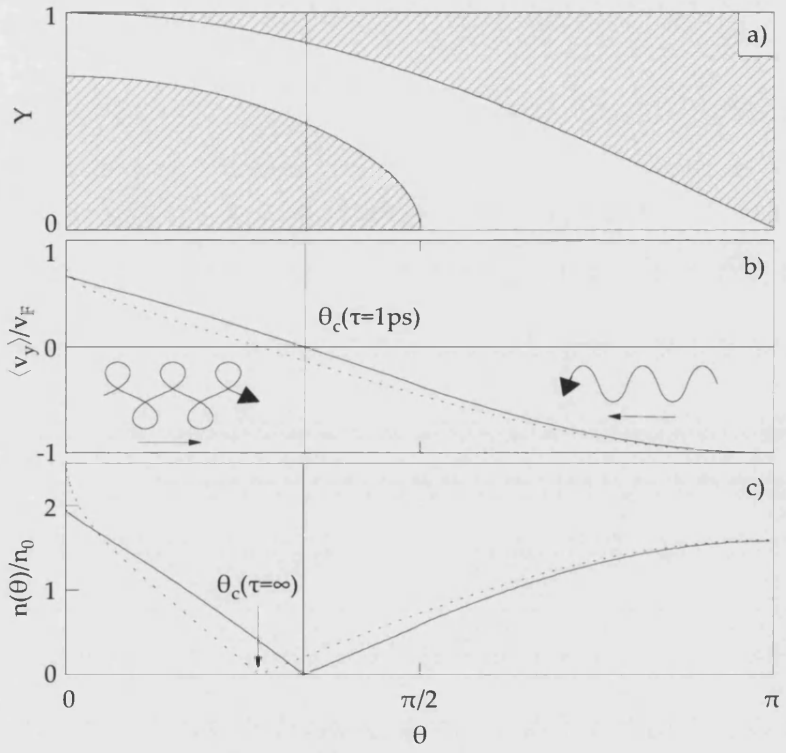

Figure 50. Plots of various oscillator properties against chacterising parameter θ. a) The possible range of Y for different values of θ lie within the clear area. b) Drift velocity for different orbits. c) The supply function. In panels b and c, the values are plotted for $\tau = 1$ps (solid line) and $\tau = \infty$ (dotted line).

If the frequency of B_z matches the Larmor frequency of the electron in B_y, then Rabi oscillations will result as the spin flips between the ground and the excited state. The deviation of B_z from the Larmor frequency is termed the detuning frequency, ω_{eg}. Quantum mechanically, B_z acts to couple $|g\rangle$ and $|e\rangle$. By solving the effective Hamiltonian of the spin coupled to these three fields, the eigenenergies of the two states are found to be

$$E_\pm = \hat{E}_0 \mp \frac{\hbar\Gamma}{4}\sqrt{\chi\rho} - i\frac{\hbar\Gamma}{4}\left(1 \mp \sqrt{\chi/\rho}\right). \tag{6.13}$$

Here,

$$\hat{E}_0 = (\hat{E}_g + \hat{E}_e)/2 \tag{6.14}$$

$$\omega_{eg} = \omega - (\hat{E}_e - \hat{E}_g)/\hbar \tag{6.15}$$

$$\chi = \frac{|\omega_{eg}|}{\Gamma/2} \tag{6.16}$$

$$\rho = \frac{\delta}{-\mathrm{sgn}(\Omega^2) + \sqrt{1+\delta^2}} \tag{6.17}$$

$$\Omega^2 = \Omega_1^2 + \omega^2 - \frac{\Gamma^2}{4} \tag{6.18}$$

$$\delta = \frac{\Gamma|\omega_{eg}|}{|\Omega^2|} \tag{6.19}$$

The eigenenergies are plotted in fig. 51 as a function of the detuning frequency and for different values of r, where $r = \Omega_1/(\Gamma/2)$. Coupling becomes stronger when the frequency of B_z approaches the Larmor frequency. It is also necessary for $r > 1$, as the coupling does not have time to be established if the rate of radiative decay is greater than the Rabi frequency.

The spin can emit a photon by radiatively decaying from the excited state. Clearly, the electron cannot decay from the ground state. The photon emitted escapes to infinity, and so the e.m. field is assumed to be empty. Therefore we can consider these two spin states as $|g,0\rangle$ and $|e,0\rangle$ – they are dressed by the ground state of the field. These two states interact with the electromagnetic state $|g,\mathbf{k},p\rangle$, where $\mathbf{k}$ and p are the photon wavevector and polarisation.

The spontanous radiative emission rate from the excited state is given by

$$\Gamma = \frac{2\pi}{\hbar}\sum_a \sum_{\mathbf{k},p} |\langle a,\mathbf{k}p|V_{phot}|b,0\rangle|^2 \delta(E_b - E_a - \hbar\omega) \tag{6.20}$$

$$= \frac{1}{3}\frac{(g\mu_B)^2 k^3}{ce^2}\alpha. \tag{6.21}$$

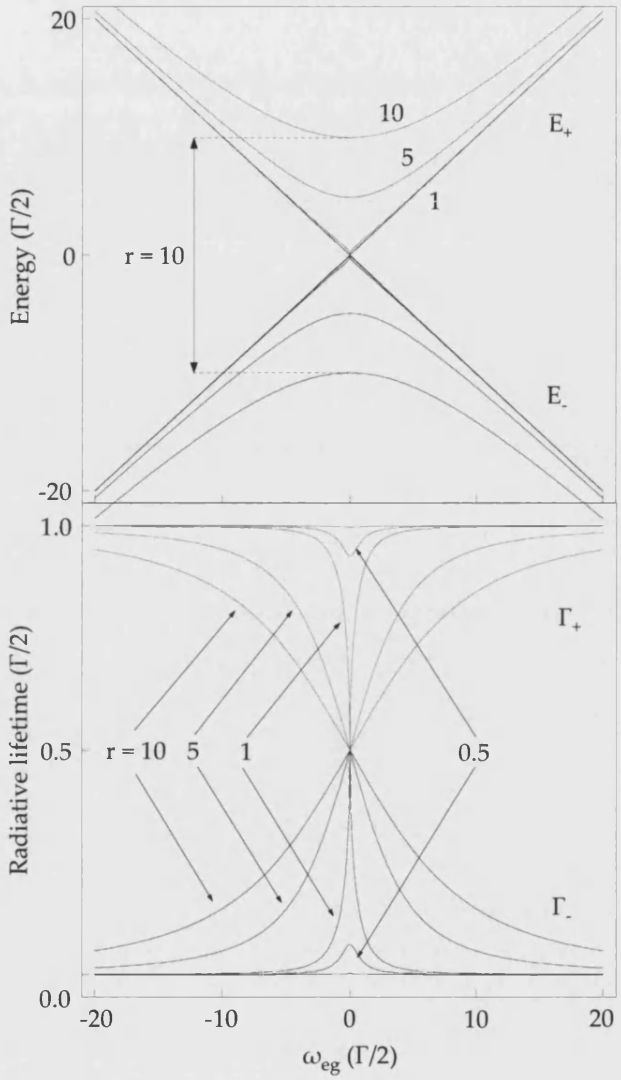

Figure 51. The mixing of the $|g\rangle$ and $|e\rangle$ states through the influence of B_z. ω_{eg} is the detuning frequency. The top panel shows the energies, E_- and E_+, of the two states. The lower panel shows the resultant lifetimes of the mixed states. A range of values of $r = \Omega_1/(\Gamma_{SR}/2)$ are plotted. The origin is set at $E_0 = 0$.

Time evolution in the waveguide is calculated by contour integration of the element of the Green's matrix of the system. The time evolution of the quantum state is calculated by computing the evolution operator $U(t)$. The evolution of the spin from the $|g\rangle$ to $|e\rangle$ is given by

$$U_{eg}(t) = \frac{i\Omega_1}{\Gamma/2} \frac{\sin[\chi(\rho - i\rho^{-1})\frac{\Gamma t}{4}]}{\chi(\rho - i\rho^{-1})} e^{-i\hat{E}^0 t/\hbar} e^{-\Gamma t/4}. \quad (6.22)$$

The amplitude of probability from $|e\rangle$ to $|e\rangle$ is

$$U_{ee}(t) = \left[\cos\left[\chi(\rho - i\rho^{-1})\frac{\Gamma t}{4}\right] - (1 + i\chi)\frac{\sin[\chi(\rho - i\rho^{-1})\frac{\Gamma t}{4}]}{\chi(\rho - i\rho^{-1})}\right] e^{-i\hat{E}^0 t/\hbar} e^{-\Gamma t/4}. \quad (6.23)$$

The probability of emitting a photon is equal to the probability of spontaneous emission multiplied by the probability of being in state $|e\rangle$. This is given by

$$\Gamma|U_{eg}(t)|^2 = \frac{\Gamma}{2} \frac{\Omega_1^2}{\lambda_1^2 + \lambda_2^2} (\cosh(\lambda_2 t) - \cos(\lambda_1 t)) e^{-\Gamma t/2}. \quad (6.24)$$

In summary, in this section electrons injected into both $|e\rangle$ and $|g\rangle$ states have been time-evolved in the waveguide. The probability of single photon emission has been derived.

Many-photon processes

The coupling of the $|g\rangle$ and $|e\rangle$ states by B_z allows spins to be 'recharged' into the excited state after undergoing emission. They can then emit a second photon, and this process can be repeated *ad infinitum*. The probability of an electron injected in the ground state emitting one photon only after a dwell time t in the channel is given by

$$p_g^{(1)}(t) = \int_0^t dt_1 \Gamma |U_{eg}(t_1)|^2. \quad (6.25)$$

By summing the possible one photon emissions over the emission times for the first photon, the probability of a *two* photon event can be determined. The probability of a *three* photon event is calculated in a similar way. This process gives

$$p_g^{(2)}(t) = \int_0^t dt_1 \int_0^{t_1} dt_2 \Gamma^2 |U_{eg}(t_1 - t_2)|^2 |U_{eg}(t_2)|^2 \quad (6.26)$$

and

$$p_g^{(3)}(t) = \int_0^t dt_1 \int_0^{t_1} dt_2 |U_{eg}(t_1 - t_2)|^2 \times \int_0^{t_2} dt_3 \Gamma^3 |U_{eg}(t_2 - t_3|^2 |U_{eg}(t_3)|^2. \quad (6.27)$$

The process is similar for emission from a photon starting from $|e\rangle$, but the emission probability during the *first* time period is governed by U_{ee}. This gives

$$p_e^{(1)}(t) = \int_0^t dt_1 \Gamma |U_{ee}(t_1)|^2, \quad (6.28)$$

$$p_g^{(2)}(t) = \int_0^t dt_1 \int_0^{t_1} dt_2 \Gamma^2 |U_{eg}(t_1 - t_2)|^2 |U_{ee}(t_2)|^2 \quad (6.29)$$

and

$$p_g^{(3)}(t) = \int_0^t dt_1 \int_0^{t_1} dt_2 |U_{eg}(t_1 - t_2)|^2 \times \int_0^{t_2} dt_3 \Gamma^3 |U_{eg}(t_2 - t_3|^2 |U_{ee}(t_3)|^2. \quad (6.30)$$

These integrals can be calculated numerically, and are plotted in fig. 52 for $r = 5$. The top panel shows the results for p_e and the lower panel for p_g.

The necessary quantities have now been derived to calculate the power emission from the device. First, the power radiated by mode k is calculated. This is done by summing over all radiative sequences for that mode, weighted by the supply function into that mode. This gives

$$P_k(\omega_{eg}, t) = n(\theta)(2k+1)\hbar\omega \sum_{i=1}^{\infty} i \left[n_g p_g^i(t) + n_e p_e^i(t) \right]. \quad (6.31)$$

This can be written as

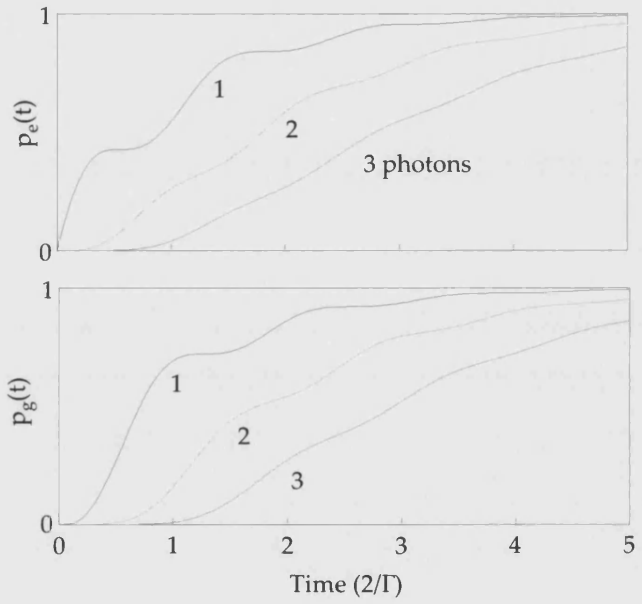

Figure 52. Emission probabilities for one, two and three photons for spins injected in the excited (top) and ground (bottom) states, with $r = 5$.

$$P_k(\omega_{eg}, t) = n(\theta)(2k+1)\hbar\omega \int_0^t d(\Gamma t_1) G(t_1), \tag{6.32}$$

where

$$G(t) = F(t) + \int_0^t dt_1 \Gamma |U_{eg}(t-t_1)|^2 G(t_1). \tag{6.33}$$

Here,

$$F(t) = f(t) + \int_0^t dt_1 \Gamma |U_{eg}(t-t_1)|^2 F(t_1) \tag{6.34}$$

and

$$f(t) = n_g |U_{eg}(t)|^2 + n_e |U_{ee}(t)|^2. \tag{6.35}$$

By summing over all modes, the total radiated power from orbits parameterised by θ is given by

$$P(\omega(\theta), \omega_0, t) = \sum_{k=0}^{\infty} P_k(\omega_{eg}, t). \tag{6.36}$$

Integrating over all values of θ gives the total power radiated by the waveguide –

$$\langle P(\omega_0, t) \rangle = \int_0^{\pi} d\theta P(\omega(\theta), \omega_0, t). \tag{6.37}$$

In summary, the probabilities for multiphoton processes have been calculated, and the resultant power emitted from the waveguide described.

Summary

A number of features of the results presented here can now be usefully highlighted.

Momentum scattering is expected to have no effect on the total fluorescence, as long as electrons are scattered from one spin oscillator state to another. If the spins are scattered into the non-magnetic region, then the lifetime of the oscillators is decreased.

The fluorescence is independent of the spin polarisation of the injected current in long waveguides (in which the electron dwell time is much greater than $(\Omega_1/2)^{-1}$). This is because the Rabi oscillations rapidly remove the memory of the initial state. In shorter waveguides, however, the fluorescence will depend on the polarisation of the supplied spins.

The property of not requiring a spin polarised supply current is highly desirable, because of the difficulties in injecting such a current into semiconductor structures[93, 72].

6.2.2 *Device parameters and calculations*

The above theoretical development can be used to calculate emmision spectra and microwave power for real devices.

In the following numerical calculations, a supply current of $I = 10\mu A$ is assumed. The use of an InAs based quantum well would give values of $m^* = 0.023m_0$ for the effective mass and $g = -15$ for the Landé g factor. An electron density of $n_s = 10^{11}cm^{-2}$ and a field gradient of $B^1 = 2 \times 10^6 T/m$ are realistic.

The total length of the waveguide is taken to be $L = 1000\mu m$. There is no spin polarisation of initial current (i.e. $n_g(t = 0) = n_e(t = 0)$, and the number of spins oscillating in phase with each other is $N = 10^{10}$.

Two regimes can be investigated. The *Rabi* regime is the regime in which spin oscillators experience a strong Rabi coupling, as the oscillatory period of B_z is close to their Larmor frequency due to B_y. As long as their dwell time in the waveguide is long enough, these oscillators fluoresce all along the waveguide.

Oscillators in the *exponential* regime are not regenerated into the excited state by Rabi oscillations. They exhibit radiative decay at the entrance to the waveguide.

The power as a function of dwell time in the waveguide for different values of $\tau = \Omega_1/(\Gamma/2)$ is plotted in fig. 53. For emission when $\tau < 1$, a transient radiative decay occurs for spins prepared in the $|e\rangle$ state. This corresponds to the exponential regime, in which microwave generation occurs in the region near to the start of the waveguide. Conversely, when $\tau > 1$ Rabi oscillations are established. A radiative cascade is established, in which many photons can be emitted from the same electron as it travels along the channel. Radiative emission is therefore distributed along the waveguide.

Fig. 54 shows the fluorescence power as a function of time in the waveguidefor a range of detuning frequencies. Plots for $\tau = 5$ (top, well into the Rabi regime) and $\tau = 0.5$ (bottom, threshold of the exponential regime) are shown.

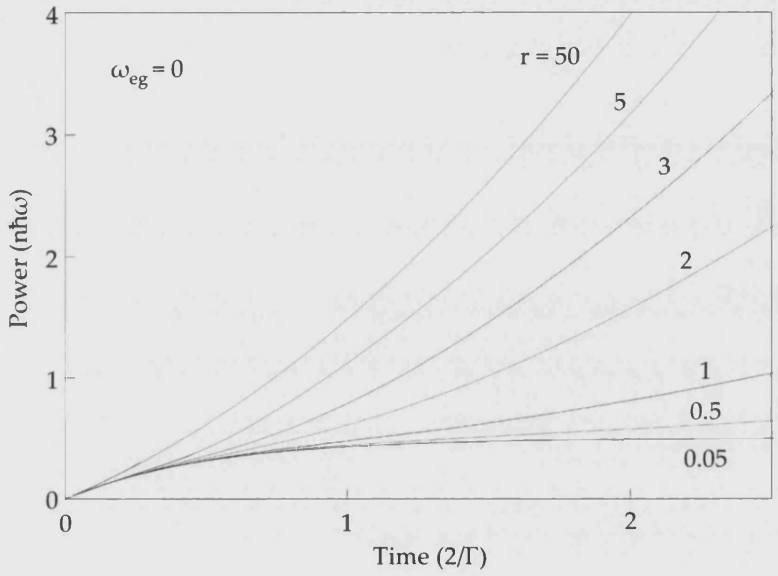

Figure 53. Power radiated from the waveguide as a function of dwell time in the waveguide for different values of $r = \Omega_1/(\Gamma_{SR}/2)$. Here, the detuning of the photon frequency is set to $\omega_{eg} = 0$.

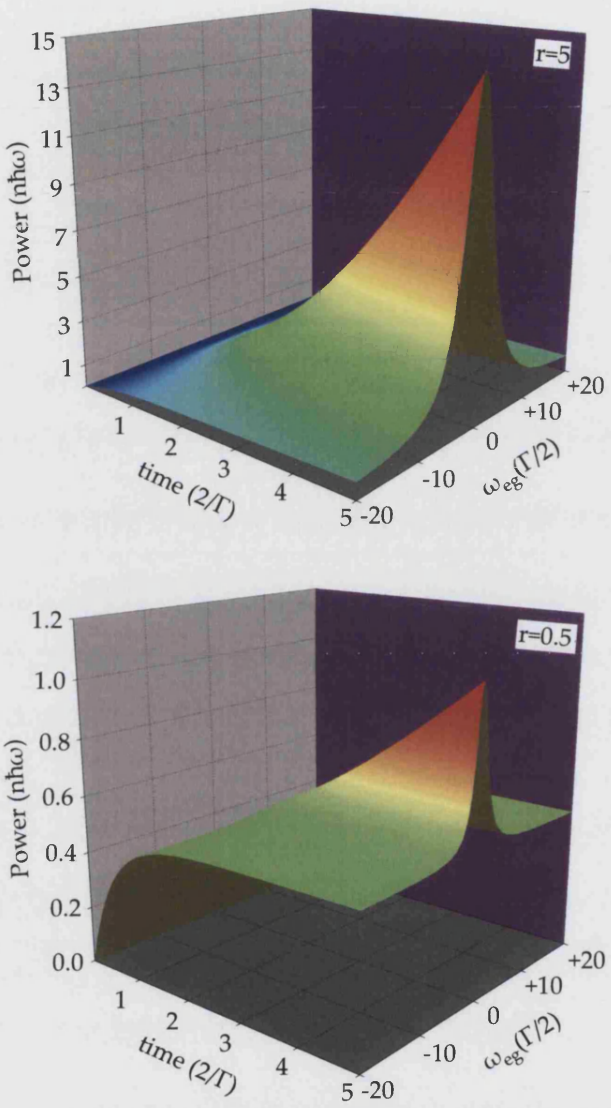

Figure 54. Fluorescence power as a function of time in the waveguide for a range of detuning frequencies ω_{eg}. Top – $r = 5$. Bottom – $r = 0.5$. Note the change in the $n\hbar\omega$ scale between the two plots.

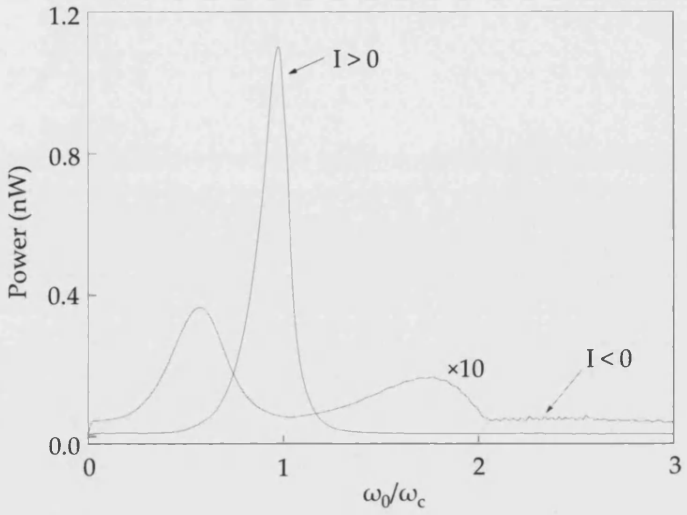

Figure 55. Microwave emission spectrum integrated over all orbits as a function of photon frequency. Orbits with positive and negative drift velocities are plotted separately, and on different scales.

Fig. 55 shows the total power output by all snake orbits as a function of the Larmor frequency. Positive and negative currents are plotted separately, with $I > 0$ corresponding to orbits parameterised by $49.3° < \theta < 180°$ and $I < 0$ corresponding to $0° < \theta < 49.3°$.

The emitted power peaks at 1.2nW, when the Larmor frequency matches the cut-off frequency. For the reverse current, the power peak is at lower frequencies, because, in this direction, slower oscillators are excited, which require smaller Larmor fields at resonance.

The peak position is proportional to $n_s^{1/4}$. Therefore, some tuning of the output frequency would be possible using an electrostatic gate to alter the electron density in the device.

6.2.3 *A free electron laser?*

It is perhaps worth mentioning the similarities between this device and a free electron laser (FEL)[22, 17]. Both rely on an undulating beam of electrons. In both cases, a spatially varying magnetic field is used to direct the electrons. Both emit energy in the form of electromagnetic radiation, and both are tunable

within a fairly wide range.

However, the mechanism of emission is different in the two cases. In the device described above, the electrons couple to the e.m. field *via* spontanteous Raman emission, whilst in a FEL, Brehmstrahlung is the mechanism by which photons are emitted.

6.2.4 *Conclusion*

This theory predicts that cycloid orbits in a magnetic field gradient will emit microwave radiation. This is due to radiative decay from the upper spin state in Zeeman splitting. The emission is sustained by spins being recharged into the excited state by Rabi oscillations. Powers of the order of 1nW are predicted, making this device a possible route for microwave networking in an ULSI setting.

6.3 DEVICE

While the power emitted from a 1mm stripe is predicted to be of the order of 1nW, emission from a stripe of length a few tens of microns would be much smaller, and so difficult to detect. However, a further consequence of the theory outlined above is the interaction of incoming radiation with the snake orbit oscillators. Therefore, a sample consisting of a ferromagnetic stripe overlaying a wider channel was fabricated and irradiated with microwaves. Interactions between the electrons in snake orbits and the e.m. field would perturb the conductance of the channel, and be detectable *via* resistance measurements.

The stripe was 90nm wide and 36μm long. The depth of the 2DEG was 35nm and the channel width was 2μm. The quantum well was formed in an AlGaAs/GaAs heterostructure, rather than an InAs based material. The g factor in GaAs based wells is lower than in InAs structures, and so resonance for a given frequency of e.m. radiation would be expected to occur at higher fields.

The device was made using standard cleanroom techniques, as described in section 3.1. Ohmic contacts were defined using optical lithography and deposited using thermal evaporation. They were then annealed. The channel was defined by optical lithography and wet-etched. Finally, the narrow dysprosium wire was defined with EBL and thermally evaporated. The samples were not gated, as such a structure would have reflected the incident microwaves.

The device is similar to the one described in Chapter 4, but without the additional dry etch, which was used there to narrow the channel to the same width as the ferromagnetic wire. A

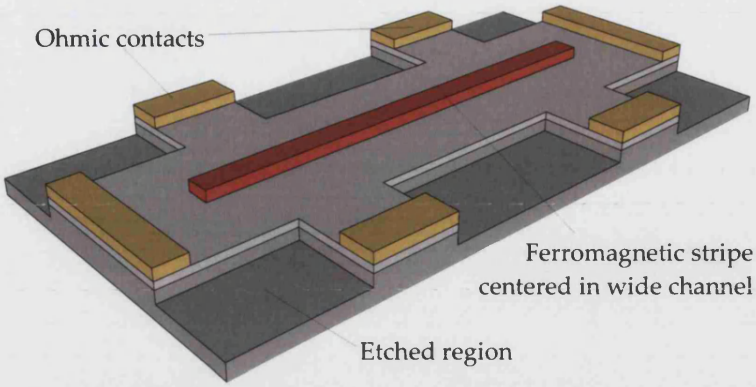

Figure 56. A schematic of the device used to demonstrate ferromagnetic resonance. It is similar to the device described in chapter 4, but with a much broader channel.

schematic of the device is shown in fig. 56.

6.4 EXPERIMENTS

The sample was mounted as in fig. 57 and cooled to 1.5K in a variable temperature insert cryostat. The parallel alignment of the sample to the field was confirmed by Hall measurements. The component of H perpendicular to the 2DEG at $\mu_0 H = 15T$ was around 0.1T, giving an angle of deviation from parallel of less than 1°.

The sample was therefore irradiated from the back, in order to avoid screening of the 2DEG by the magnetic stripe.

A range of microwave frequencies were applied to the sample while the applied field was swept from 0T to 10T. Microwave applied frequencies were in the range 50GHz to 120GHz. The power level was -10dBm, above which significant heating of the sample occured. This was deduced from the attenuation of Shubnikov-de Haas oscillations.

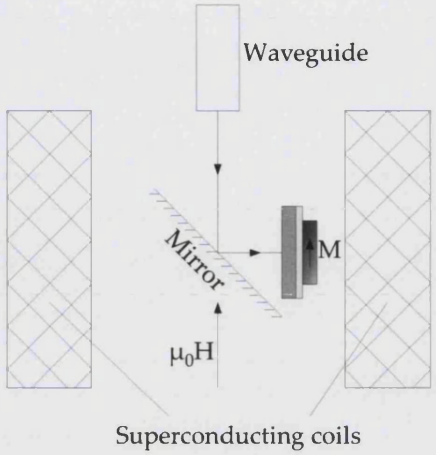

Figure 57. Sample setup for microwave irradiation experiments.

6.5 RESULTS

Results for field sweeps of 0T - 10T are shown in fig. 58. Subsequent frequency traces are offset by 0.4Ω for clarity. Magnetoresistance peaks dependent on the frequency of the applied microwaves are arrowed.

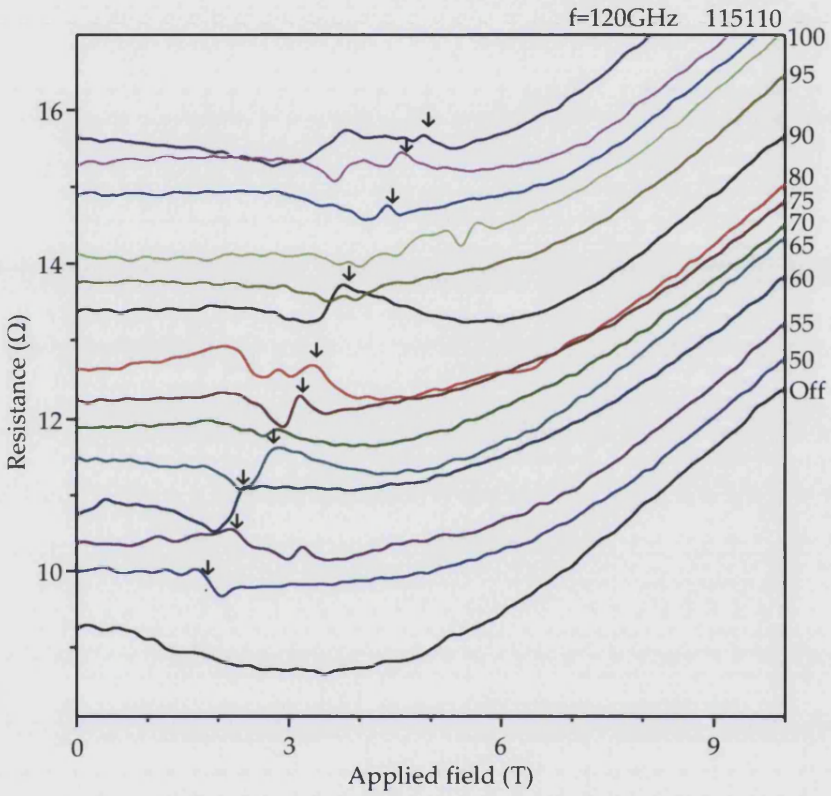

Figure 58. Magnetoresistance of the 2DEG stripe for incident microwave frequencies in the range 50GHz to 120GHz. The field was applied parallel to the 2DEG, and swept from 0T to 10T. Frequency dependent peaks are marked with arrows.

6.6 ANALYSIS

To gain an insight into the source of the f dependent peaks in the magnetoresistence measurements in fig. 58 the applied field at the peak, B_{peak}, can be plotted against the frequency, f, of the microwave radiation. The dependency of B on f is shown in fig. 59.

The line extrapolates to the origin, and the gradient of the B vs S graph is found to be $3.8 \pm 0.3 \times 10^{11}$Ts. From equation 2.8 we determine a value for g of between ± 1.75 and ± 2.05.

Resonance effects due to electrons in the semiconductor quantum well would be expected to show a frequency dependence comensurate with a g factor close to the bulk GaAs value of $g = -0.44$[76]. This suggests that the resistance peaks are not due to interactions between the microwaves and the snake oscillators (or, indeed, any other effect in the 2DEG).

Instead, the g value determined here suggests the peak is due to ferromagnetic resonance in the Dy stripe[68]. The change in the magnetoresistance at this resonant field can be attributed to disturbance of the magnetisation of the stripe by FMR. This, in turn, affects the resistance of the channel *via* the mechanism described in Chapter 4.

It is also worth noting that the ferromagnetic resonance of dysprosium has not previously been directly probed at 0.3K.

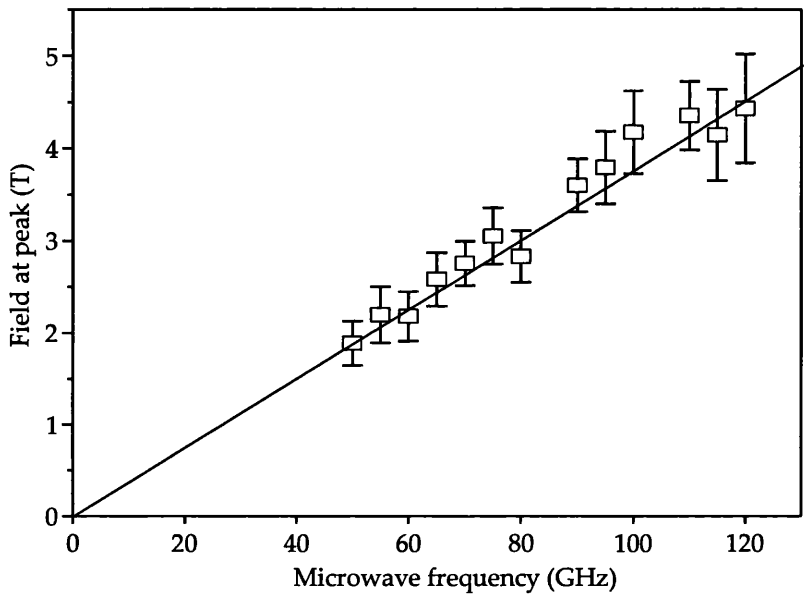

Figure 59. Applied field at peak as a function of microwave frequency. A straight line fitted to the data is observed to pass through the origin. The slope of the line corresponds to a g factor of 1.9 ± 0.15.

6.7 CONCLUSION

In conclusion, a theory has been presented in which radiative emission from electrons in snake orbits has been predicted. For a device of realistic parameters, a power output of the order of 1nW is expected. Such a system would therefore be useful as a short range wireless interconnect.

FMR in a 90nm Dy stripe has been detected by resistance measurements on the underlying 2DEG channel. The measurements gave a Landé g factor of $g = -1.9 \pm 0.15$, in broad agreement with literature values for Dy and in contrast to the value of around -0.44 that would be expected for GaAs.

7 CONCLUSION

Three aspects of snake orbit behaviour have been described in the preceding chapters. In this chapter, the conclusions are drawn together, and some suggestions for further work and extensions are presented.

7.1 RESISTANCE OF MAGNETICALLY MODULATED CHANNELS

7.1.1 *Conclusions*

Asymmetric positive magnetoresistance in a channel modulated by a magnetic field gradient produced by a transversely magnetised ferromagnetic stripe has been observed. This has been described by a model in which the magnetic potential decreases the number of conducting modes in the channel. The asymmetric behaviour comes from the different potentials seen by electrons travelling in opposite directions.

The field was also applied to this device perpendicular to the 2DEG. In this configuration, the stray field from the magnetised stripe was dwarfed by the applied field. Magnetoresistance measurements were performed using pairs of contacts on either side of the stripe, and so counter-propagating edge states were probed.

The difference in the conductance of the two edge states showed oscillations periodic in $1/B$. This were ascribed to scattering between the two edge channels occuring when a bulk Landau state crossed the Fermi surface. Scattering also occurs *via* the edge states mixing in the middle of the channel. Therefore the difference increases with applied field, as the edge states are spatially more separated.

7.1.2 *Further work*

Transverse magnetic field gradient – experimental

To explore further the theory described here, it is necessary to devise some way to access a greater range of values of field gradients. It is useful to consider the maximum field achievable by a device similar to the one used here, but with optimum design parameters.

Dysprosium has the highest saturation magnetisation of all the ferromagnets. The fields required to achieve saturation magnetisation were accessible. A better material for the ferromagnetic stripe is therefore not available.

The width and depth of the stripe can be changed. However, these parameters cannot be chosen arbitrarily. The width of the stripe is limited by the feature size acheivable by electron beam lithography (which is discussed in more depth in section 3.1.1). So the minimum possible wire width is around 20nm.

There is more freedom over the depth of the stripe. In principle, any depth of ferromagnet can be deposited. Larger cross section aspect ratios present more difficulties in fabrication, and so for this discussion a (rather arbitrary) limit for the stripe depth of five times the stripe width is imposed. The magnetic field gradient increases as the depth of the stripe increases, and so it is generally set to the maximum possible.

Finally, the stripe could be brought as close as possible to the 2DEG, by using a very near surface heterostructure. Currently, the shallowest high mobility heterostructures available have a junction depth of around 30nm.

The magnetic field gradient resulting from these parameters can be calculated. It is found to be greatest for a width of about 40nm and a depth of 200nm, which would result in a field gradient of $1.8 \times 10^7 \mathrm{Tm}^{-1}$. However, this width corresponds to only two conducting modes at zero field, and so such a device could not reveal more than two conductive plateaux. There is therefore a tradeoff between field gradient and available modes to exclude.

Transverse magnetic field gradient – theoretical

The consequences of the model presented here depend rather critically on the boundary profile of the lateral confining potential. This is not uncommon – the magnetoresistance of very narrow 2DEG channels formed by etching show qualitatively different behaviour from those defined by an electrostatic pinch gate[84]. In that case, the difference is due to the different scattering mechanisms at the channel boundaries.

The experiment here could be repeated using a pinch gate to define the channel, which would give a more easily calculated channel profile. However, this would increase fabrication difficulties, as the ferromagnetic stripe would have to be isolated from the gates. Alternatively, an increased understanding of the etched channel's profile could be gained by fitting the experimental data to the predicted results for different forms of the potential.

Electron channelling in edge states

It may be worth repeating the experiment in which the magnetic field was applied perpendicular to the sample, but using channels unmodulated by the ferromangetic stripe. The channels in these devices should be have a range of widths, from 1μm to under 200nm, in order to change the coupling between the counter-propagating states.

The devices should have four contacts equally spaced on either side of the channel, as well as two at the ends. This would allow the middle contact pair to be used as voltage probes, and the others to inject and extract current either equally into both edge channels, or preferentially into one side.

The system would also benefit from a more sophisticated theoretical analysis. In particular, the extent of the wavefunctions associated with the edge states and bulk states could be calculated for different fields, and the cross-channel scattering probability deduced.

7.2 SPECTROMETERS

7.2.1 *Conclusions*

Snake state spectrometers, designed to discretise the snake states in a channel and measure the resulting orbits, were designed and tested. Magnetoresistance oscillations were observed, corresponding to the transmission of individual orbits. This provides more evidence for the existence of snake orbits, and supports the idea that a large percentage of the current carrying electrons in the magnetically modulated channel remain in these orbits over distances less than the electron mean free path.

7.2.2 *Further work*

Alternative designs for the snake state spectrometer could be considered. Some prototype devices were fabricated in which the PC 3, the point contact designed to select individual snake orbits, was realised by a pinch gate. By varying the voltage on the gate, the width of PC 3 could have been varied. This would have altered the selectivity of the device, and changed the sharpness of the conductance peaks representing the transmission of a snake orbit.

One of these devices is shown in fig. 60. Attempts at measurements on these devices were frustrated by poor quality ohmic contacts, but the idea is worth pursuing.

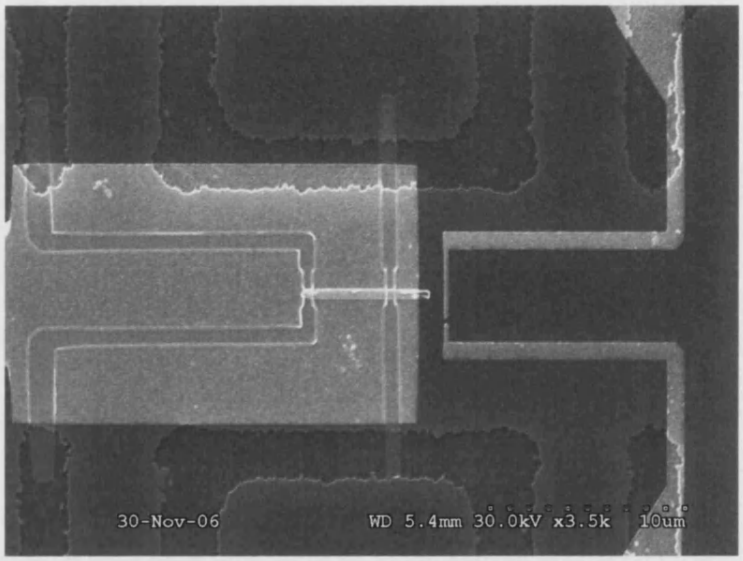

Figure 60. Electron beam micrograph of spectrometers, using a electrostatic pinch gate for PC 3. In this device, the region under the ferromagnetic stripe is covered by an independent electrostatic gate, which would allow greater control over the electron density in the critical region.

7.3 RESISTIVELY DETECTED FERROMAGNETIC RESONANCE

7.3.1 *Conclusions*

A theory has been described in which the electron spin energy levels are split by a transverse magnetic field, and microwave emission results from radiative decay from the excited state to the ground state. Expected emission spectra have been calculated, and peak output power has theoretically been determined to be of the order of 1nW.

In the course of preliminary experiments to test this theory, ferromagnetic resonance in a dysprosium stripe was detected by perturbations to the resistance in a 2DEG channel, and the g factor determined to be 1.95 ± 0.1. This is in broad agreement with literature values[68].

7.3.2 *Further work*

Clearly, much experimental work remains to be done in this area, aimed towards the direct detection of microwave emission from devices. To maximise the power emission, future devices should be made from InAs heterostructures, in contrast to the AlGaAs/-GaAs devices described here. Also, the emitter could consist of a $1mm^2$ array of stripes, each containing an independent population of spin oscillators.

Such a device presents no great difficulties in fabrication, but it may be difficult to measure power levels of a few nanowatts in a cryogenic setting.

7.4 CONCLUSIONS

In conclusion, three different aspects of the Physics of electron transport in steep magnetic field gradients has been investigated. Asymmetric magnetoresistance has been observed and explained, discrete snake states in a channel have been observed and microwave emission has been predicted.

A

CALCULATION OF ENERGY LEVELS IN MAGNETICALLY MODULATED POTENTIAL

The computer program written to calculate eigenfunctions in a symmetric potential is listed below. The program was written in Fortran 90, and was compiled and run on a Sun Ultra E3500 using Solaris v9.

```
program solver
!
! Declare variables
!
double precision:: range,inputrange
double precision:: xmin
double precision:: xmax
double precision:: x,xstep
double precision:: psi !WF at x,x+1/2deltax,x+deltax
double precision:: dpsi !derivative of WF
double precision:: ddpsi !double derivative of WF
double precision:: v,fieldgrad !potential,field gradient
double precision:: inpute,e,laste !Energy in calculation
double precision:: estep !energy change in hunting routine
double precision:: potmin,null
integer :: lastdiverge,diverge,n !Counter for array storage
!
! ---------
! Start program
! ---------
!
! Get start parameters from user,convert to AU.
! Field grad kept as SI
!
write(*,*) 'Please enter field gradient to analyse (MT/m).'
read(*,*) fieldgrad
write(*,*) 'Please enter an initial energy to try (eV).'
read(*,*) inpute
e=inpute*1.602E-19/4.3597E-18
range=500.0*18.897
fieldgrad=fieldgrad*1.0E6
!
```

```
! Initialise variables - fixed parameters
!
xmax=range/2
xmin=-xmax
xstep=range/10000
x=0.0
n=0
null=0.0
potmin=potential(x,fieldgrad,null)
!
! Initialise variables - dynamic parameters
!
write(*,*)'x=',x
write(*,*)'a=',a
write(*,*)'psi=',psi
!
write(*,*)'xmin=',xmin
write(*,*)'xmax=',xmax
write(*,*)'xstep=',xstep
!
! determine potential minimum
!
DO
if(potential(x,fieldgrad,null)<potmin) then
potmin=potential(x,fieldgrad,null)
endif
!
x=x+xstep
if (x>range) EXIT
END DO
write(*,*)'All wf, all index'
!
DO
!
n=n+1
if(n==6)e=inpute*1.602E-19/4.3597E-18
estep=0.0001*0.03675
e=e+estep
lastdiverge=0
!
DO
!
! Start energy loop
!
x=0
```

```
if(n>5)then
psi=0
dpsi=1 !asymmetric wf
else
psi=1
dpsi=0 !symmetric wf
endif
counter=1
open(unit=7,file='wavefunction')
!
DO
!
! Calculate estimates for WF over the working interval
!
ddpsi=2*0.067*(potential(x,fieldgrad,potmin)-e)*psi
dpsi=dpsi+(ddpsi*xstep)
psi=psi+(xstep*dpsi)
x=x+xstep
!
! Store WF,potential(eV)
!
write(7,*)x/18.897,potential(x,fieldgrad,potmin)
  /(1.602E-19/4.3597E-18),psi
write(7,*)(0-x/18.897),potential(x,fieldgrad,potmin)
  /(1.602E-19/4.3597E-18),-psi
!
if(x>xmax .OR. psi>1E10 .OR. psi<(0-1E10)) EXIT
END DO
!
! set divergence
!
if(psi<0) then
diverge=1
else
diverge=-1
end if
!
! compare divergence to previous
!
if((lastdiverge*diverge)<0) then
estep=0-(estep/2.0)
end if
laste=e
e=e+estep
lastdiverge=diverge
```

```
!
! finish condition
!
if(psi<1E10 .AND. psi>(0-1E10))EXIT
if(e>5)EXIT
if(abs(e-laste)<(0.01E-6*0.03675))EXIT
!
! Close file
!
close(unit=7)
END DO
write(*,*)'energy=',e/(1.602E-19/4.3597E-18),'n=',n
if(n>10)EXIT
END DO
!
! -------
! Subroutines
! -------
!
CONTAINS
!
! Calculates potential at a point
!
double precision function potential(pos,bgrad,offset)
double precision, intent(in)::pos,bgrad,offset
double precision:: hbar,me,e,kx,y,magpot
!
e=1.6E-19
me=0.067*9.109E-31
hbar=1.054E-34
kx=1.457E8
y=pos*5.2918E-11
!
! Channel potential
!
if (pos<1625 .AND. pos>-1625) then
potential=0.0
else
potential=0.1837
endif
!
! magnetic potential - calc in joules, conv to au
!
magpot=(1.0/(2.0*me))*(((hbar*kx)-(e*bgrad*0.5*(y**2)))**2)
magpot=magpot/4.3597E-18
```

```
!potential=potential+magpot
!
! relocate to min=0
!
potential=potential-offset
!
end function potential
!
! ----------
! end subroutines
! ----------
!
end program solver
```

B

DERIVATION OF RESISTANCE MINIMA OF SPECTROMETER

It is assumed that electrons are travelling ballistically. The step approximation to the magnetic field profile is used, with $B_z = +B$ on one side of the stripe, and $B_z = -B$ on the other side.

Other symbols used in this derivation are as follows. Physical dimensions are also shown in fig. 61, which is a duplication of fig. 47.

d = distance from PC 2 to PC 3
l_s = distance from PC 1 to PC 2
a = offset of PC 3 from stripe axis
θ = angle between stripe axis and line from PC 2 to PC3
R_c = cyclotron radius of electron in B_z
n = integer number of snake orbit half-wavelengths
l_a = snake orbit wavelength
k_F = Fermi wavevector

We start by relating some of the physical dimensions of the device by

$$\frac{a}{d} = \tan\theta \tag{B.1}$$

and

$$n\frac{l_a}{2} = l_s. \tag{B.2}$$

Also,

$$l_a = 2R_c\cos\left(\frac{\pi}{2} - \theta\right) = 4R_c\sin\theta. \tag{B.3}$$

An integer number of wavelengths must fit into the length of the stripe. We impose this condition by requiring that

$$n \times 2R_c\sin\theta = l_s. \tag{B.4}$$

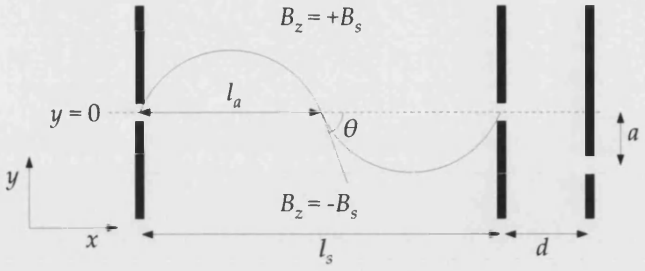

Figure 61. The geometry used to model the devices. Parameters for the derivation are shown.

Combining this with the trigonometric equality

$$\tan^2\varphi = \frac{\sin^2\varphi}{1-\sin^2\varphi} \tag{B.5}$$

gives

$$\frac{a^2}{d^2} = \frac{(l_s/2R_c n)^2}{1-(l_s/2R_c n)^2}. \tag{B.6}$$

This can be rearranged into a more useful form.

$$\frac{a^2}{d^2}\left(1-\left(\frac{l_s}{2R_c n}\right)^2\right) = \left(\frac{l_s}{2R_c n}\right)^2 \tag{B.7}$$

$$\frac{a^2}{d^2}\left((2R_c n)^2 - l_s^2\right) = l_s^2 \tag{B.8}$$

$$(2R_c n)^2 = l_s^2\left(1+\frac{a^2}{d^2}\right) \tag{B.9}$$

$$n^2 = \frac{l_s^2}{(2R_c)^2}\left(1+\frac{a^2}{d^2}\right) \tag{B.10}$$

$$n = \frac{l_s}{2R_c}\sqrt{1+\frac{a^2}{d^2}}. \tag{B.11}$$

The expression for R_c,

$$R_c = \frac{\hbar k_F}{eB_z}, \tag{B.12}$$

can be substituted into equation B.11, and so

$$n = \frac{l_s eB}{2\hbar k_F}\sqrt{1+\frac{a^2}{d^2}} \tag{B.13}$$

is obtained. The requirement that n is integer gives discrete values for B, given by

$$B = \frac{2n\hbar k_F}{l_s e\sqrt{1+\frac{a^2}{d^2}}}. \tag{B.14}$$

C

PUBLICATIONS

The following publications have resulted from the work presented here.

J. Phys: Conf. Ser. 51:419, 2006
Resistively detected microwave absorption by planar spin oscillators.
A. Nogaret, N. J. Lambert, Y. Krupko, J. C. Portal, H. E. Beere and D. A. Ritchie

I.J.M.P B 21(8-9):1507, 2007
Point contact spectroscopy of magnetic edge states.
N. J. Lambert, A. Nogaret, S. Sassine, J. C. Portal, H. E. Beere and D. A. Ritchie

Phys. Rev. B. In publication
Electrically induced spin resonance fluorescence: II Fluorescence spectra.
A. Nogaret, N. J. Lambert and F. M. Peeters

BIBLIOGRAPHY

[1] M Henini A. Nogaret, S. J. Bending. Resistance resonance effects through magnetic edge states. *Phys. Rev. Let.*, 84(10): 2231–2234, 2000. (Cited on page 49.)

[2] S. Adachi. GaAs, AlAs, and $Al_xGa_{1-x}As$ material parameters for use in research and device applications. *J. App. Phys.*, 58 (3):R1, 1985. (Cited on page 5.)

[3] Z. I. Alferov. The history and future of semiconductor heterostructures. *Semiconductors*, 32(1):1, 1998. (Cited on page 4.)

[4] Zh. I. Alferov, V. M. Andreev, V. I. Korol'kov, D. N. Trat'yakov, and Tuchkevich V. M. High-voltage P-N junctions in $Ga_xAl_{1-x}As$ crystals. *Sov. Phys. Semicond.*, 1(10): 1313, 1968. (Cited on page 5.)

[5] C. W. J. Beenakker and H. van Houten. Quantum transport in semiconductor nanostructures. *Solid State Physics*, 44:1, 1991. (Cited on pages 4, 22, 35, and 64.)

[6] S. J. Bending and A. Oral. Hall effect in a highly inhomogeneous magnetic field distribution. *J. App. Phys.*, 81(8):3721, 1997. (Cited on page 54.)

[7] G. Bergmann. Physical interpretation of weak localization: A time-of-flight experiment with conduction electrons. *Phys. Rev. B*, 28:2914, 1983. (Cited on page 22.)

[8] N. Braslau, J. B. Gunn, and J. L. Staples. Metal-semiconductor contacts for GaAs bulk effect devices. *Solid State Electron.*, 10:381–383, 1967. (Cited on page 34.)

[9] L. J. Brillson. *Contacts to Semiconductors: Fundamentals and Technology*. Noyes Publications, Park Ridge, New Jersey, U. S. A, 1993. (Cited on page 34.)

[10] F. J. Bruni and L. T. Nuyen. Production-scale molecular beam epitaxy for high-frequency applications. *JOM*, August: 34, 1998. (Cited on page 6.)

[11] Z. Celinski, K. B. Urquhart, and B. Heinrich. Using ferromagnetic resonance to measure the magnetic moments of ultrathin films. *J. Mag. Mag Mat.*, 166:6, 1997. (Cited on page 15.)

[12] M. F. Chang, V. P. Roychodhury, L. Zhang, H. Shin, and Y. Qian. RF/wireless interconnect for inter- and intra-chip communications. *Proc. IEEE*, 89(4):456, 2001. (Cited on page 97.)

[13] R. Cheung, Y. H. Lee, C. M. Knoedler, K. Y. Lee, T. P Smith, and D. P. Kern. Sidewall damage in n+ -GaAs quantum wires from reactive ion etching. *App. Phys. Lett.*, 54:2130, 1989. (Cited on page 36.)

[14] S. Chikazumi. *Physics of Ferromagnetism*. Oxford University Press, 2nd edition, 1997. (Cited on pages 12 and 13.)

[15] K. K. Choi, D. C. Tsui, and K. Alavi. Dephasing time and one-dimensional localization of two-dimensional electrons in GaAs/$Al_xGa_{1-x}As$ heterostructures. *Phys. Rev. B*, 36: 7751, 1987. (Cited on page 23.)

[16] S. Datta and B. Das. Electronic analog of the electro-optic modulator. *App. Phys. Lett.*, 56(7):665, 1990. (Cited on page 29.)

[17] D. A. G. Deacon, L. R. Elias, J. M. J Madey, G. J. Ramian, H. A. Schwettman, and T. I. Smith. First operation of a free-electron laser. *Phys. Rev. Lett.*, 38(16):892, 1977. (Cited on page 113.)

[18] R. Dingle, H. L. Störmer, A. C. Gossard, and W. Wiegmann. Electron mobilities in modulation-doped semiconductor heterojunction superlattices. *App. Phys. Lett.*, 33(7):665, 1978. (Cited on page 10.)

[19] J. F. Elliott, S. Legvold, and F. H. Spedding. Some magnetic properties of Dy metal. *Phys. Rev.*, 94(5):1143, 1954. (Cited on page 41.)

[20] H. J. Fendler. Chemical self-assembly for electronic applications. *Chem. Mater.*, 13:3196, 2001. (Cited on page 1.)

[21] A. Fert and I. A. Campbell. Two-current conduction in nickel. *Phys. Rev. Lett.*, 21(16):1190, 1968. (Cited on page 29.)

[22] M. Friedman and M. Herndon. Microwave emission produced by the interaction of an intense relativistic electron beam with a spatially modulated magnetic field. *Phys. Rev. Lett.*, 28(4):210, 1972. (Cited on page 113.)

[23] J. K. Furdyna. Diluted magnetic semiconductors. *J. Appl. Phys.*, 64(4):R29, 1988. (Cited on page 30.)

[24] S. Gardelis, C. G. Smith, C. H. W. Barnes, E. H. Linfield, and D. A. Ritchie. Spin-valve effects in a semiconductor field-effect transistor: A spintronic device. *Phys. Rev. B*, 60 (11):7764, 1999. (Cited on page 29.)

[25] N. J. Giordano. *Computational Physics*. Prentice Hall, 1997. (Cited on page 67.)

[26] L. I. Glazman and A. V. Khaetskii. Nonlinear quantum conductance of a lateral microconstraint in a heterostructure. *Europhys. Lett.*, 9:263, 1989. (Cited on page 71.)

[27] G. Grabecki, J. Wrobell, K. Fronc, A. Aleszkiewcz, A. Guziewicz, E. Papis, E. Kaminska, A. Piotrowska, H. Shtrikman, and T. Dietl. Unidirectional transmission of electrons in a magnetic field gradient. *Physica E*, 21 (2-4): 451, 2004. (Cited on pages 50 and 51.)

[28] D Grundler. Ballistic spin-filter transistor. *Phys. Rev. B*, 63: 161307(R), 2001. (Cited on page 29.)

[29] M. Hara, A. Endo, S. Katsumoto, and Y. Iye. Transport in a two-dimensional electron-gas narrow channel with a magnetic-field gradient. *Phys. Rev. B*, 69 (15):153304, 2004. (Cited on pages 28, 49, 50, and 51.)

[30] B. Heinrich, J. F. Cochran, M. Kowalewski, J. Kirschner, Z. Celinski, A. S. Arrott, and K. Myrtle. Magnetic anisotropies and exchange coupling in ultrathin f.c.c. Co(001) structures. *Phys. Rev. B*, 44(17):9348, 1991. (Cited on page 15.)

[31] ITRS. International technology roadmap for semiconductors: 2006 update. Technical report, 2006. (Cited on page 1.)

[32] G. Itskos, R. Murray, A. Meeder, N. Papathanasiou, and M. Ch. Lux-steiner. Optical spin injection in $CuGaSe_2$/GaAs films. *Appl. Phys. Lett.*, 89:032108, 2006. (Cited on page 29.)

[33] J. F. Janak. g factor of the two-dimensional interacting electron gas. *Phys. Rev.*, 174:823, 1969. (Cited on page 71.)

[34] C. L. Joseph, C. Calero, and E. M. Chudnovsky. Collective electromagnetic relaxation in crystals of molecular magnets. *Phys. Rev. B.*, 70:174416, 2004. (Cited on page 97.)

[35] A. Kastalsky and J. C. M. Hwang. Study of persistent photoconductivity effect in n-type selectively doped AlGaAs/-GaAs heterojunction. *Sol. Stat. Comm.*, 51(5):317, 1984. (Cited on page 9.)

[36] J. A. Katine, F. J. Albert, R. A. Buhrman, E. B. Myers, and D. C. Ralph. Current-driven magnetization reversal and spin-wave excitations in Co/Cu/Co pillars. *Phys. Rev. Lett.*, 84(14):3149, 2000. (Cited on page 97.)

[37] J Kilby. US Patent no. 3138743, June 23 1964. (Cited on page 1.)

[38] Charles Kittel. *Introduction to Solid State Physics*. John Wiley & Sons, Inc, 1996. (Cited on pages 7, 13, and 34.)

[39] H. A. Kramers. *Quantum Mechanics*. Dover Publications Inc., 1964. (Cited on page 64.)

[40] H. Kroemer. Theory of a wide-gap emitter for transistors. *Proc. I.R.E.*, 45(11):1535, 1957. (Cited on page 4.)

[41] V. Kubrak, A. W. Rushforth, Rahman F. Neumann, A. C and, B. L. Gallagher, Henini M. Main, P. C and, C. H. Marrows, and B. J. Hickey. The transport of 2D electrons through magnetic barriers. *Physica E*, 7:997, 200.

[42] V. Kubrak, A. Neumann, B. L. Gallagher, P. C. Main, M. Henini, C. H. Marrows, and B. J. Hickey. Magnetoresistance and Hall magnetometry of single submicron ferromagnetic structures. *J. App. Phys.*, 87(9):5986, 2000.

[43] D. Lawton, A. Nogaret, M. V. Makarenko, O.V. Kibis, S.J. Bending, and M. Henini. Electrical rectification by magnetic edge states. *Physica E*, 13:699, 2002. (Cited on pages 28 and 49.)

[44] D. N. Lawton, A. R. Nogaret, S. J. Bending, D. K. Maude, J. C Portal, and M. Henini. Suppression of electron channelling in microscopic magnetic waveguides. *Phys. Rev. B*, 64:033312–1–033312–4, 2001. (Cited on page 28.)

[45] W. Y. Lee, S. Gardelis, B.-C. Choi, Y. B. Xu, C. G. Smith, C. H. W. Barnes, D. A. Ritchie, E. H. Linfield, and J. A. C. Bland. Magnetization reversal and magnetoresistance in a lateral spin-injection device. *J. Appl. Phys.*, 85(9):6682, 1999. (Cited on page 29.)

[46] J. Lindner and K. Baberschke. Ferromagnetic resonance in coupled ultrathin films. *J. Phys.: Condens. Matter*, 15:S465, 2003. (Cited on page 15.)

[47] Mark J. Madou. *Fundamentals of Microfabrication: The Science of Miniaturization*. CRC Press LLC, 2000 N.W. Corporate

Blvd., Boca Raton, Florida 33431, 2002. (Cited on pages 34, 35, and 36.)

[48] J. I. Martin, J. Nogues, K Liu, J. L. Vicent, and I. K. Schuller. Ordered magnetic nanostructures: Fabrication and properties. *J. Mag. Mag. Mat.*, 256:449, 2003. (Cited on page 4.)

[49] J. R. Merril. Introductory quantum mechanics with the computer. *Amer. J. Phys.*, 40:138, 1972. (Cited on page 67.)

[50] A. G. Milnes and D. L. Feucht. *Heterojunctions and Metal-Semiconductor Junctions.* Academic Press, 1972. (Cited on page 5.)

[51] G. E. Moore. Cramming more components onto integrated circuits. *Electronics*, 38(8), 1965. (Cited on page 1.)

[52] W. M. Moreau. *Semiconductor Lithography: Principles, Practises and Materials.* Plenum Press, 1988. (Cited on page 33.)

[53] T. N. Morgan. Theory of the DX center in $Al_xGa_{1-x}As$ and GaAs crystals. *Phys. Rev. B*, 34(4):2664, 1986. (Cited on page 8.)

[54] N. F.. Mott. The resistance and thermoelectric properties of the transition metals. *Proc. Roy. Soc. Lon. A*, 156(888):368, 1936. (Cited on page 29.)

[55] J. E. Müller. Effect of a nonuniform magnetic field on a two-dimensional electron gas in the ballistic regime. *Phys. Rev. Lett.*, 68(3):385, January 1992. (Cited on pages 50 and 64.)

[56] R. J. Nicholas, R. J. Haug, K. von Klitzing, and G. Weimann. Exchange enhancement of the spin splitting in a GaAs-$Ga_xAl_{1-x}As$ heterojunction. *Phys. Rev. B*, 37:1294, 1988. (Cited on page 71.)

[57] A. Nogaret. Electrically induced raman emission from planar spin oscillator. *Phys. Rev. Lett.*, 94:147207, 2005. (Cited on page 98.)

[58] K. S. Novoselov, A.K. Geim, S. V. Dubonos, Hill E. W., and I. V. Grigorieva. Subatomic movements of a domain wall in the peierls potential. *Nature*, 426:812, 2003. (Cited on page 54.)

[59] Y. Ohno, D. K. Young, B. Beschoten, F. Matsukura, H. Ohno, and D. D. Awschalom. Electrical spin injection in a ferromagnetic semiconductor heterostructure. *Nature*, 402:790, 1999. (Cited on page 30.)

[60] N. K. Patel, J. T. Nicholls, L. Martn-Moreno, M. Pepper, J. E. F. Frost, D. A. Ritchie, and G. A. C. Jones. Properties of a ballistic quasi-one-dimensional constriction in a parallel high magnetic field. *Phys. Rev. B*, 44(19):10973, 1991. (Cited on page 71.)

[61] N. K. Patel, J. T. Nicholls, L. Martn-Moreno, M. Pepper, J. E. F. Frost, D. A. Ritchie, and G. A. C. Jones. Evolution of half plateaus as a function of electric field in a ballistic quasi-one-dimensional constriction. *Phys. Rev. B*, 44(24):13549, 1991. (Cited on page 71.)

[62] H. W. C. Postma, T. Teepen, Z Yao, M. Grifoni, and C. Dekker. Carbon nanotube single-electron transistors at room temperature. *Science*, 293:76, 2001. (Cited on page 1.)

[63] M. A. Reed, C. Zhou, C. J. Muller, T. P. Burgin, and J. M. Tour. Conductance of a molecular junction. *Science*, 278:252, 1997. (Cited on page 1.)

[64] J. Reijniers and F. M. Peeters. Snake orbits and related magnetic edge states. *J. Phys. Cond. Matt.*, 12:9771, 200. (Cited on page 50.)

[65] Freescale Semiconductor: Press release. Freescale leads industry in commercializing MRAM technology: 4 Mbit MRAM memory product now in volume production, July 10 2006. (Cited on page 1.)

[66] W. H. Rippard, M. R. Pufall, S. Kaka, S. E. Russek, and T. J. Silva. Direct-current induced dynamics in $Co_{90}Fe_{10}/Ni_{80}Fe_{20}$ point contacts. *Phys. Rev. Lett.*, 92(2): 027201, 2004. (Cited on page 97.)

[67] W. H. Rippard, M. R. Pufall, S. Kaka, T. J. Silva, S. E. Russek, and J. A. Katine. Injection locking and phase control of spin transfer nano-oscillators. *Phys. Rev. Lett.*, 95:067203, 2005. (Cited on page 97.)

[68] F. C. Rossol and R. V. Jones. Ultrabroad ferromagnetic resonancy in dysprosium metal. *J. Appl. Phys.*, 37(3):1227, 1966. (Cited on pages 118 and 125.)

[69] M. L. Roukes, A. Scherer, H. G. Allen Jr, S. J. Craighead, R. M. Ruthen, E. D. Beebe, and J. P. Harbison. Quenching of the Hall effect in a one-dimensional wire. *Phys. Rev. Lett.*, 59 (26):3011, 1987. (Cited on page 49.)

[70] H. S. Rupprecht, J. M. Woodall, and G. D. Pettit. Efficient visible electroluminescence at 300K from $Ga_{1-x}al_xAs$ P-N junctions grown by liquid-phase epitaxy. *Appl. Phys. Lett.*, 11 (3):81, 1967. (Cited on page 5.)

[71] N. Samarth. An introduction to semiconductor spintronics. *Sol. Stat. Phys.*, 58:1, 2004. (Cited on page 29.)

[72] G. Schmidt, D. Ferrand, L. W. Molenkamp, Filip. A. T., and B. J. van Wees. Fundamental obstacle for electrical spin injection from a ferromagnetic metal into a diffusive semiconductor. *Phys. Rev. B*, 62(8):R4790, 2000. (Cited on pages 29 and 110.)

[73] D. Y. Sharvin and Y. V. Sharvin. Magnetic-flux quantisation in a cylindrical film of a normal metal. *JETP Lett.*, 34(5):272, 1981. (Cited on page 27.)

[74] W. Shockley. US Patent no. 2569347, 1951. (Cited on page 4.)

[75] C. G. Smith. Low-dimensional quantum devices. *Rep. Prog. Phys.*, 59(2):235, 1996. (Cited on pages 7 and 10.)

[76] M. J. Snelling, G. P. Flinn, A. S. Plaut, R. T. Harley, A. C. Tropper, R. Eccleston, and C. C. Phillips. Magnetic g factor of electrons in $GaAs/Al_xGa_{1-x}As$ quantum wells. *Phys. Rev. B.*, 44(20):11345, 1991. (Cited on pages 68 and 118.)

[77] J. Spector, H. L. Stormer, K. W. Baldwin, L. N. Pfeiffer, and K. W. West. Electron focusing in two-dimensional systems by means of an electrostatic lens. *J. Appl. Phys.*, 56(13):1290, 1990. (Cited on page 81.)

[78] J. Spector, H. L. Stormer, L. N. Baldwin, K. W. Pfeiffer, and K. W. West. Refractive switch for two-dimensional electrons. *Appl. Phys. Lett.*, 56(24):2433, 1990. (Cited on page 81.)

[79] S. J. Steinmuller, T. Trypiniotis, W. S. Cho, A. Hirohata, W. S. Lew, C. A. F. Vaz, and J. A. C. Bland. Highly efficient spin filtering of ballistic electrons. *Phys. Rev. B*, 69(15):153309, 2004. (Cited on page 29.)

[80] H. L. Stormer, R. Dingle, A. C. Gossard, W. Wiegmann, and M. D. Sturge. Two-dimensional electron-gas at differentially doped GaAs-AlGaAs heterojunction interface. *J. Vac. Sci. Tech.*, 16(5):1517, 1979. (Cited on page 9.)

[81] R. P. Taylor, P. T. Coleridge, M. Davies, Y. Feng, J. P. McCaffrey, and P. A. Marshall. Physical and electrical investigation

of ohmic contacts to AlGaAs/GaAs heterostructures. *J. Appl. Phys.*, 76(12):7966, 1994. (Cited on page 34.)

[82] J. Tejada, E. M. Chudnovsky, J. M. Hernandez, and R. Amigó. Electromagnetic radiation produced by avalanches in the magnetisation reversal of Mn_{12}-acetate. *App. Phys. Lett.*, 84 (13):2373, 2004. (Cited on page 98.)

[83] J. M. Thijssen. *Computational Physics*. Cambridge University Press, 1999. (Cited on page 67.)

[84] T. J. Thonton, M. L. Roukes, A. Scherer, and B. P. Van de Gaag. Boundary scattering in quantum wires. *Phys. Rev. Lett*, 63(19):2128, 1989. (Cited on pages 92 and 122.)

[85] M. et al Tittnich. A year in the life of an immersion lithography alpha tool at Albany NanoTech. *Proc. SPIE*, 6151:1, 2006. (Cited on page 33.)

[86] C. P. Umbach, C. Van Haesendonck, R. B. Laibowitz, S. Washburn, and R. A. Webb. Direct observation of ensemble averaging of the Aharonov-Bohm effect in normal-metal loops. *Phys. Rev. Lett.*, 56(4):386, 1986. (Cited on page 27.)

[87] D. Uzur, A. Nogaret, H. E. Beere, D. A. Ritchie, C. H. Marrows, and B. J. Hickey. Probing the annular electronic shell structure of a magnetic corral. *Phys. Rev. B*, 69(24):241301, 2004. (Cited on page 29.)

[88] P. Van Dorpe, Z. Liu, W. Van Roy, V. F. Motsnyic, Sawicki M., G. Borghs, and J. De Boeck. Very high spin polarization in GaAs by injection from a (Ga,Mn)As Zener diode. *Appl. Phys. Lett.*, 84(18):3495, 2004. (Cited on page 30.)

[89] H. Van Houten, B. J. Van Wees, M. J. G. Heijman, and J. P. André. Submicron conducting channels defined by shallow mesa etch in GaAs-AlGaAs heterojunctions. *App. Phys. Lett.*, 49:1781, 1986. (Cited on page 35.)

[90] B. J. van Wees, H. van Houten, C. W. J. Beenakker, J. G. Williamson, L. P. Kouwenhoven, D. van der Marel, and C. T. Foxon. Quantized conductance of point contacts in a two-dimensional gas. *Phys. Rev. Lett.*, 60(9):848, 1988. (Cited on page 71.)

[91] B. J. van Wees, E. M. M. Willems, L. P. Kouwenhoven, C. J. P. M. Harmans, J. G. Williamson, C. T. Foxon, and J. J. Harris. Suppression of shubnikov–de haas resistance oscillations

due to selective population or detection of landau levels: Absence of inter-landau-level scattering on macroscopic length scales. *Phys. Rev. B*, 39:8066, 1989. (Cited on pages 74, 75, and 76.)

[92] C. Vieu, F. Carcenac, A. Pepin, Y. Chen, M. Mejias, A. Lebib, L. Manin-Ferlazzo, L. Couraud, and H. Launois. Electron beam lithography: Resolution limits and applications. *Appl. Surf. Sci.*, 164:111, 2000. (Cited on page 33.)

[93] I. Žutić, J. Fabian, and S. Das Sarma. Spintronics: Fundamentals and applications. *Rev. Mod. Phys.*, 76(2):323, April 2004. (Cited on pages 29 and 110.)

[94] R. Wang, X. Jiang, R. M. Shelby, Macfarlane R. M., S. S. P. Parkin, S. R. Bank, and J. S. Harris. Increase in spin injection efficiency of a CoFe/MgO(100) tunnel spin injector with thermal annealing. *Appl. Phys. Lett.*, 86(5):052901, 2005. (Cited on page 30.)

[95] R. A. Webb, S. Washburn, C. P. Umbach, and R. B. Laibowitz. Observation of $\frac{h}{e}$ Aharonov-Bohm oscillations in normal-metal rings. *Phys. Rev. Lett.*, 54(25):2696, 1985. (Cited on page 27.)